Centro de Investigación Científica y de Educación Superior de Ensenada, Baja California

Doctorado en Ciencias
en Ciencias de la Tierra
con orientación en Sismología

Role of the fluid viscous stress tensor in poroelastic wave propagation across discontinuities

Tesis

para cubrir parcialmente los requisitos necesarios para obtener el grado de

Doctor en Ciencias

Presenta:

Josué Gabriel González Flores

Ensenada, Baja California, México

2022

Tesis defendida por

Josué Gabriel González Flores

y aprobada por el siguiente Comité

_____

Dr. Pratap Narayan Sahay Sahay

Director de tesis

Dr. Jonas de Dios de Basabe Delgado
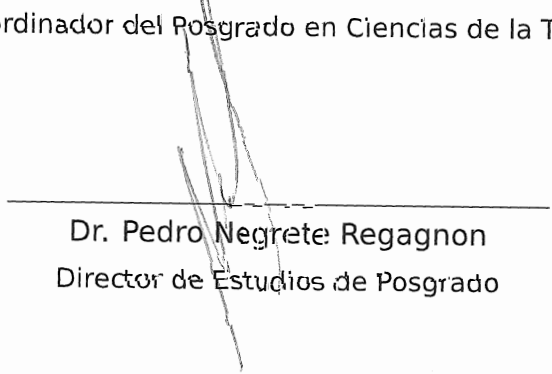
Dr. Luis Alonso Gallardo Delgado

Dr. Tobias Markus Müller

_____

Dr. Javier Alejandro González Ortega

Coordinador del Posgrado en Ciencias de la Tierra

_____

Dr. Pedro Negrete Regagnon

Director de Estudios de Posgrado

Resumen de la tesis que presenta Josué Gabriel González Flores como requisito parcial para la obtención del grado de Doctor en Ciencias en Ciencias de la Tierra con orientación en Sismología.

Rol del tensor de esfuerzos viscosos del fluido en la propagación de ondas poroelásticas a través de discontinuidades

Resumen aprobado por:

Dr. Pratap Narayan Sahay Sahay
Director de tesis

El tensor de esfuerzo viscoso del fluido captura los esfuerzos debidos al cambio en el tiempo de la deformación de un fluido Newtoniano. La traza de este tensor describe la disipación de presión, y la parte libre de traza describe el movimiento de cizalla del fluido, es decir, la vorticidad del fluido. Ambos procesos representan los dos mecanismos de atenuación intrínseca del fluido. Este tensor no existe en la ampliamente utilizada teoría de poroelasticidad de Biot. Como resultado, la disipación viscosa en el fluido no se incluye adecuadamente. Esta solo tiene en cuenta la disipación debida al arrastre del movimiento relativo de las partes que constituyen el medio poroso. La falta del tensor de esfuerzo viscoso del fluido tiene implicaciones para la propagación de ondas a través de discontinuidades poroelásticas. Esta tesis estudia esas implicaciones analizando el *scattering* de ondas en contactos planos con superficies impermeables y permeables. Esto se realiza en la teoría de poroelasticidad de De la Cruz-Spanos que incluye el tensor de esfuerzo viscoso del fluido en las relaciones constitutivas. Esta teoría describe un proceso adicional, la onda S lenta, que manifiesta la vorticidad del fluido a macro-escala, junto con las ondas P rápida, P lenta y S rápida predichas en la teoría de Biot. El caso de las superficies impermeables es de especial interés porque aumenta la generación de vorticidad del fluido; por lo tanto, las implicaciones del tensor de esfuerzo viscoso son más evidentes. Este caso muestra que sin el tensor de esfuerzo viscoso en las ecuaciones constitutivas, el movimiento del fluido no está restringido en la dirección tangencial al contacto. Esto provoca una violación de la condición fundamental de no deslizamiento del fluido. La ausencia del tensor de esfuerzo viscoso no sólo afecta a la definición de las condiciones de frontera, también provoca un cambio en la amplitud de las ondas convertidas. En el caso de las ondas S, genera una reducción de la amplitud que, en superficies impermeables, existe aunque no haya ningún contraste de propiedades. Esta también se produce en las ondas P; sin embargo, la reducción de amplitud es menor. Este efecto no se limita a las superficies impermeables, también aparece en los contactos permeables con variaciones en las propiedades. En todos los casos, los efectos no son exclusivamente función de la frecuencia. Por el contrario, dependen del contraste de propiedades en la heterogeneidad y el contacto hidráulico. Debido a esto, el efecto del esfuerzo viscoso no puede determinarse con un único término en las ecuaciones de movimiento, como postula la teoría de permeabilidad dinámica. Por lo tanto, las ecuaciones poroelásticas deben incluir el tensor de esfuerzo viscoso del fluido, como se hace en la teoría de De la Cruz-Spanos, para describir adecuadamente la propagación de las ondas a través de discontinuidades.

Palabras clave: Poroelasticidad, propagación de ondas, tensor de esfuerzos viscosos

Abstract of the thesis presented by Josué Gabriel González Flores as a partial requirement to obtain the Doctor of Science degree in Earth Science with orientation in Seismology.

Role of the fluid viscous stress tensor in poroelastic wave propagation across discontinuities

Abstract approved by:

Dr. Pratap Narayan Sahay Sahay

Thesis Director

The fluid viscous stress tensor captures the stresses due to the strain rate of a Newtonian fluid. The trace of this tensor describes the pressure dissipation, and the trace-free part describes the fluid shear motion, i.e., the fluid vorticity. Both terms represent the two intrinsic loss mechanisms of the fluid. This tensor is missing in the widely used Biot theory of poroelasticity. As a result, the viscous dissipation within the fluid is not adequately captured in this theory. It only accounts for the viscous dissipation due to the drag of the relative motion of the constituent parts of a porous medium. The missing fluid viscous stress tensor has implications for waves across poroelastic discontinuities. This thesis studies those implications by analyzing the wave-scattering on planar contacts with impermeable and permeable surfaces. It is carried out in the framework of the de la Cruz-Spanos poroelasticity theory that includes the fluid viscous stress tensor into the constitutive relations. This theory incorporates an additional wave process, the slow S-wave, which manifests fluid vorticity at a macro-scale, along with the fast P-, slow P-, and fast S-waves predicted in the Biot theory. The case of impermeable surfaces is of particular interest because it enhances the generation of fluid vorticity; hence the implications of the fluid viscous stress tensor are more apparent. This case shows that, without the fluid viscous stress tensor in the poroelastic constitutive equations, the motion of the fluid is unconstrained in the tangential direction of the contact. It causes a violation of the fundamental no-slip boundary condition of the fluid. The absence of fluid viscous stress tensor not only affects the definition of boundary conditions but also causes a change in the amplitude of the scattered waves. In the case of S-waves, it generates a reduction of amplitude that, in impermeable surfaces, exists even if there is not any contrast in properties. It also occurs in P-waves. However, there is a minor amplitude reduction in this case. This effect is not limited to the impermeable surfaces, but it also appears in the permeable contacts with variations in properties. In all the cases, those effects are not exclusively a function of the frequency. Instead, they are dependent on the contrast of properties at the heterogeneity and the hydraulic contact. Therefore, the effect of the viscous stress can not be determined with a single term in the equations of motion, as the dynamic permeability theory postulates. Thus, the poroelastic equations must include the fluid viscous stress tensor, as in the de la Cruz-Spanos theory, to describe the wave propagation across discontinuities.

Dedication

I dedicate this thesis to my parents, who inspired me to keep learning, my wife, who always supports me in continuing this journey, and my siblings, who are always there to help me.

Acknowledgments

Contents

Chapter 1   Introduction

Chapter 2   Basics of poroelastic theory

Chapter 3   Boundary conditions at discontinuities

Contents (continue)

Contents (continue)

Figures list

Figures list (continue)

Figures list (continue)

Figures list (continue)

Figures list (continue)

Figures list (continue)

Tables list

Chapter 1.   Introduction

1.1   Background and perspective

1.1.1   Physics of viscous boundary layers in porous media

Reservoir seismology aims to obtain higher resolution subsurface images in the context of geo-fluid characterization. Herein, the reservoirs are composed of a solid frame with connected pores, and they are saturated with viscous fluids. The effects of the saturating fluid on elastic moduli are well known. However, the wave attenuation resulting from the solid frame and the fluid interactions is an open research problem. The cause of this attenuation is the generation of the intrinsic diffusive processes of a Newtonian fluid. These processes are pressure diffusion and fluid vorticity, and they are characterized by the fluid viscous stress tensor (Landau and Lifshitz, 1987). Although, in a Newtonian Fluid both process are presented, the vorticity is the predominant cause of attenuation, since any relative motion of the fluid with respect to the solid frame generates it.

Because the fluid vorticity's skin depth (δ) is frequency-dependent, the generation of relative fluid motion in a pore has two regimes. At low frequencies, δ is larger than any characteristic pore-throat diameter (Λ); thus, the fluid remains almost fully coupled to the pore walls due to the viscous forces, as shown in Figure 1 for the case of a single pore under a periodic motion. As the frequency increases, δ approaches Λ, causing a significant reduction in coupling. Finally, at high enough frequencies, the viscous skin depth becomes smaller than the pore radius; thus, the fluid and the solid frame are only coupled in the vicinity of the pore walls. This allows the generation of fluid vorticity and the viscous boundary layers (VBLs) near to the walls (Figure 2).

While the fluid to solid frame interaction can be analyzed at pore-scale for a single pore, studying the effect on the attenuation of mechanical waves is not feasible. This is because the wavelength is much larger than the characteristic pore size. Hence, there is a vast number of pores at wavelength, and their distribution is usually undefined. The study of these effects can be naturally performed in the poroelastic theory that up-scales the behavior of a porous medium by considering the average motion of the solid frame and fluid in a representative volume element (RVE).

Low-frequency regime
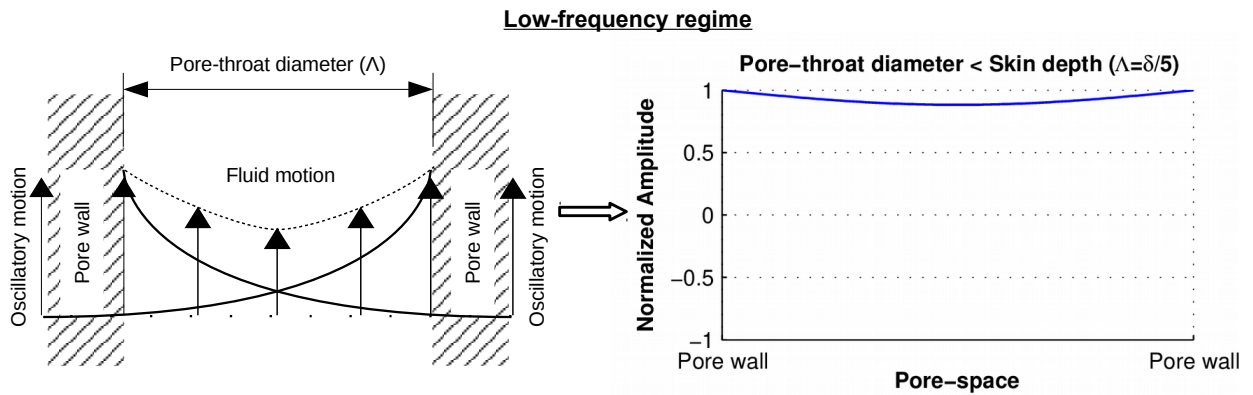
Figure 1. Fluid vorticity in a single pore generated by an in-phase periodic oscillation, in the vertical direction of the pore walls. The left panel is a schematic representation of the fluid motion, and the right one presents the normalized displacement of a Newtonian fluid. Here, the viscous skin depth is five times the pore-throat radius. Therefore, the fluid is viscously coupled to the wall.

High-frequency regime
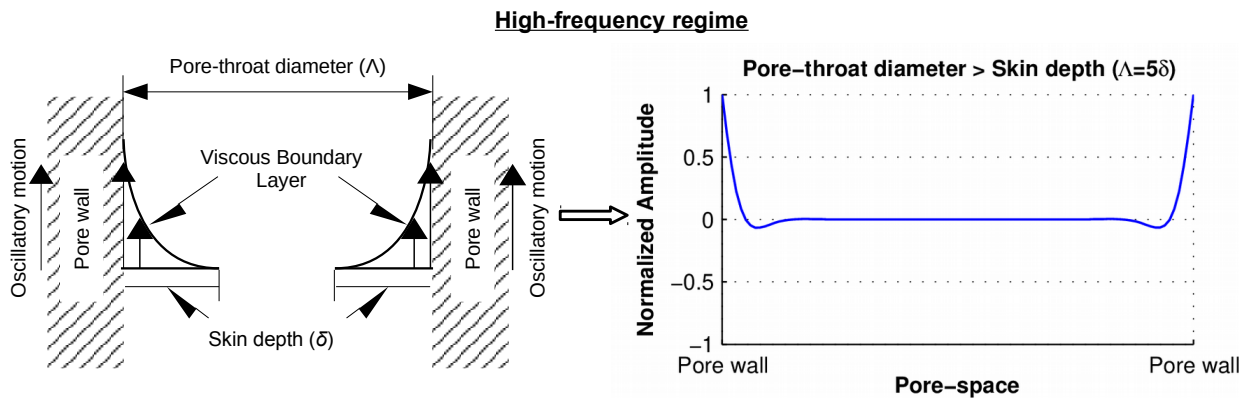
Figure 2. Fluid vorticity in a single pore generated by an in-phase periodic oscillation, in the vertical direction of the pore walls. The left panel is a schematic representation of the fluid motion, and the right one presents the normalized displacement of a Newtonian fluid. Here, the pore-throat radius is five times the viscous skin depth. Therefore the fluid vorticity is generated near the walls.

1.1.2 Viscous boundary layers in Biot poroelastic theory

The standard theory for analyzing wave propagation in fluid-saturated porous media is due to Biot (1956a, 1956b). He constructs the poroelastic constitutive equations by a variational approach considering an elastic energy potential but ignoring the fluid viscous stress. This theory successfully predicts a second compressional (slow P-) wave, which represents the out-of-phase compressional motion of the constituent parts of the porous medium, apart from the seismic wave fields, namely, the fast P- and S-waves. The slow P-wave has a diffusive character in the low-frequency regime

when the fluid is viscously coupled to the solid frame, and it behaves as the P-wave in the fluid in the high-frequency regime. The generation of slow P-wave amounts to the reduction in the amplitude of the seismic waves. However, not until the early eighties, when Plona (1981) observed the slow P-wave experimentally for the first time, did the rock physics and seismic exploration community starts paying attention to the poroelastic theory.

In the poroelastic perspective, the wave attenuation mechanisms are the fluid movement relative to the solid frame on account of Darcy flow, so-called wave-induced fluid flow (WIFF), and the viscous relaxations within the fluid. WIFF can occur in pore-scale heterogeneities, i.e., the squirt flow, or in heterogeneities much larger than the pore size but much smaller than the wavelength, i.e., the mesoscopic flow. Also, it can occur in macroscopically homogeneous media due to pressure gradients between peaks and troughs of the wave, the so-called Biot global flow. In all these cases, the fluid is moving to balance the pressure gradients that the wave generates. This mechanism is widely studied. Müller et al. (2010) present a review of those studies. In contrast, there are few studies on the second mechanism, considering it an independent process. This is because the fluid viscous stress tensor, which is needed to characterize the intrinsic relaxation of Newtonian fluids (Landau and Lifshitz, 1987), is missing in the widely used poroelastic theory of Biot.

It is believed that Biot global flow quantifies the effects of fluid viscous stress. In fact, it only accounts for the attenuation due to the viscous-inertial coupling of the fluid, as it does not consider the generation of fluid vorticity. This belief seems plausible in the low-frequency regime when the fluid is viscously coupled to the pore walls (Figure 1) because fluid vorticity is not generated in this regime. However, in the high-frequency regime, fluid vorticity develops (Figure 2). Therefore, at least in this regime, the viscous stress tensor must be included to account for the generation of fluid vorticity.

Biot (1956b) points out that, at the high-frequency regime, an additional term is needed to capture the effects of the viscous forces in the VBLs. He proposed incorporating this effect by including a viscodynamic correction factor in the fluid mobility term. This factor aims to capture the effects of the fluid viscous stress tensor without including it. However, there is no expression that defines the correction in his work,

and its definition requires knowing the geometry of the pore-space, which is infeasible for porous rocks. Johnson (1982) points out that for soft porous materials, such as gels, the viscous forces of the fluid must affect the deformation of the solid frame. He attempts to incorporate the fluid viscous stress tensor into the Biot theory by postulating the existence of effective bulk and shear viscosities. Such effective viscosities account for the effect of the fluid viscous stress tensor at the macro-scale. However, their incorporation into the Biot theory is not properly defined. The effective viscosities are not related to the fluid properties, and they do not account for the interactions at the pore surface. Later, Johnson et al. (1987) incorporated the viscodynamic correction factor of Biot (1956b) in the poroelastic equations of motion by considering a frequency-dependent (dynamic) permeability, the so-called JKD model. The JKD model considers the effect of VBLs but not explicitly the existence of the fluid vorticity. Thus, it cannot account for the development of VBLs at heterogeneities because additional couplings of the fluid and the heterogeneity have to be considered in this case. For that, the model must include a description of the fluid vorticity that the coupling with the heterogeneity will generate. However, the fluid viscous stress tensor that describes the fluid vorticity is neglected in the JKD model.

1.1.3   Viscous stress tensor and slow S-wave in poroelastic theory

There has been attempts to incorporate the fluid viscous stress tensor in the poroelastic description. Katsube (1985) and Katsube and Carroll (1987a, 1987b) develop a poroelastic approach that includes the fluid viscous stress tensor into the formulation using the mathematics of the mixture theory. However, this theory does not define the parameters in terms of the physical properties of porous media. In addition, the construction of the macroscopic description does not include all the interactions happening at the pore surfaces. It only accounts for the interactions in terms of displacements but ignores the strains and stresses that such interactions generate.

Another theory of poroelasticity that includes the fluid viscous stress tensor is given by de la Cruz and Spanos (1985). Here onwards, I refer to it as the dCS theory. To construct the macroscopic poroelastic equations, they up-scale the linear elastic theory and Navier-Stokes equations applying the mathematics of volume-averaging (Slattery, 1969; Whitaker, 1969).This methodology includes the average motions, strains, and

stresses of the solid frame, the fluid, and the pore surfaces. The inclusion of the fluid viscous stress tensor in the dCS theory predicts an additional shear wave, the slow S-wave, and the waves predicted in the Biot theory. This slow S-wave is the manifestation of fluid vorticity at the macro-scale. It allows a complete description of a porous medium at the macro-scale; however, de la Cruz and Spanos (1985) do not define its parameters in terms of the properties of porous media. It was not until two decades later that those parameters were interpreted and related to the properties of porous media by Sahay (2008). In his work, Sahay also shows that the Biot theory can be derived from dCS theory if the viscous stress tensor is vanished in the constitutive equations.

Sahay (2008) analyzes the implications of including the viscous stress tensor in the dCS poroelastic theory for the case of S-waves propagating in a homogeneous infinite medium. He found that, for practical purposes, the viscous stress does not affect the fast S-wave, except for very high frequencies where the fluid strength is in the same order as that of the solid frame. In that range of frequencies, the fluid relaxes the wave amplitude generating an attenuation peak not observed in the Biot theory, which does not include the viscous stress tensor.

The existence of the slow S-wave affects the wave propagation across discontinuities due to the conversion scattering into this wave, as it was shown in the context of randomly inhomogeneous porous media (Müller and Sahay, 2011a). It results in attenuation and dispersion of the fast waves in the vicinity and above the Biot critical frequency (Müller and Sahay, 2011c). The analysis of Müller and Sahay shows the importance of including the conversion scattering into the slow S-wave on wave propagation. They define the dominant frequencies and the length of heterogeneities where such scattering is essential. However, they do not study the parameters that control the generation of the slow S-wave. Moreover, their analysis is limited to media with weak contrasts, which is not always the case in wave propagation. Thus, to understand the effects of the fluid viscous stress tensor, further studies are needed.

The reflection and transmission problem analysis is a classic topic for the understanding scattered waves at a discontinuity. To study the role of the fluid viscous stress tensor, the reflection and transmission solution for two porous media in impermeable contact is of particular interest. The impermeable surfaces enhance the generation of

the slow S-wave, since the fluid vorticity occur throughout the interface; hence, the implications of the fluid viscous stress tensor are more apparent. Furthermore, slow S-wave must be generated at any heterogeneity that causes a change in fluid motion, even if the surface is permeable.

1.1.4 Limited theoretical and experimental insights of scattering in impermeable surfaces

In the literature, there are a few reports on the scattering of poroelastic waves incident at an impermeable contact. On the Biot theory, Geerstma and Smit (1961) analyze a P-wave traveling in the normal direction across the interface between a solid and a poroelastic medium, where the solid is a natural impermeable medium. They conclude that a porous medium in contact with a solid behaves as a pure elastic solid. Afterward, Deresiewicz and Rice (1964) studied the same problem and found a slow P-wave of small amplitude generated at the impermeable surface. Meaning that the porous medium does not behave as an elastic solid.

The publications on experimental analysis of impermeable surfaces are also scarce. The first report is due to Rasolofosaon (1988). He propagates an ultrasonic pulse across a porous slab, with impermeable surfaces, immersed in a water tank. The pulse hits the surface of the porous slab, travels across it, and is recorded at a receiver placed a few centimeters away from the sample. The experiment is performed at different incident angles. Rasolofosaon reports that the response of a porous slab with sealed surfaces is close to an elastic solid, and the slow P-wave is not generated, as Geerstma and Smit (1961) predict. However, Rasolofosaon qualitatively shows that the amplitude observed was smaller than expected in the Biot theory. Afterward, Johnson et al. (1994) quantify the transmitted amplitude experimentally. It is similar to Rasolofosaon's (1988) experiment, focusing only on the normal incident angle. They show that the slow P-wave is generated even with an impermeable surface.

Although the scattering into the slow P-wave is reported by Geerstma and Smit (1961) (theoretically) and Johnson et al. (1994) (experimentally), both works are developed for a P-wave incident perpendicular to the surface. Thus, in this case, the slow S-wave cannot be generated at the interface because the particle motion is in the nor-

mal direction. In addition, the theoretical analysis is carried out in the framework of the Biot theory, which does not account for the viscous stress tensor. Therefore, even if their research is extended to non-normal incident angles, the fluid viscous stress tensor could not be captured because of the limitations of the Biot theory.

The published works on reflection and transmission solutions carried out in the dCS theory are also limited. The lone paper that solves the problem for a porous medium in contact with a solid medium is given by De la Cruz and Spanos (1992). That work aims to show the advantages of using the dCS poroelastic theory instead of the elastic approach. The results show all the poroelastic effects and do not distinguish between the consequences of the fluid viscous stress tensor and those caused by the contrast of elastic properties. Furthermore, De la Cruz and Spanos (1992) get the reflection and transmission solution for a virtual interface located in the zone where the mass is conserved instead of the physical contact of both porous media. This consideration leads to predictions that might be unphysical for the reflection and transmission coefficients.

The limited works in the literature evidence the need for an exhaustive study on the effect of viscous stresses. Such a study is not just an academic exercise, but it can improve the understanding of wave processes in reservoirs.

1.1.5   Geological context: permeable and impermeable boundaries

In sedimentary reservoirs, impermeable boundaries are not uncommon. In the petroleum geology research area, impermeable barriers and the factors that give their origin are well known (North, 1985). The shale and the clay content are the common materials causing impermeable surfaces. These surfaces appear in sandstone-shale successions, which are common in deltaic sequences. Also, in the sandstone formations, the deposition with clay breaks can cause horizontal impermeable surfaces that prevent fluid motion across the bedding. Even at the pore-scale, the presence of authigenic clay mineral generates impermeable zones. Furthermore, the scattering into the slow S-wave is not limited to the impermeable surfaces, but it is generated in all the heterogeneities. Thus, any change in porosity, permeability, saturating fluid, or elastic moduli within the reservoir can generate the slow S-wave by mode conversion. Therefore, the understanding of the fluid vorticity and the associated viscous forces

will help in the characterization of these reservoirs.

1.2 Thesis objectives and accomplishments

This thesis aims to study the role of the fluid viscous stress tensor on wave propagation in heterogeneous porous media to advance the understanding of attenuation mechanisms in reservoirs. I carry it out in two stages that define the specific objectives of the thesis. They are:

1. Study the effects of the fluid viscous stress tensor in the scattering of waves that travel across the planar contact of two porous-half spaces.

2. Analyze the effects of the fluid viscous stress tensor in wave propagation across a thin layered porous medium.

The former objective is performed by solving the reflection and transmission problem for two porous half-spaces in contact. The permeable and impermeable interfaces are considered because slow S-wave and viscous stress tensor effects exist in both cases. The first step for this analysis is to define the appropriated boundary condition, mainly for the tangential fluid motion associated with the fluid vorticity. The reflection and transmission solution in the welded contact of a solid and a porous half-space is developed to corroborate the boundary conditions proposed. It shows an unphysical motion of the fluid that violates the no-slip state if the viscous stress tensor is not accounted for.

Thereafter, the amplitude of waves scattered in the permeable/impermeable contact of two porous half-spaces is analyzed. The solutions in the dCS and Biot theories are contrasted in order to distinguish the effects of the viscous stress tensor. It proves that the viscous stress tensor affects the amplitude of all scattered waves, regardless of whether the contact is permeable or impermeable. But the effect is more profound in impermeable interfaces.

The second objective seeks to show the effects of the viscous stress tensor in media with many heterogeneities. The thin layered porous medium is considered because it is the simplest heterogeneous medium, with a common presence in reservoirs, that

can be analyzed semi-analytically. The amplitude of waves that travel across a stack of plane poroelastic layers is calculated using the reflectivity method. For this purpose, I have developed a reflectivity method algorithm for poroelastic layers with permeable or impermeable surfaces. It is implemented for dCS and Biot theories. To the best of my knowledge, it is the first algorithm in poroelasticity research that considers impermeable layers and can be used for all frequency regimes.

The wave amplitudes computed with the reflectivity method in the dCS theory show that the conversion scattering into the slow S-wave at each contact causes a decrement not observed in the Biot theory. This reduction is more significant for S-waves and also on impermeable surfaces. Even though it exists in all the cases, tt is observed that the number of contacts enhances that reduction, such that a vast number of heterogeneities has a larger effect on the viscous stress tensor.

1.3 Outline of thesis

Chapter 2 introduces the governing equation of the dCS poroelastic theory. It develops the solution for plane waves, and the dispersion relations of the poroelastic waves are analyzed. Also, the Biot theory is presented as a limit of the dCS theory where the viscous stress tensor vanishes. The boundary conditions for the permeable and impermeable contacts are presented in Chapter 3. This chapter shows that the boundary condition that accounts for the relative fluid motion in the tangential direction is only possible if the fluid viscous stress tensor is included. Chapter 4 analyzes the poroelastic reflection/transmission problem in planar contact with a solid half-space. It shows that the lack of that tensor, and the unconstrained fluid motion, leads to predict a relative fluid motion at the contact that violates the no-slip boundary condition. Then, Chapter 5 analyzes the scattered waves in a planar interface of two porous media from the reflection and transmission solution. Both permeable and impermeable contacts are considered. The effect of the fluid viscous stress tensor in waves that travel across a stack of thin porous layers is developed in Chapter 6. In such a stack, the effect of impermeable surfaces, permeable surfaces, and porosity variations is analyzed. Chapter 7 presents the impact of the fluid viscous stress tensor in attenuation. Finally, the discussions and concluding remarks are presented in Chapter 8.

Chapter 2.   Basics of poroelastic theory

This chapter introduces the poroelastic equations of motion and constitutive rela-
tions, in Cartesian coordinates, described in the dCS theory (de la Cruz and Spanos,
1985; Sahay et al., 2001). Using the definitions stated by Sahay (2008, 2013), these
equations are presented in a form that their comparison with the poroelastic theory
of Biot (1962) is straightforward (section 2.1). Herein, the index notation is used for
the stresses, strains, and displacement fields, with the italic sub-indices "*j, k, l, m,
n=x, y, z*". The roman sub-indices are used to distinguish between scalar variables.
The variables u_j^s and w_j, with a single sub-index, are used for the displacement fields,
and these variables with double sub-indices, i.e., u_{jk}^s and w_{jk}, define their associated
strain tensors. The gradient ($\nabla x = x_{,j}$), divergence ($\nabla \cdot \vec{x} = x_{j,j}$), curl ($\nabla \times \vec{x} = \epsilon_{jkl} x_{k,l}$),
double curl ($\nabla \times (\nabla \times \vec{x}) = \epsilon_{jkl} \epsilon_{kmn} x_{m,nl}$), and Laplacian ($\nabla^2 x = x_{,kk}$ or $\nabla^2 = \partial_j \partial_j$) linear
differential operators are also presented in index notation. Boldface letters are used
to represent matrices. The sub-indices j, k, and l in matrices indicate the sub-indices
of each element of the matrix.

Section 2.2 develops the plane wave solution for the poroelastic wave equations
of motion in the frequency domain. The methodology used for the solution has been
previously presented for cylindrical (Solorza and Sahay, 2009; Gonzalez, 2017) and
Cartesian (Sahay, 2008; Sanchez, 2010) geometries. However, for completeness of
the work, this methodology is also presented. In section 2.3 the relation between dCS
and Biot theories is shown. Finally, the dispersion relations of the existing waves are
described in section 2.4.

2.1 The dCS poroelastic theory

2.1.1 Governing equations

The poroelastic theory is constructed in terms of the average motions of the solid
and fluid parts; however, it is commonly described in terms of the solid-frame dis-
placement (u_j^s) and the relative motion of the fluid with respect to the solid frame
($w_j = \eta_0 (u_j^f - u_j^s)$, where η_0 is the unperturbed porosity), which is referred to as the
filtration displacement field (Biot, 1962). In terms of these fields, the equations of

motion, expressed in matrix notation, are

$$
\left[\begin{pmatrix} \rho^{\circ}_{\mathrm{m}} & \rho^{\circ}_{\mathrm{f}} \\ \rho^{\circ}_{\mathrm{f}} & \frac{S}{\eta_0}\rho^{\circ}_{\mathrm{f}} \end{pmatrix} \underbrace{\quad}_{\boldsymbol{\rho}} \frac{\partial^2}{\partial t^2} + \frac{\rho^{\circ}_{\mathrm{f}}}{\eta_0}\Omega_{\mathrm{b}} \begin{pmatrix} 0 & 0 \\ 0 & 1 \end{pmatrix} \frac{\partial}{\partial t} \right] \underbrace{\begin{pmatrix} u^{\mathrm{s}}_j \\ w_j \end{pmatrix}}_{\mathbf{u}_j} = \begin{pmatrix} \tau_{jk,k} \\ \sigma^{\mathrm{f}}_{jk,k} \end{pmatrix} + \begin{pmatrix} \rho^{\circ}_{\mathrm{m}} \\ \rho^{\circ}_{\mathrm{f}} \end{pmatrix} F_j .
\tag{1}
$$

Herein $\rho^{\circ}_{\mathrm{m}} = \phi_0\rho^{\circ}_{\mathrm{s}} + \eta_0\rho^{\circ}_{\mathrm{f}}$ is the unperturbed bulk density of the porous medium, $\rho^{\circ}_{\mathrm{s}}$ and $\rho^{\circ}_{\mathrm{f}}$ are, respectively, the unperturbed densities of the solid mineral and the fluid. The term η_0 is the porosity and $\phi_0 = 1 - \eta_0$ is the volume fraction of the solid. The term S is the tortuosity of the pore space, and $\Omega_{\mathrm{b}} = \eta_0\nu_{\mathrm{f}}/\kappa$ is a lumped parameter that has dimension of frequency and can be viewed as the weighted hydraulic conductivity. ν_{f} is the pore-fluid kinematic shear viscosity and κ is the permeability. F_j is the external body force.

The tensors $\tau_{jk} = \tau^{\mathrm{s}}_{jk} + \tau^{\mathrm{f}}_{jk}$ and $\sigma^{\mathrm{f}}_{jk} = \tau^{\mathrm{f}}_{jk}/\eta_0$ are, respectively, the total and the pore-fluid stresses, and τ^{s}_{jk} and τ^{f}_{jk} are the volume averaged solid and fluid stresses. They are related to the porous deformation by the poroelastic constitutive relations in this framework, as

$$
\underbrace{\begin{pmatrix} \tau_{jk} \\ \sigma^{\mathrm{f}}_{jk} \end{pmatrix}}_{\boldsymbol{\tau}_{jk}} = \left(\mathbf{K} + \boldsymbol{\xi}\frac{\partial}{\partial t} \right) \begin{pmatrix} u^{\mathrm{s}}_{ll} \\ w_{ll} \end{pmatrix} \delta_{jk} + 2 \left(\boldsymbol{\mu} + \boldsymbol{\nu}\frac{\partial}{\partial t} \right) \begin{pmatrix} \breve{u}^{\mathrm{s}}_{jk} \\ \breve{w}_{jk} \end{pmatrix} ,
\tag{2}
$$

where

$$
\mathbf{K} = \begin{pmatrix} K^{\star}_{\mathrm{ud}} & \alpha^{\star}M^{\star} \\ \alpha M^{\star} & M^{\star} \end{pmatrix} ,
\tag{3}
$$

$$
\boldsymbol{\xi} = \begin{pmatrix} \alpha & 1 \\ \alpha/\eta_0 & 1/\eta_0 \end{pmatrix} \frac{\eta_0 M^{\star}}{K_{\mathrm{f}}} \xi_{\mathrm{f}} ,
\tag{4}
$$

$$
\boldsymbol{\mu} = \begin{pmatrix} 1 & 0 \\ 0 & 0 \end{pmatrix} \mu_0 ,
\tag{5}
$$

and

$$
\boldsymbol{\nu} = \begin{pmatrix} \alpha_\mu & 1 \\ \alpha_\mu/\eta_0 & 1/\eta_0 \end{pmatrix} \mu_{\mathrm{f}} .
\tag{6}
$$

The terms $u^s_{jk} = \frac{1}{2}\left(u^s_{j,k} + u^s_{k,j}\right)$ and $w_{jk} = \frac{1}{2}\left(w_{j,k} + w_{k,j}\right)$ are, respectively, the solid-frame and filtration strain tensors. The elements $\breve{u}^s_{jk}$ and $\breve{w}_{jk}$ are the trace free part of solid-frame and filtration strain tensors, respectively. The term $K_0 + \alpha\alpha^*M^* \equiv K^\star_{ud}$ is the bulk modulus of the undrained porous medium. K_0 is the bulk modulus of the solid frame, i.e., the bulk modulus for the porous frame without any saturating fluid. The term $\alpha \equiv \eta_0 + \phi_0\delta_{K_s}$ is the Biot bulk coefficient, $\eta_0 + \phi_0\delta_{K_s}n \equiv \alpha^*$ is the effective pressure coefficient for bulk volume, n is a non-dimensional coefficient that describes the effective pressure for porosity, and $\frac{1}{M^*} = \frac{\eta_0}{K_f} + n\frac{\alpha-\eta_0}{K_s}$ is defined as the generalized fluid storage coefficient (Sahay, 2013). K_s corresponds to the bulk modulus of the solid part if it has no pores, i.e., the bulk modulus of the solid mineral, and K_f is the bulk modulus of the pore-fluid. The bulk modulus of the solid mineral and that of the solid-frame are related as $\phi_0(1-\delta_{K_s})K_s \equiv K_0$. So, δ_{K_s} is interpreted as the Bulk modulus decrement parameter of solid-frame. μ_0 is the shear modulus of the solid-frame, and it is related to the shear modulus of the solid mineral as $\phi_0(1-\delta_{\mu_s})\mu_s \equiv \mu_0$. δ_{μ_s} is interpreted as the shear modulus decrement parameter of the solid-frame, and $\eta_0 + \phi_0\delta_{\mu_s} \equiv \alpha_\mu$ is the Biot shear coefficient (Sahay, 2008). The terms ξ_f and μ_f are the bulk and shear viscosity of the pore-fluid, respectively.

By substituting the constitutive relations 2 into the equations of motion 1, they are written as

$$\left(\mathbf{I}\frac{\partial^2}{\partial t^2} + \Omega_i\mathbf{D}\frac{\partial}{\partial t}\right)\begin{pmatrix} u^s_j \\ w_j \end{pmatrix} = \left(\mathbf{C}_\alpha + \mathbf{N}_\alpha\frac{\partial}{\partial t}\right)\begin{pmatrix} u^s_{l,lj} \\ w_{l,lj} \end{pmatrix} - \left(\mathbf{C}_\beta + \mathbf{N}_\beta\frac{\partial}{\partial t}\right)\begin{pmatrix} \epsilon_{jkl}\epsilon_{kmn}u^s_{m,nl} \\ \epsilon_{jkl}\epsilon_{kmn}w_{m,nl} \end{pmatrix}. \tag{7}$$

Herein $\mathbf{I}$ is the 2×2 identity matrix, $\Omega_i = \Omega_b/(S - m_f)$ is the Biot critical frequency, which marks the transition from low- to high-frequency regime, and $m_f = \eta_0\rho^\circ_f/\rho^\circ_m$ is the fluid mass fraction (the equivalent mass fraction for the solid is $m_s = \phi_0\rho^\circ_s/\rho^\circ_m$). The matrices $\mathbf{D}$, $\mathbf{C}_\alpha$, $\mathbf{N}_\alpha$, $\mathbf{C}_\beta$, and $\mathbf{N}_\beta$ are

$$\mathbf{D} = \begin{pmatrix} 0 & -\frac{m_f}{\eta_0} \\ 0 & 1 \end{pmatrix}, \tag{8}$$

$$\mathbf{C}_\alpha = \boldsymbol{\rho}^{-1}\left(\mathbf{K} + \frac{4}{3}\boldsymbol{\mu}\right), \tag{9}$$

$$\mathbf{N}_\alpha = \boldsymbol{\rho}^{-1}\left(\boldsymbol{\xi} + \frac{4}{3}\boldsymbol{\nu}\right), \tag{10}$$

$$\mathbf{C}_{\beta} = \boldsymbol{\rho}_{\mathrm{d}}^{-1}\boldsymbol{\mu}, \tag{11}$$

and

$$\mathbf{N}_{\beta} = \boldsymbol{\rho}^{-1}\boldsymbol{\nu}. \tag{12}$$

The matrices $\mathbf{C}_{\alpha}$ and $\mathbf{N}_{\alpha}$ are associated with compressional processes, whereas $\mathbf{C}_{\beta}$ and $\mathbf{N}_{\beta}$ are related to shear processes. The elements of $\mathbf{C}_{\alpha}$ and $\mathbf{C}_{\beta}$ matrices have the dimension of velocity squared. The elements of $\mathbf{N}_{\alpha}$ and $\mathbf{N}_{\beta}$ have the dimension of kinematic viscosity.

2.1.2 Frequency domain representation

The poroelastic equations of motion (equation 7) in frequency domain are

$$\boldsymbol{\alpha}\begin{pmatrix} u^{\mathrm{s}}_{l,lj} \\ w_{l,lj} \end{pmatrix} - \boldsymbol{\beta}\begin{pmatrix} \epsilon_{jkl}\epsilon_{kmn}u^{\mathrm{s}}_{m,nl} \\ \epsilon_{jkl}\epsilon_{kmn}w_{m,nl} \end{pmatrix} + \omega^2\begin{pmatrix} u^{\mathrm{s}}_{j} \\ w_j \end{pmatrix} = 0, \tag{13}$$

where $\boldsymbol{\alpha}$ and $\boldsymbol{\beta}$ are non-symmetric 2 by 2 matrices associated with P- and S-waves, respectively, whose elements are dimensionally equal to velocity squared. They are

$$\boldsymbol{\alpha} = \boldsymbol{\Omega}^{-1}\left(\mathbf{C}_{\alpha} - i\omega\mathbf{N}_{\alpha}\right) \equiv \begin{pmatrix} \alpha_{11} & \alpha_{12} \\ \alpha_{12} & \alpha_{22} \end{pmatrix}, \tag{14}$$

$$\boldsymbol{\beta} = \boldsymbol{\Omega}^{-1}\left(\mathbf{C}_{\beta} - i\omega\mathbf{N}_{\beta}\right) \equiv \begin{pmatrix} \beta_{11} & \beta_{12} \\ \beta_{22} & \beta_{22} \end{pmatrix}, \tag{15}$$

where $\boldsymbol{\Omega}$ is a 2×2 matrix associated with the Biot relaxation frequency Ω_{i}

$$\boldsymbol{\Omega} = \mathbf{I} + i\frac{\Omega_{\mathrm{i}}}{\omega}\mathbf{D}. \tag{16}$$

Using the definition of the $\boldsymbol{\alpha}$ and $\boldsymbol{\beta}$ matrices, the constitutive relations in frequency domain read as

$$\begin{pmatrix} \tau_{jk} \\ \sigma^{\mathrm{f}}_{jk} \end{pmatrix} = \boldsymbol{\rho}\boldsymbol{\Omega}\left[(\boldsymbol{\alpha} - 2\boldsymbol{\beta})\begin{pmatrix} u^{\mathrm{s}}_{ll} \\ w_{ll} \end{pmatrix}\delta_{jk} + 2\boldsymbol{\beta}\begin{pmatrix} u^{\mathrm{s}}_{jk} \\ w_{jk} \end{pmatrix}\right]. \tag{17}$$

2.2 Plane wave propagation in a homogeneous medium

To develop the plane wave solution of the equations of motion 13 for a homogeneous isotropic poroelastic medium, let us consider the Cartesian coordinates with the wave motion independent of the y-coordinate. In such a case, the horizontally polarized shear- (SH-) waves decouple in the y-direction, and the compressional (P-) and vertically polarized shear (SV-) waves are constrained to the *x-z* plane.

2.2.1 Plane wave solution for SH-waves

The equations of motion for SH-waves are a coupled system of two Helmholtz equations. In matrix form it reads as

$$\boldsymbol{\beta}\nabla^2\mathbf{u}_y + \omega^2\mathbf{u}_y = 0, \tag{18}$$

which are decoupled by the transformation

$$\mathbf{u}_y = \begin{pmatrix} u_y^s \\ w_y \end{pmatrix} = \mathbf{R}_\beta\Xi = \underbrace{\begin{pmatrix} 1 & \gamma_{\beta_{\mathrm{II}}} \\ \gamma_{\beta_{\mathrm{I}}} & 1 \end{pmatrix}}_{\mathbf{R}_\beta} \underbrace{\begin{pmatrix} \Xi_{\mathrm{I}} \\ \Xi_{\mathrm{II}} \end{pmatrix}}_{\Xi}. \tag{19}$$

$\mathbf{R}_\beta$ is the right-eigenvector matrix of $\boldsymbol{\beta}$. The elements Ξ_{I} and Ξ_{II} are the decoupled potentials for the SH wave modes existing in the poroelastic medium, and they are called fast and slow SH-waves, respectively. The terms $\gamma_{\beta_{\mathrm{I}}} = \beta_{21}/(\beta_{\mathrm{I}}^2 - \beta_{22})$ and $\gamma_{\beta_{\mathrm{II}}} = (\beta_{\mathrm{II}}^2 - \beta_{22})/\beta_{12}$ are the ratio of filtration to solid-frame fields generated by the fast S-wave and the ratio of solid-frame to filtration field generated by the slow S-wave, respectively.

$\mathbf{R}_\beta$ diagonalizes the $\boldsymbol{\beta}$ matrix as

$$\mathbf{L}_\beta^{\mathsf{T}}\boldsymbol{\beta}\mathbf{R}_\beta = \boldsymbol{\Lambda}_\beta \equiv \begin{pmatrix} \beta_{\mathrm{I}}^2 & 0 \\ 0 & \beta_{\mathrm{II}}^2 \end{pmatrix}, \tag{20}$$

where, $\mathbf{L}_\beta^{\mathsf{T}} = \mathbf{R}_\beta^{-1}$ is the left eigenvector matrix. The elements β_{I}^2 and β_{II}^2 are, respectively, the square velocity of the fast (S_{I}) and slow (S_{II}) S-waves, and they are the eigenvalues of the $\boldsymbol{\beta}$ matrix.

By substituting equation 19 into 18, followed by the application of $\mathbf{L}_\beta^\mathsf{T}$ upon it from the left, yields to the following set of two decoupled scalar Helmholtz equations

$$\left(\mathbf{\Lambda}_\beta \nabla^2 + \omega^2 \mathbf{I}\right) \mathbf{\Xi} = \mathbf{0}. \tag{21}$$

The plane wave solution for equation 21 is

$$\mathbf{\Xi}^\pm = \begin{pmatrix} \Xi_\mathrm{I}^\pm \\ \Xi_\mathrm{II}^\pm \end{pmatrix} = e^{i\omega p x} \begin{pmatrix} e^{\pm i\omega q_{\beta_\mathrm{I}} z} & 0 \\ 0 & e^{\pm i\omega q_{\beta_\mathrm{II}} z} \end{pmatrix} \begin{pmatrix} b_\mathrm{I}^\pm \\ b_\mathrm{II}^\pm \end{pmatrix} = e^{i\omega(p x \mathbf{I} \pm \mathbf{Q}_\beta z)} \mathbf{b}^\pm, \tag{22}$$

The ± sign determines the up-going (-) and down-going (+) wavefields. The horizontal slownesses p is the free parameter. The terms $q_{\beta_\mathrm{I}}^2 = \beta_\mathrm{I}^{-2} - p^2$ and $q_{\beta_\mathrm{II}}^2 = \beta_\mathrm{II}^{-2} - p^2$ are the squared vertical slownesses for the fast and slow S-waves, respectively. The terms b_I and b_II are displacement amplitudes for the fast and slow S-waves, respectively.

The stresses generated by the SH-wave solution 22 are only

$$\boldsymbol{\tau}_{yz} = \pm \boldsymbol{\rho} \, \mathbf{\Omega} \mathbf{R}_\beta \mathbf{\Lambda}_\beta \mathbf{Q}_\beta \mathbf{\Xi}^\pm. \tag{23}$$

Herein, the relation 20 is used to change $\boldsymbol{\beta} \mathbf{R}_\alpha = \mathbf{R}_\alpha \mathbf{\Lambda}_{\boldsymbol{\beta}}$.

2.2.2 Plane wave solution for P-SV waves

The P- and SV-waves can be decoupled by applying a potential decomposition as

$$\mathbf{u} = \underbrace{\begin{pmatrix} \nabla \Phi_\mathrm{s} \\ \nabla \Phi_\mathrm{w} \end{pmatrix}}_{\mathbf{L}} + \underbrace{\begin{pmatrix} \nabla \times (\nabla \times (\hat{e}_z \Psi_\mathrm{s})) \\ \nabla \times (\nabla \times (\hat{e}_z \Psi_\mathrm{w})) \end{pmatrix}}_{\mathbf{N}} \tag{24}$$

$\mathbf{L}$ and $\mathbf{N}$ are a generalization of the Hansen vectors (Ben-Menahem, 1981). $\mathbf{L}$ is a curl-free vector that represents compressional motion, and $\mathbf{N}$ is a divergence-free vector related to shear waves.

Substituting the vector decomposition 24 in the equations of motion 13 leads to

two systems of two Helmholtz equations. They are

$$\left(\boldsymbol{\alpha}\nabla^2 + \omega^2\mathbf{I}\right)\underbrace{\begin{pmatrix} \Phi_s \\ \Phi_w \end{pmatrix}}_{\boldsymbol{\Phi}} = \mathbf{0}, \tag{25}$$

and

$$\left(\boldsymbol{\beta}\nabla^2 + \omega^2\mathbf{I}\right)\underbrace{\begin{pmatrix} \Psi_s \\ \Psi_w \end{pmatrix}}_{\boldsymbol{\Psi}} = \mathbf{0}, \tag{26}$$

where $\boldsymbol{\Phi}$ and $\boldsymbol{\Psi}$ are the P- and S-potentials, respectively.

2.2.2.1 Plane wave solution for decoupled P potentials

As with the SH-waves, the matrix Helmholtz equations for P-potentials (equation 25) are decoupled by the transformation

$$\boldsymbol{\Phi} = \mathbf{R}_\alpha\boldsymbol{\phi} = \underbrace{\begin{pmatrix} 1 & \gamma_{\alpha_{\mathrm{II}}} \\ \gamma_{\alpha_{\mathrm{I}}} & 1 \end{pmatrix}}_{\mathbf{R}_\alpha}\underbrace{\begin{pmatrix} \phi_{\mathrm{I}} \\ \phi_{\mathrm{II}} \end{pmatrix}}_{\boldsymbol{\phi}}. \tag{27}$$

Herein, $\mathbf{R}_\alpha$ is the right-eigenvector matrix of the $\boldsymbol{\alpha}$ matrix. The elements ϕ_{I} and ϕ_{II} are the decoupled potentials for the compressional wave modes existing in a poroelastic medium, and they are called fast and slow P-waves, respectively. The terms $\gamma_{\alpha_{\mathrm{I}}} = (\alpha_{\mathrm{I}}^2 - \alpha_{11})/\alpha_{12}$ and $\gamma_{\alpha_{\mathrm{II}}} = \alpha_{12}/(\alpha_{\mathrm{II}}^2 - \alpha_{11})$ defines, respectively, the ratio of filtration field to solid-frame field generated by the fast P wave and the ratio of solid-frame to filtration field generated by the slow P wave.

$\mathbf{R}_\alpha$ diagonalizes the $\boldsymbol{\alpha}$ matrix as

$$\mathbf{L}_\alpha^\mathsf{T}\,\boldsymbol{\alpha}\,\mathbf{R}_\alpha = \boldsymbol{\Lambda}_\alpha \equiv \begin{pmatrix} \alpha_{\mathrm{I}}^2 & 0 \\ 0 & \alpha_{\mathrm{II}}^2 \end{pmatrix}, \tag{28}$$

where, $\mathbf{L}_\alpha^\mathsf{T} = \mathbf{R}_\alpha^{-1}$ is the left eigenvector matrix. The elements α_{I}^2 and α_{II}^2 are, respectively, the square velocity of the fast (P_{I}) and slow (P_{II}) P-waves, and they are the eigenvalues of the $\boldsymbol{\alpha}$ matrix.

By substituting equation 27 into 25, followed by the application of $\mathbf{L}_\alpha^\mathsf{T}$ upon it from the left, yields to the following set of two decoupled scalar Helmholtz equations

$$\left(\mathbf{\Lambda}_\alpha \nabla^2 + \omega^2 \mathbf{I}\right)\boldsymbol{\phi} = \mathbf{0}. \tag{29}$$

The plane wave solution for equation 29 is

$$\boldsymbol{\phi}^\pm = \begin{pmatrix} \phi_\mathrm{I}^\pm \\ \phi_\mathrm{II}^\pm \end{pmatrix} = e^{i\omega px}\begin{pmatrix} e^{\pm i\omega q_{\alpha_\mathrm{I}}z} & 0 \\ 0 & e^{\pm i\omega q_{\alpha_\mathrm{II}}z} \end{pmatrix}\begin{pmatrix} a_\mathrm{I}^\pm \\ a_\mathrm{II}^\pm \end{pmatrix} = e^{i\omega(px\mathbf{I}\pm\mathbf{Q}_\alpha z)}\,\mathbf{a}^\pm, \tag{30}$$

The terms $q_{\alpha_\mathrm{I}}^2 = \alpha_\mathrm{I}^{-2} - p^2$ and $q_{\alpha_\mathrm{II}}^2 = \alpha_\mathrm{II}^{-2} - p^2$ are the squared vertical slownesses for the fast and slow P-waves, respectively. The terms a_I and a_II are potential amplitudes for the fast and slow P-waves, respectively.

2.2.2.2 Plane wave solution for decoupled S potentials

The S-potentials (equation 26) obey the same matrix Helmholtz equations that the SH waves (equation 18); therefore, S-potentials have the same solution. Thus, after the transformation $\mathbf{\Psi} = \mathbf{R}_\beta \boldsymbol{\psi}$, the solutions for S-potentials are

$$\boldsymbol{\psi}^\pm = \begin{pmatrix} \psi_\mathrm{I}^\pm \\ \psi_\mathrm{II}^\pm \end{pmatrix} = e^{i\omega px}\begin{pmatrix} e^{\pm i\omega q_{\beta_\mathrm{I}}z} & 0 \\ 0 & e^{\pm i\omega q_{\beta_\mathrm{II}}z} \end{pmatrix}\begin{pmatrix} b_\mathrm{I}^\pm \\ b_\mathrm{II}^\pm \end{pmatrix} = e^{i\omega(px\mathbf{I}\pm\mathbf{Q}_\beta z)}\,\mathbf{b}^\pm. \tag{31}$$

In this case, the terms b_I and b_II are potential amplitudes for the fast and slow S-waves, respectively.

2.2.2.3 Displacements and stresses in terms of decoupling potentials

Substituting the solutions 30 and 31 for potentials into equation 24, the expressions of displacements are

$$\mathbf{u}_z = \pm i\omega \mathbf{R}_\alpha \mathbf{Q}_\alpha \boldsymbol{\phi}^\pm + i\omega p \mathbf{R}_\beta \boldsymbol{\psi}^\pm . \tag{32}$$

$$\mathbf{u}_x = i\omega p \mathbf{R}_\alpha \boldsymbol{\phi}^\pm \mp i\omega \mathbf{R}_\beta \mathbf{Q}_\beta \boldsymbol{\psi}^\pm , \tag{33}$$

Thereafter, substituting the above solutions in the constitutive relations 17, and using the relation 20 to change $\boldsymbol{\beta}\mathbf{R}_\alpha = \mathbf{R}_\alpha\boldsymbol{\Lambda_\beta}$, the stresses generated by the P-SV waves are

$$\boldsymbol{\tau}_{zz} = -\omega^2\boldsymbol{\rho}\boldsymbol{\Omega}\big[(\mathbf{I}-2p^2\boldsymbol{\beta})\,\mathbf{R}_\alpha\boldsymbol{\phi}^\pm \pm 2p\mathbf{R}_\beta\boldsymbol{\Lambda}_\beta\mathbf{Q}_\beta\boldsymbol{\psi}^\pm\big], \tag{34}$$

$$\boldsymbol{\tau}_{xz} = -\omega^2\boldsymbol{\rho}\boldsymbol{\Omega}[\pm 2p\boldsymbol{\beta}\mathbf{R}_\alpha\mathbf{Q}_\alpha\boldsymbol{\phi}^\pm - \mathbf{R}_\beta\left(\mathbf{I}-2p^2\boldsymbol{\Lambda}_\beta\right)\boldsymbol{\psi}^\pm]. \tag{35}$$

2.3   Biot theory as a limiting case of the dCS theory

The poroelastic equations of motion in the Biot theory have the same form as equation 1. However, the definition of stresses is different in each theory. It is because of two main reasons: (i) the Biot theory assumes a reciprocal interaction at the pore surface, and (ii) the Biot constitutive relations ignore the fluid viscous stress tensor. The last one is stated under the assumption that the fluid viscous forces are fully captured by the fluid mobility term, the first derivative in time of the equation of motion 1, as it is considered in steady-state flow analyses using Darcy law.

The reciprocal interaction at the pore surface describes a specific deformation in which, for a fluid-saturated porous medium subjected to an equal increment of the confining and pore pressures, that is, the unjacketed experiment, the amount of deformation undergone by the bulk volume is equal to that at the pore volume. This limit is constructed in the dCS theory by setting the effective pressure coefficient for the porosity equal to one ($n = 1$). Once n is set to one, the constitutive relations in the Biot theory can be recovered from equation 2, ignoring the strain rate terms. That is, by vanishing the fluid viscosities ξ_f and μ_f in the matrices $\boldsymbol{\xi}$ and $\boldsymbol{\nu}$ of the constitutive relations, respectively. In this limit, the constitutive relations become

$$\begin{pmatrix} \tau_{jk} \\ \sigma^f_{jk} \end{pmatrix} = \mathbf{K}\begin{pmatrix} u^s_{ll} \\ w_{ll} \end{pmatrix}\delta_{jk} + 2\boldsymbol{\mu}\begin{pmatrix} \breve{u}^s_{jk} \\ \breve{w}_{jk} \end{pmatrix}. \tag{36}$$

Vanishing μ_f in the matrix $\boldsymbol{\nu}$ has a strong impact on the description of shear processes. It is apparent in the SH-wave equation 18 that, in this limit, is given by

$$\begin{pmatrix} \mu_0 & 0 \\ 0 & 0 \end{pmatrix}\nabla^2\begin{pmatrix} u^s_y \\ w_y \end{pmatrix} + \omega^2\begin{pmatrix} \rho_m & \rho_f \\ \rho_f & \frac{\rho_f}{\eta_0}\left(S + i\frac{\Omega_b}{\omega}\right) \end{pmatrix}\begin{pmatrix} u^s_y \\ w_y \end{pmatrix} = 0. \tag{37}$$

From the second equation of the system of equations 37 one finds that the filtration and solid-frame displacement fields are not independent. Instead, they are related as

$$w_y = \gamma_{\text{Biot}} u_y^s,$$

(38)

with the coefficient of proportionality

$$\gamma_{\text{Biot}} = -\frac{\eta_0/S}{1 + i\frac{\Omega_b/S}{\omega}}.$$

(39)

Utilizing the dependence of the two fields (equation 38), from the first equation of the system of equations 37, the equation of motion for the solid-frame becomes

$$\left(\beta_{\text{Biot}}^2 \nabla^2 + \omega^2\right) u_y^s = 0,$$

(40)

with

$$\beta_{\text{Biot}}^2 = \frac{\mu_0}{\rho_m + \rho_f \gamma_{\text{Biot}}},$$

(41)

where β_{Biot} is read off as the shear wave velocity. Thus, there is only one shear wave, and the slow S-wave does not appear. Equation 38 also implies that the shear motion for the filtration field is governed by the same wave equation 40. Thus, the diffusive nature of shear motion within the viscous fluid (the vorticity) is not accounted for.

The plane wave solution of equation 40 is

$$u_y^s = b^\pm e^{i\omega(px \pm q_{\beta_{\text{Biot}}} z)}.$$

(42)

Here, $q_{\beta_{\text{Biot}}}^2 = \beta_{\text{Biot}}^{-2} - p^2$ is the vertical slowness for the S-wave in the Biot theory.

The compressional waves are affected by the lack of both viscosities, ξ_f and μ_f. However, its effects are not as pronounced as in the S waves. The solution keeps the same form as equation 30, with a change in the definition of $\boldsymbol{\alpha}$ matrix that does not contain the matrix $\boldsymbol{\xi}$ in the Biot theory. The effects of these differences are shown in section 2.4.

2.3.1 The Johnson-Koplik-Dashen dynamic permeability model

In a porous medium, at sufficiently low frequencies, the viscous skin depth of the fluid shear motion greatly exceeds any characteristic pore-throat size (Λ). Therefore, one expects that the fluid moves in unison with the solid frame during shear excitation. At higher frequencies, when the viscous skin depth becomes comparable or smaller than Λ, viscous boundary layers develop in the vicinity of pore interfaces. Then, the unison shearing motion of solid-frame and fluid is no longer possible. Instead, the fluid develops a shear motion independent of the solid-frame shearing. Biot (1956b) pointed out the need for an additional term to capture the fluid shear motion in the high-frequency regime. He proposed to incorporate this effect by including a viscodynamic correction factor in the Darcy term of fluid mobility. This factor is alternatively incorporated into the poroelastic equations of motion by making the permeability frequency-dependent (Johnson et al., 1987). It is known as the Johnson-Koplik-Dashen dynamic permeability (JKD) and is given by

$$\kappa(\omega) = \frac{\kappa}{\left(1 - 4i\frac{\omega}{\Omega_b}\frac{\kappa S^2}{\eta_0 \Lambda^2}\right)^{1/2}} \, , \tag{43}$$

where $2/\Lambda$ is the dynamically weighted surface to pore volume ratio. Λ characterize the average pore-throat diameter.

The inclusion of the JKD term into the Biot poroelastic theory only modifies the first derivative in time of the equation of motion (the Ω_b term changes). However, the rest of the equations remains unaffected, even the fluid stress.

2.4 Poroelastic dispersion relations

The poroelastic dispersion relations describe the frequency-dependent behavior of the waves. This section analyzes such behavior for the waves in the dCS and Biot theories. For that, the dispersion relations are computed in MATLAB using the properties of the sintered glass beads porous media as in Bouzidi and Schmitt (2012). Those properties are presented in Appendix A. The pseudocode of MATLAB function is described in section 1 of Appendix B.

2.4.1 Fast S-wave

The phase velocity for the fast S-wave (left panel of figure 3) shows three distinct regimes separated by the Biot critical frequency (Ω_i) and the saturated-frame relaxation frequency for S-waves ($\Omega_\beta = \mu_0/\mu_f$). Ω_i marks the transition from the viscous to the inertial coupling of the fluid to the solid frame. Whereas Ω_β marks the critical point where the fluid shear strength is equal to that in the solid frame, and it causes a relaxation of the shearing of porous media. Above this critical frequency, the description of fluid-solid frame interaction at the pore surface has to be modified since the current poroelastic theories consider that the fluid shearing does not affect the solid frame, an assumption that is not valid at or above Ω_β. However, I show the value of velocity and attenuation at those frequencies for completeness.

The inverse of quality factor (right panel of Figure 3) shows two peaks in the critical frequencies. The peak at Ω_i is generated by the Darcy relaxation, and the one at Ω_β is generated by the intrinsic fluid viscous relaxation. The geometric average of Ω_i and Ω_β, $\Omega_\beta^\dagger$, marks the frequency beyond which intrinsic viscous relaxation of the pore fluid takes over the Darcy relaxation.

To compare the dispersion relation with that described in the Biot theory, I present it by the red dashed line. In contrast with the dCS theory, there are only two regimes in the S wave predicted in the Biot theory, below and above Ω_i. The Biot S-wave does not show the solid frame relaxation frequency Ω_β, and it is equivalent to the fast S-wave in dCS theory at frequencies below $\Omega_\beta^\dagger$.

The approximations for shear velocities at regimes below Ω_β are presented in Sahay (2008). Those approximations for the fast S-wave velocity are

$$\beta_I^2 \approx \begin{cases} \beta_c^2\left(1 - i\frac{\omega}{\Omega_i}d_f m_f\right) & \omega \ll \Omega_i, \\[2em] \frac{\beta_c^2}{1-\frac{m_f}{S}}\left(1 - i\frac{m_f}{S}\frac{\Omega_i}{\omega} - i\frac{\omega}{\Omega_\beta}\left(\frac{\eta_0}{S}\frac{m_s}{m_f} + \alpha_\mu\left(1 - \frac{1}{S}\right)\right)\right) & \Omega_i \ll \omega \ll \Omega_\beta, \end{cases} \tag{44}$$

where $\beta_c = \sqrt{\mu_0/\rho_m}$ is the Gassmann shear velocity.

The asymptotic form of the dispersion relation 44 shows that, in the low-frequency regime ($\omega \ll \Omega_i$), the fluid is viscously coupled to the solid frame causing a behavior

as an effective elastic medium. However, as the coupling is not perfect, the inverse quality factor increases with frequency. In the high-frequency regime ($\Omega_i \ll \omega \ll \Omega_\beta$), the fluid is coupled only in the vicinity of the pore-wall, causing a relative motion of the fluid with respect to the solid frame. It causes a reduction in the effective density that increases the phase velocity. The inverse quality factor decreases with frequency until $\Omega_\beta^\dagger$, after which it increases until it achieves the peak at Ω_β (Figure 3).
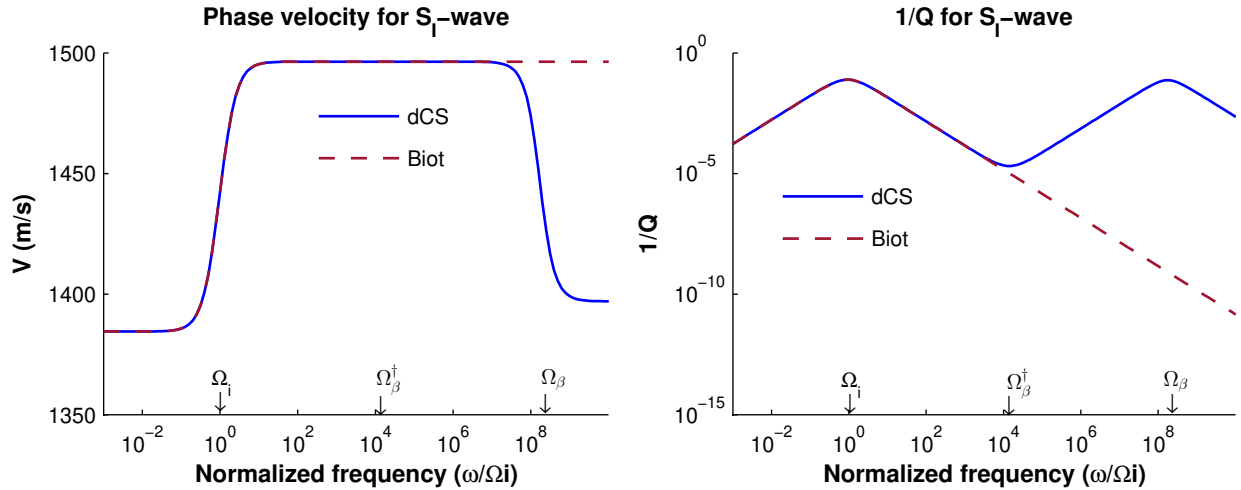
Figure 3. Dispersion relation for the fast S wave. The phase velocity is on the left side, and the inverse quality factor is on the right side.

2.4.2 Slow-S wave

The dispersion relation for the slow S-wave is shown in figure 4. This wave shows only two regimes, the low- and high-frequency regimes. In the low-frequency regime, the slow S-wave has the behavior of a damped diffusive wave. Herein, the velocity is very slow and is strongly attenuated. It is because the fluid is viscously coupled to the solid frame, and this coupling annihilates the fluid vorticity. As the frequency increase above Ω_i, the fluid decouples from the solid frame, and it allows the development of fluid vorticity. In the high-frequency regime, the slow S-wave behaves as a diffusive wave. It shows a phase velocity that increases with frequency (left panel of figure 4) and an inverse quality factor around two ($1/Q \approx 2$), characteristics of a diffusive wave.

The approximation for the slow S-wave dispersion relation is also presented in Sahay (2008) for $\omega < \Omega_\beta$. These approximations are

$$\beta_{\mathbb{II}}^2 \approx \begin{cases} -\omega^2 \frac{\kappa}{\eta_0}\left(1 + i\omega \frac{\kappa}{\eta_0 \nu_f}S\right), & \omega \ll \Omega_i \ll \Omega_\beta. \\[3mm] -i\frac{\omega \nu_f}{S}\left(1 - i\frac{1}{S}\frac{\Omega_i}{\omega} + i\frac{\omega}{\Omega_\beta}\frac{\alpha_\mu}{S}(S-1)\right), & \Omega_i \ll \omega \ll \Omega_\beta. \end{cases} \quad (45)$$

The asymptotic expression 45 shows that, in the low-frequency regime, the phase velocity of the slow S-wave depends on the permeability and the squared frequency. In the high-frequency regime, this velocity squared is described by the same equation as the fluid vorticity weighted by the tortuosity of the solid frame (S).
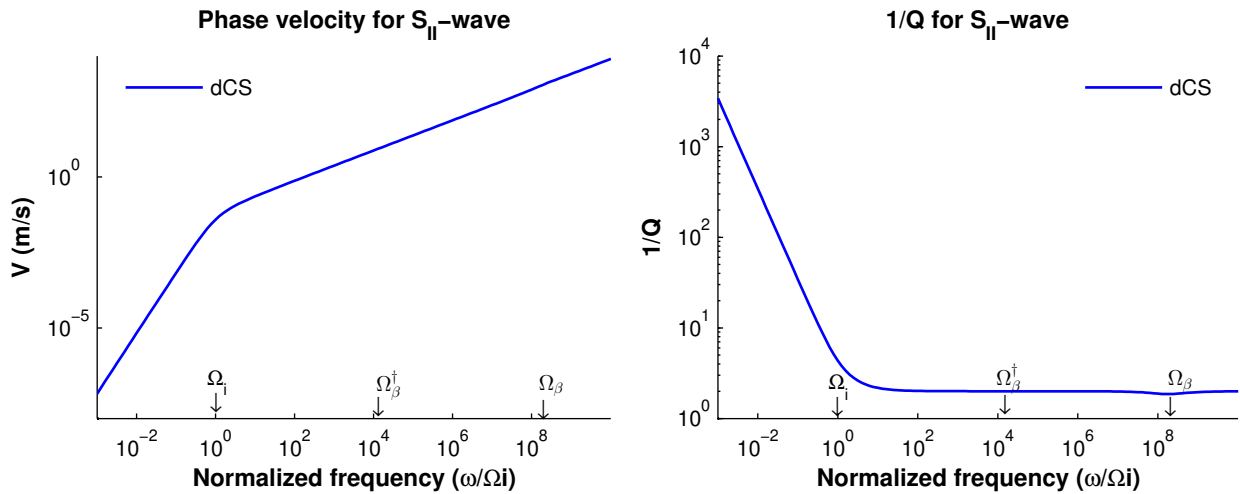
Figure 4. Dispersion relation for the slow S wave. The phase velocity is on the left side, and the inverse quality factor is on the right side.

2.4.3 Fast P-wave

Like the fast S-wave, the phase velocity for the fast P-wave (left panel of figure 5) shows three distinct regimes separated by the Biot critical frequency (Ω_i) and the saturated-frame relaxation frequency for P-waves ($\Omega_\alpha = (K_{ud}^\star + 4\mu/3)/(\xi_f \eta_0 M^\star/K_f + 4\mu_f/3)$). Herein, Ω_α marks the frequency where the intrinsic fluid relaxation relaxes the compression of the porous medium. As in the case of S-waves, above Ω_α the poroelastic framework must be corrected; however, the values for phase velocity and attenuation are computed for completeness.

The inverse quality factor (right panel of figure 5) has two peaks at the critical frequencies. At Ω_i, the attenuation is generated by the fluid relaxation, and, at Ω_α, the peak of inverse quality factor is caused by intrinsic relaxation of the fluid. At the geometric average of Ω_i and Ω_α, $\Omega_\alpha^\dagger$, the intrinsic relaxation of the fluid takes over the Darcy relaxation.

Below Ω_α, the fast P-wave predicted in the Biot theory, red dashed line in figure 5, shows the same phase velocity that in dCS theory. The values of inverse Q are equivalent below $\Omega_\alpha^\dagger$.
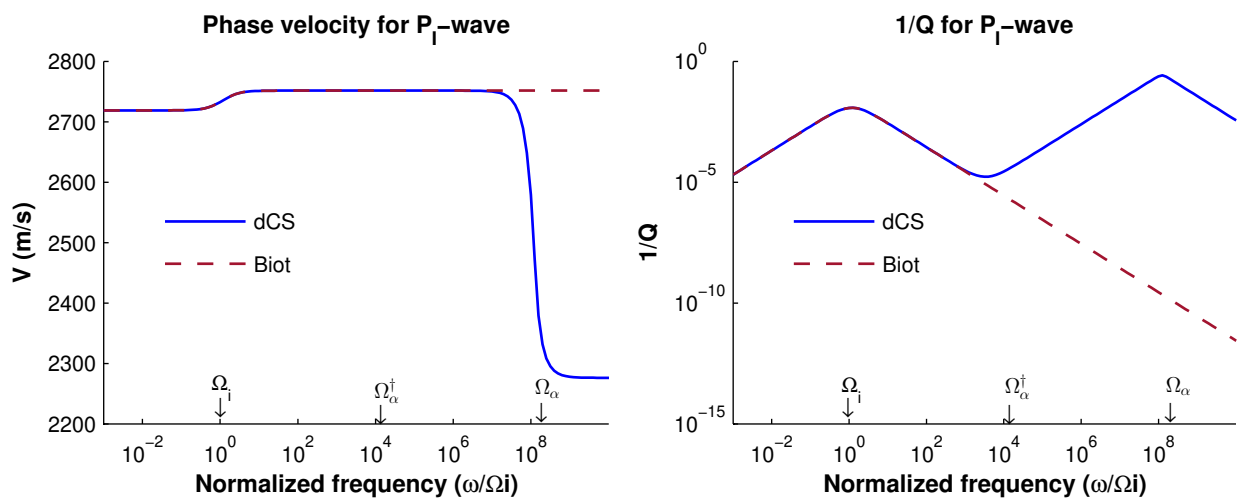
Figure 5. Dispersion relation for the fast P wave. The phase velocity is on the left side, and the inverse quality factor is on the right side.

The approximations for the fast P-wave velocity in the low- and high-frequency regimes are

$$
\alpha_I^2 \approx
\begin{cases}
\alpha_c^{\star 2}\left(1 - i\frac{\omega}{\Omega_b}(m_f + \varepsilon^\star)\right), & \omega \ll \Omega_i. \\[2em]
\alpha_c^{\star 2}\left(\frac{S+\varepsilon^\star}{S-m_f} - \frac{m_s}{S+\varepsilon^\star}\frac{\alpha_0^2}{\alpha_c^{\star 2}}\frac{\alpha_{fl}^2}{\alpha_c^{\star 2}}\right)\Big[1- \\[1em]
i\frac{\Omega_i}{\omega}d_f \frac{m_f+\varepsilon^\star - m_s\frac{\alpha_0^2}{\alpha_c^{\star 2}}\frac{\alpha_{fl}^2}{\alpha_c^{\star 2}}\frac{(S-m_f)^2}{(S+\varepsilon^\star)^2}}{\frac{S+\varepsilon^\star}{S-m_f} - \frac{m_s}{S+\varepsilon^\star}\frac{\alpha_0^2}{\alpha_c^{\star 2}}\frac{\alpha_{fl}^2}{\alpha_c^{\star 2}}} - i\frac{\omega}{\Omega_\alpha^\star}\frac{\eta_0 d_s+(S-1)d_f\Upsilon}{\frac{S+\varepsilon^\star}{S-m_f} - \frac{m_s}{S+\varepsilon^\star}\frac{\alpha_0^2}{\alpha_c^{\star 2}}\frac{\alpha_{fl}^2}{\alpha_c^{\star 2}}} \times \\[1em]
\left(d_f - \frac{m_s}{(S+\varepsilon^\star)^2}\frac{\alpha_0^2}{\alpha_c^{\star 2}}\frac{\alpha_{fl}^2}{\alpha_c^{\star 2}} - \frac{1+(\alpha^\star-\eta_0)(\alpha-\Upsilon)}{\eta_0 d_s+(S-1)d_f\Upsilon}\frac{\eta_0 m_s}{m_f(S+\varepsilon^\star)}\frac{\alpha_0^2}{\alpha_c^{\star 2}}\right)\Big], & \Omega_i \ll \omega \ll \Omega_\alpha.
\end{cases}
\tag{46}
$$

Herein $\alpha_c^{\star 2} = (K_{ud}^\star + 4\mu_0/3)/\rho_m^\circ$ is the generalized Gassmann P-wave velocity squared,

$\alpha_0^2 = (K_0 + 4\mu_0/3)/(\phi_0 \rho_s^\circ)$ is the P-wave velocity squared in the solid frame, and $\alpha_{fl}^{\star 2} = \eta_0 M^\star / \rho_f^\circ$ is the P-wave velocity squared of the fluid inside the porous frame.

The dispersion relation 46 shows that, in the low-frequency regime ($\omega \ll \Omega_i$), the phase velocity of the fast P-wave shows the same value that an effective elastic (Gassmann) medium because of fluid and solid frame constituent parts are coupled. The inverse quality factor increases with frequency since the coupling is not perfect. In the high-frequency regime ($\Omega_i \ll \omega \ll \Omega_\alpha$), the phase velocity shows an increment because the fluid is partially decoupled, as it happens in the fast S-wave. However, the fluid does not support the load in the same amount as in the low-frequency regime, and the increment is smaller than the fast S-wave. The inverse quality factor decrease with frequency until $\Omega_\alpha^\dagger$, after which it increases with frequency to the pick at Ω_α.

2.4.4 Slow P-wave

The dispersion relation for the slow P-wave is shown in figure 6. The phase velocity shows three distinct regimes separated by Ω_i and Ω_α, as the fast P-wave. At the low-frequency regime ($\omega \ll \Omega_i$), the slow P-wave shows the behavior of a diffusive wave, it is, the phase velocity increase with frequency and is attenuated around a half-wavelength ($Q \approx 1/2$). In the high-frequency regime ($\Omega_i \ll \omega \ll \Omega_\alpha$), the slow P-wave is a propagating wave, with a nearly constant phase velocity and an inverse quality factor that decreases with frequency. Above Ω_α, the slow-P wave behaves as a diffusive wave since the intrinsic fluid diffusion is dominant; however, it also needs a correction as in the fast P-wave.

The approximation for the slow P wave dispersion relations in the low- and high-frequency regimes are

$$\alpha_{II}^2 \approx \begin{cases} -i\alpha_{fl}^2 m_s \dfrac{\alpha_0}{\alpha_c^\star} \dfrac{\omega}{\Omega_b}\left(1 + \dfrac{\omega}{\Omega_b}(S + \varepsilon^\star)\right), & \omega \ll \Omega_i. \\[2em] \dfrac{\alpha_{fl}^2}{S + \varepsilon^\star} m_s \dfrac{\alpha_0}{\alpha_c^\star}\Big[1 - i\dfrac{\Omega_i}{\omega}\dfrac{S - m_f}{S + \varepsilon^\star} - \\[1em] i\dfrac{\omega}{\Omega_\alpha^\star}\left((1 + (\alpha^\star - \eta_0)(\alpha - \Upsilon))\dfrac{\eta_0}{m_f}\dfrac{\alpha_c^{\star 2}}{\alpha_{fl}^{\star 2}} - \dfrac{\eta_0 d_s + (S - 1)d_f \Upsilon}{S + \varepsilon^\star}\right)\Big], & \Omega_i \ll \omega \ll \Omega_\alpha. \end{cases}$$ (47)
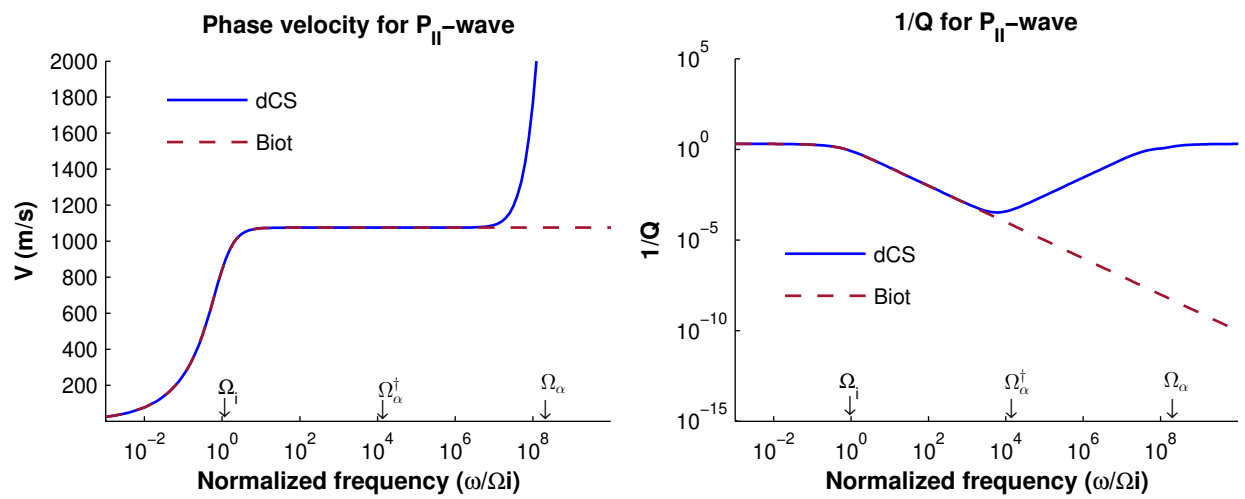
Figure 6. Dispersion relation for the slow P wave. The phase velocity is on the left side, and the inverse quality factor is on the right side.

Chapter 3.   Boundary conditions at discontinuities

Boundary conditions are essential to describe the behavior of waves across discontinuities. They control the way waves are scattered at the interface. The widely used poroelastic boundary conditions are due to Deresiewicz and Skalak (1963). However, because they do not define the behavior of fluid motion tangential to surfaces, these conditions cannot be applied to general cases where such fluid motion occurs. This chapter presents the complete set of boundary conditions for the poroelastic theory. Section 3.1 presents an overview of the boundary conditions given by Deresiewicz and Skalak (1963). Although they define the conditions for different hydraulic contacts, only the permeable (open-pore) and impermeable (closed-pore) limits can be derived from the poroelastic differential equations of motion.

Moreover, in any case, the condition of the fluid motion in the tangential direction is undefined. In section 3.2 the boundary conditions are extended for accounting for that motion. Herein, the case of a solid half-space in welded contact with a porous half-space is used to understand the fluid motion in the tangential direction. Then, the boundary conditions are extended for two porous media at impermeable/permeable contact (section 3.3).

3.1 Boundary conditions in the literature

Deresiewicz and Skalak (1963) give the widely accepted poroelastic boundary conditions. These are developed in the Biot theory from the continuity of the total normal energy flux that, for the u_j^s and w_j fields, is defined as

$$J_\perp = \left(\tau_{jk} \dot{u}_j^s - p^f \delta_{jk} \dot{w}_j \right) \hat{n}_k. \tag{48}$$

The boundary conditions in a permeable interface are defined as the continuity of each term in expression 48. They are

$$\llbracket \dot{u}_\perp^s \rrbracket = 0, \tag{49}$$

$$\llbracket \dot{u}_\parallel^s \rrbracket = 0, \tag{50}$$

$$\llbracket \tau_\perp \rrbracket = 0, \tag{51}$$

$$\llbracket \tau_{\parallel} \rrbracket = 0, \tag{52}$$

$$\llbracket \dot{w}_{\perp} \rrbracket = 0, \tag{53}$$

$$\llbracket p^f \rrbracket = 0. \tag{54}$$

Herein, $\llbracket \ \rrbracket$ represents a jump in its argument. The sub-index $\perp$ and $\parallel$ stand for the normal and tangential directions, respectively. The continuity of $\dot{u}^s_{\perp}$ together with $\dot{w}_{\perp}$ satisfy the mass conservation principle. The continuity of normal and tangential tractions, equations 51 and 52, are on account of Newton's third law. Equation 50 satisfies the no-slip boundary condition for the solid frame of the porous medium. Equation 54 defines the equilibrium of pressure across the interface.

In the opposite limit, the impermeable or closed-pore case, the fluid cannot flow across the interface; thus, the conditions 53 and 54 changes to

$$\dot{w}_{\perp}^{(1)} = \dot{w}_{\perp}^{(2)} = 0. \tag{55}$$

That is, the filtration field in the normal direction vanishes on both sides of the interface.

The boundary conditions of Deresiewicz and Skalak (equations 49-55) are widely used on the reflection-transmission solutions for porous media. However, they do not describe the behavior of the filtration field parallel to the interface ($\dot{w}_{\parallel}$), which accounts for the no-slip condition for the fluid motion. It is because the fluid stress does not account for the viscous forces, causing two redundant degrees of freedom related to the fluid's tangential motion.

3.2   Definition of the boundary condition for tangential fluid motion

In the dCS poroelastic theory, the total normal energy flux is

$$J_{\perp} = \left(\tau_{jk} \dot{u}^s_j + \sigma^f_{jk} \dot{w}_j \right) \hat{n}_k. \tag{56}$$

To fully define the boundary conditions, it is necessary to constrain the term $\llbracket \sigma^f_{\parallel} \dot{w}_{\parallel} \rrbracket = 0$, which accounts for the normal energy flux carried on in the fluid shearing, along with the conditions 49-54.

To understand the tangential motion of the fluid at a discontinuity, let us consider the case of a porous media in welded contact with a solid half-space. The last one acts as a natural impermeable medium that completely disrupts fluid motion. The boundary conditions for this case are

$$\dot{u}^{s}_{\perp} = \dot{u}_{\perp}, \tag{57}$$

$$\dot{u}^{s}_{\parallel} = \dot{u}_{\parallel}, \tag{58}$$

$$\tau_{\perp} = \sigma_{\perp}, \tag{59}$$

$$\tau_{\parallel} = \sigma_{\parallel}, \tag{60}$$

$$\dot{w}_{\perp} = 0. \tag{61}$$

The terms u and σ are the displacements and stresses in the solid medium. The condition 57 stands for the conservation of mass. Equation 58 satisfies the no-slip condition of the solid, and equations 59 and 60 account for the Newton's third law. Equation 61 is the impermeable condition in the Biot theory, and it specifies that the fluid is not able to flow across the interface.

The remaining condition can be satisfied by vanishing either the traction $\sigma^{f}_{\parallel}$ or the filtration field $\dot{w}_{\parallel}$. The choice $\sigma^{f}_{\parallel} = 0$ means that the viscous shear stress of the fluid is vanishing as in a stress-free surface. However, viscous fluids support shear stresses and must be continuous with that of the interface portion in contact, accounting for Newton's third law. Therefore, $\sigma^{f}_{\parallel} = 0$ is not a suitable condition since it violates Newton's third law. On the other hand, choosing $\dot{w}_{\parallel} = 0$ defines a state where the fluid is coupled to the solid frame of porous medium. This condition is feasible since the fluid is always in touch with the solid on an impermeable surface, and viscous fluids in contact with solids obey the no-slip condition. Therefore, as the solid-frame motion is continuous (equation 58), both parts of the porous medium, the fluid and solid frame, move in unison, and it is satisfied vanishing the tangential filtration field in both sides of the interface. It is

$$\dot{w}_{\parallel} = 0. \tag{62}$$

3.3 Extending boundary conditions in a porous-porous contact

For two porous half-spaces in an impermeable contact, the interface can be defined by considering a solid layer of zero thickness between the half-spaces. In such a case, the boundary conditions are defined by the equations 49-52, 55, and

$$\dot{w}_\parallel^{(1)} = \dot{w}_\parallel^{(2)} = 0. \tag{63}$$

For the permeable case, the term $\sigma_\parallel^f \dot{w}_\parallel$ does not vanish. Instead, it is continuous across the interface $\left([\![\sigma_\parallel^f \dot{w}_\parallel]\!] = 0 \right)$. It is satisfied by considering the continuity of each term. It is

$$[\![\dot{w}_\parallel]\!] = 0, \tag{64}$$
$$[\![\sigma_\parallel^f]\!] = 0. \tag{65}$$

The continuity of the $\dot{w}_\parallel$ field accounts for the no-slip condition of the fluid. Whereas the continuity of the $\sigma_\parallel^f$ traction accounts for Newton's third law.

Chapter 4.   Implications of the fluid viscous stress at an impermeable surface

This chapter analyzes the behavior of a porous medium with an impermeable surface by solving the reflection-transmission problem of a horizontally polarized shear (SH) wave normally incident upon a planar contact of a solid and a porous half-space. It enables us to understand the implications of the presence (dCS theory) or absence (Biot theory) of the fluid viscous stress tensor.

Section 4.1 establishes the media configuration for the reflection-transmission problem. Then, in section 4.2 the reflection and transmission coefficients are developed in the Biot theory. They show an unphysical fluid motion at the contact that violates the no-slip condition for the fluid (equation 63). Section 4.3 analyzes if the JKD term solves that shortcoming. However, the unphysical fluid motion at the contact persists. Finally, the analysis in the dCS theory is presented in section 4.4. Herein, the transmission coefficients show that the fluid motion associated with the transmitted slow S-wave counteracts that generated by the transmitted fast S-wave. Therefore, the no-slip condition is fully satisfied.

4.1   Statement of the problem

Let there be an isotropic elastic solid half-space in welded contact with a fluid-saturated porous half-space. The boundary is defined by the plane $z = 0$ (Figure 7). I consider a plane SH-wave in the upper half-space propagating in the positive z-direction. The normally incident SH-wave will generate a reflected SH-wave in the solid half-space. In the porous medium, only one transmitted SH-wave is predicted in the Biot theory, with and without JKD correction, whereas there are two transmitted SH-waves, the fast and slow S-waves, in the dCS theory.

The displacement in the solid half-space (u_y) is governed by the equation of motion of linear elasticity. In the frequency domain, it is represented as the scalar Helmholtz equation

$$\beta^2 \nabla^2 u_y + \omega^2 u_y = 0 \quad \text{for } z \leq 0, \tag{66}$$

and the stress is given by the elastic constitutive equation

$$\sigma_{yz} = \rho\,\beta^2\,\partial_z u_y \quad \text{for } z \leq 0\,. \tag{67}$$

$\beta = \sqrt{\mu/\rho}$ is the S-wave velocity, and ρ and μ are the density and shear modulus of the solid half-space, respectively.
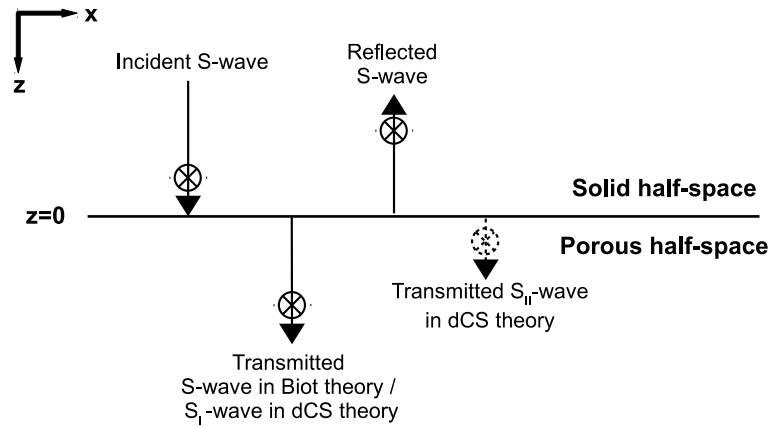
Figure 7. Schematic representation of horizontally polarized incident, reflected and transmitted shear waves at the planar contact of solid and porous half-spaces. Within the Biot theory, there is only one transmitted S-wave. Whereas, in the dCS theory, there are the transmitted fast (S_{I}) and slow (S_{II}) S-waves. The Biot S-wave and the dCS theory S_{I}-wave are equivalent and they are denoted by the same arrow. The dCS theory S_{II}-wave is marked by a dotted arrow.

In the Biot theory, the displacements and corresponding stresses in the porous half-space are given by equations 18 and 23, respectively. In the dCS theory, the motion is described by equation 37, and the stress is given by equation 36.

4.2 Reflection and transmission coefficients in the Biot theory

For the normal incident case, the Helmholtz equation 66 permits the down-going incident ($u_{y_{\mathrm{inc}}}$) and up-going reflected ($u_{y_{\mathrm{r}}}$) plane waves in the upper solid half-space as

$$u_{y_{\mathrm{inc}}} \;=\; e^{i\omega\,q_\beta z}\,, \tag{68}$$

$$u_{y_{\mathrm{r}}} \;=\; r_{S_{\mathrm{Biot}}} e^{-i\omega\,q_\beta z}\,. \tag{69}$$

Here, the amplitude of the incident wave is taken as unity; therefore, the reflected wave amplitude $r_{S_{Biot}}$ is the reflection coefficient. The term q_β is the vertical slowness of S-wave, which for the normal incidence is $q_\beta = 1/\beta$.

In the porous half-space, the transmitted wave permitted by equation 40 is a down-going plane wave that propagates on the solid-frame. The solution reads

$$u^s_{y_t} = t_{S_{Biot}} e^{i\omega\, q_{\beta_{Biot}}\, z} , \tag{70}$$

where, $q_{\beta_{Biot}} = 1/\beta_{Biot}$ is the vertical slowness for the normal incident case.

Substituting equations 68 and 69 into equation 67, and equation 70 into equation 36 for τ_{yz}, the stresses in the upper elastic and lower poroelastic half-spaces are obtained. Thereupon, applying the boundary conditions 58 and 60, the system of equations is

$$\begin{pmatrix} \rho\beta & (\rho_m + \rho_f \gamma_{\beta_{Biot}})\beta_{Biot} \\ -1 & 1 \end{pmatrix} \begin{pmatrix} r_{S_{Biot}} \\ t_{S_{Biot}} \end{pmatrix} = \begin{pmatrix} \rho\beta \\ 1 \end{pmatrix}. \tag{71}$$

It yields to the following solution

$$t_{S_{Biot}} = \frac{2\rho\beta}{\rho\beta + (\rho_m + \rho_f \gamma_{\beta_{Biot}})\beta_{Biot}}. \tag{72}$$

$$r_{S_{Biot}} = t_{S_{Biot}} - 1. \tag{73}$$

Because the shear motion for the filtration field is completely specified by the solid-frame motion, equation 38, the complete poroelastic motion generated by the transmitted wave is

$$\mathbf{u}_{y_t} = \begin{pmatrix} u^s_y \\ w_y \end{pmatrix} = t_{S_{Biot}} \begin{pmatrix} 1 \\ \gamma_{Biot} \end{pmatrix} e^{i\omega\, q_{\beta_{Biot}}\, z}, \tag{74}$$

which means that the no-slip condition for the filtration field, equation 62, is never satisfied, since neither $t_{S_{Biot}}$ nor $\gamma_{\beta_{Biot}}$ can be vanishing. Choosing the vanishing transmission coefficient $t_{S_{Biot}}$ would amount to an unphysical state because it will result in total reflection whatsoever the contrast in impedance is. Furthermore, $\gamma_{\beta_{Biot}}$ is also non-vanishing, as its explicit expression, in terms of material properties and frequency, worked out below in equation 75 shows.

4.2.1 Non-vanishing filtration field at the interface

In the following, I derive the explicit expression of $|t_{S_{Biot}} \gamma_{\beta_{Biot}}|$, the amplitude of non-vanishing filtration field at the interface.

The ratio $\gamma_{\beta_{Biot}}$ and the velocity β_{Biot} are frequency-dependent and, in turn, they make the transmission coefficient $t_{S_{Biot}}$ frequency-dependent. This dependence has two distinct regimes, separated by the transition frequency Ω_i.

By performing a series expansion in terms of frequency and retaining only the leading-order terms in equation 39, the asymptotic expressions of $\gamma_{\beta_{Biot}}$ in the low- and high-frequency regimes are

$$\gamma_{\beta_{Biot}} \approx -\frac{\eta_0}{S} \times \begin{cases} \dfrac{\omega^2}{\Omega_b^2/S^2} - i\dfrac{\omega}{\Omega_b/S}, & \omega \ll \Omega_i \\[3mm] \\ 1 - i\dfrac{\Omega_b/S}{\omega} & \Omega_i \ll \omega \end{cases} . \tag{75}$$

Using the preceding equation and the approximation for β_{Biot} into equation 72, the asymptotic form of transmission coefficient $t_{S_{Biot}}$ is

$$t_{S_{Biot}} \approx \begin{cases} \underbrace{\dfrac{2Z_\beta}{Z_\beta + Z_{\beta_c}}}_{A_{t_{Biot}}^{s_{lo}}} \left[1 - i\dfrac{\omega}{\Omega_b}\dfrac{m_f}{2}\dfrac{Z_{\beta_c}}{Z_\beta + Z_{\beta_c}} \right], & \omega \ll \Omega_i \\[6mm] \\ \underbrace{\dfrac{2Z_\beta}{Z_\beta + Z'_{\beta_c}}}_{A_{t_{Biot}}^{s_{hi}}} \left[1 - i\dfrac{\Omega_i}{\omega}\dfrac{1}{S}\dfrac{m_f}{2}\dfrac{Z'_{\beta_c}}{Z_\beta + Z'_{\beta_c}} \right], & \Omega_i \ll \omega \end{cases} . \tag{76}$$

Herein, $Z_\beta = \rho\beta$ is the S-wave impedance in the solid half-space. $Z_{\beta_c} = \rho_m\beta_c$ and $Z'_{\beta_c} = (\sqrt{1 - m_f/S})\rho_m\beta_c$ are the effective S-wave impedances in the porous half-space in the low- and high-frequency regimes, respectively. In equation 76, the magnitude of the complex numbers within square-brackets is approximately unity since each lumped material parameter is arranged to be less than unity, and the leading scaled frequency term is much smaller than unity. Therefore, the modulus of the coefficient is essentially the term marked by the underbrace. Thus, $A_{t_{Biot}}^{s_{lo}}$ and $A_{t_{Biot}}^{s_{hi}}$ are, respectively, read off

as the amplitudes of the solid-frame displacement field generated by the transmitted wave at the low- and high-frequency regimes.

The transmitted wave generates a filtration displacement field at the contact as per equation 74. The amplitude of this motion, $|t_{S_{Biot}} \gamma_{\beta_{Biot}}| \equiv A^w_{t_{Biot}}$, is approximated as

$$
A^w_{t_{Biot}} \approx
\begin{cases}
\underbrace{-\eta_0 \dfrac{\omega}{\Omega_b} \dfrac{2Z_\beta}{Z_\beta + Z_{\beta_c}}}_{A^{w^{lo}}_{t_{Biot}}}, & \omega \ll \Omega_i \\[2em]
\underbrace{-\dfrac{\eta_0}{S} \dfrac{2Z_\beta}{Z_\beta + Z'_{\beta_c}}}_{A^{w^{hi}}_{t_{Biot}}}. & \Omega_i \ll \omega
\end{cases}
\tag{77}
$$

Equation 77 shows that in the sub-Biot critical frequency (Ω_i) regime, the filtration displacement field is not significant because of the scaled frequency term. However, as the frequency approaches Ω_i, the filtration displacement field increase and makes a transition to its asymptotic value for the high-frequency regime, which is given by the amplitude of the solid-frame displacement ($A^{s^{hi}}_{t_{Biot}}$) weighted by the factor $-\eta_0/S$. This means that the no-slip condition of the fluid at the contact (equation 62) could be satisfied only if porosity is vanishing ($\eta_0 = 0$) or tortuosity is infinite ($S \to \infty$), which are unphysical extremities for a porous medium. Therefore, it is observed that this condition is not satisfied for any fluid-saturated porous medium. This is expected because equation 62 was not part of the BVP statement, and this analysis demonstrates that this no-slip condition is not "automatically" or "implicitly" accounted for.

4.2.2 Numerical example of solid-frame and filtration displacement fields at the contact

To numerically illustrate the robustness of the above asymptotic expressions, they are compared against the exact amplitude of the solid-frame and filtration fields computed based on equation 72. The physical properties of the porous half-space are as reported by Bouzidi and Schmitt (2012). The shear modulus and density of the solid half-space are taken such that the wave is completely transmitted in the low-frequency

limit.

Figure 8 shows the solid-frame and filtration amplitudes generated by the transmitted wave. The amplitudes are normalized by the amplitude in the solid half-space generated by the incident wave. Herein, the asymptotes $A^s_{t_{Biot}}$ and $A^w_{t_{Biot}}$, which are presented by the dotted lines, are in good agreement with the corresponding exact solutions. Below the critical frequency Ω_i, the solid-frame displacement (left panel of Figure 8) is unity indicating perfect transmission. This is because the S-wave impedance of both media is the same. Above Ω_i, the solid and the fluid are not any longer perfectly coupled. Therefore, the effective density is reduced in the porous medium, which in turn reduces its effective impedance. This increases the amplitude of the solid-frame motion.

The amplitude of the filtration displacement (right panel of Figure 8) is negligibly small in the low-frequency regime. However, as the frequency approaches to Ω_i, the amplitude increases and makes a transition to its maximum value in the high-frequency regime. In the high-frequency regime, the partial fluid-solid coupling generates a filtration displacement that is negative η_0/S fraction (-0.27) of the amplitude of the solid-frame motion. This prediction is unphysical in the sense that the filtration field is expected to vanish at the contact (equation 62).
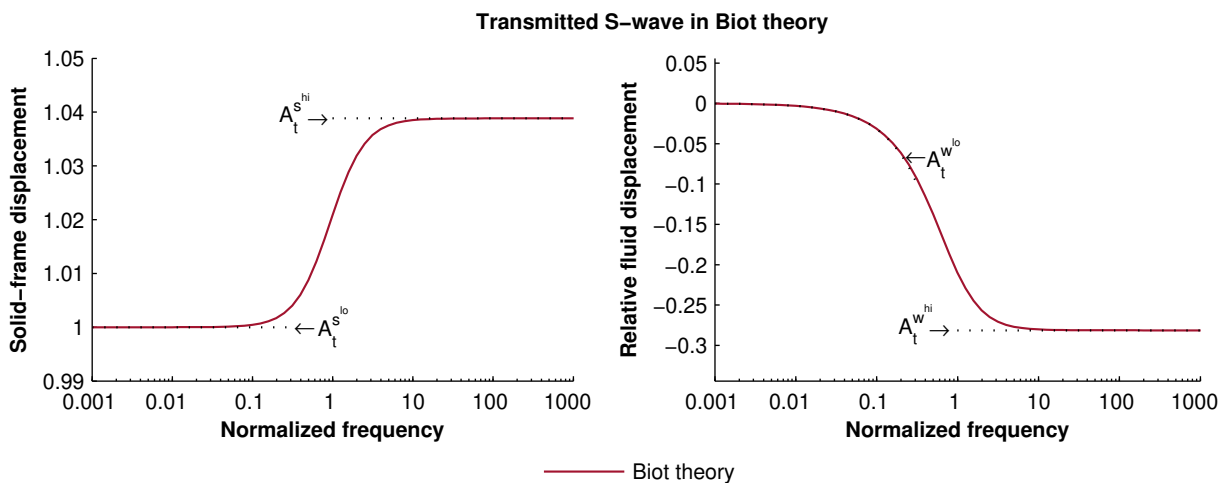
Figure 8. Displacement fields related to the transmitted wave in the Biot theory. The solid-frame field is in the left panel and the filtration field is in the right panel. The shear modulus and density in the solid half-space are 3.6 GPa and 1881 kg/m^3, respectively. The porous half-space properties are in Table 1 of Appendix A. The frequency is normalized by the Biot critical frequency Ω_i, which for this data set is 2530 Hz. The displacements are normalized by the amplitude of the motion in the solid half-space generated by the incident wave. The asymptotes for the solid-frame and filtration displacement fields are presented by the dotted-lines.

4.3 Reflection and transmission coefficients in the Biot theory with the dynamic permeability

This section analyzes whether the dynamic permeability correction is able to eliminate the relative fluid motion at the discontinuity and thereby rendering a physical meaningful solution to the reflection-transmission problem.

In the Biot theory with the JKD term, the filtration field is yet entirely specified by the solid-frame field as equation 38, except the ratio $\gamma_{\beta_{Biot}}$ therein transforms to

$$\gamma_{\beta_{JKD}} = -\frac{\frac{\eta_0}{S}}{1 + i\frac{\Omega_b}{\omega}\frac{1}{S}\left(1 - 4i\frac{\omega}{\Omega_b}\frac{\kappa S^2}{\eta_0 \Lambda^2}\right)^{1/2}}, \tag{78}$$

and the form of governing equation of shear motion still remains as equation 40, with the S-wave velocity term β_{Biot} therein changed to

$$\beta_{JKD} = \sqrt{\frac{\mu_0}{\rho_m + \rho_f \gamma_{\beta_{JKD}}}}. \tag{79}$$

Therefore, the transmission coefficient keeps the same form as equation 72. It reads

$$t_{S_{JKD}} = \frac{2\rho\beta}{\rho\beta + (\rho_m + \rho_f \gamma_{\beta_{JKD}})\beta_{JKD}}. \tag{80}$$

In regime $\omega \ll \Omega_i$, the ratio $\gamma_{\beta_{JKD}}$ and β_{JKD} velocity become $\gamma_{\beta_{Biot}}$ and β_{Biot}, respectively. Therefore, the transmission coefficient $t_{S_{JKD}}$ is essentially equal to $t_{S_{Biot}}$ in the low-frequency regime.

The asymptotes in the high-frequency regime for $\gamma_{\beta_{JKD}}$ and β_{JKD} are

$$\gamma_{\beta_{JKD}} \approx -\frac{1}{1 + \frac{\sqrt{2\nu_f/\omega}}{\Lambda}}\frac{\eta_0}{S}\left(1 - i\frac{\frac{\sqrt{2\nu_f/\omega}}{\Lambda}}{1 + \frac{\sqrt{2\nu_f/\omega}}{\Lambda}}\right), \quad \Omega_i \ll \omega, \tag{81}$$

and

$$\beta_{JKD} \approx \left(1 - \frac{\frac{m_f}{S}}{1 + \frac{\sqrt{2\nu_f/\omega}}{\Lambda}}\right)^{-1/2}\beta_c\left(1 - i\frac{1}{2}\frac{\frac{m_f}{S}\frac{\sqrt{2\nu_f/\omega}}{\Lambda}}{\left(1 - \frac{m_f}{S} + \frac{\sqrt{2\nu_f/\omega}}{\Lambda}\right)\left(1 + \frac{\sqrt{2\nu_f/\omega}}{\Lambda}\right)}\right), \quad \Omega_i \ll \omega. \tag{82}$$

By substituting these approximations into equation 80, the transmission coefficient, in the high-frequency regime, is given by

$$t_{\text{JKD}}^{\text{hi}} \approx \underbrace{\frac{2Z_\beta}{Z_\beta + Z_{\beta_c}^{\text{JKD}}}}_{A_{t_{\text{JKD}}}^{s^{\text{hi}}}} \left(1 - i\frac{1}{2} \frac{Z_{\beta_c}^{\text{JKD}}}{Z_\beta + Z_{\beta_c}^{\text{JKD}}} \frac{\frac{m_f}{S} \frac{\sqrt{2\,\nu_f/\omega}}{\Lambda}}{\left(1 - \frac{m_f}{S} + \frac{\sqrt{2\,\nu_f/\omega}}{\Lambda} \right) \left(1 + \frac{\sqrt{2\,\nu_f/\omega}}{\Lambda} \right)} \right), \tag{83}$$

where $Z_{\beta_c}^{\text{JKD}} = \rho_m \beta_c \sqrt{1 - m_f/S(1 + \sqrt{2\,\nu_f/\omega}/\Lambda)}$ is the effective S-wave impedance in the high-frequency regime. $A_{t_{\text{JKD}}}^{s^{\text{hi}}}$ is the amplitude of the solid-frame field generated by the transmitted wave in the high-frequency regime. The inclusion of the JKD term makes the transition of the amplitude to the high-frequency regime smoother because of the $\omega^{1/2}$ term. Finally, the amplitude of the filtration field generated by the transmitted wave becomes

$$A_{t_{\text{JKD}}}^{w^{\text{hi}}} \approx -\frac{\frac{\eta_0}{S}}{1 + \frac{\sqrt{2\,\nu_f/\omega}}{\Lambda}} \frac{2Z_\beta}{Z_\beta + Z_{\beta_c}^{\text{JKD}}}. \tag{84}$$

It is observed that this amplitude is not vanishing. Instead, the amplitude increases with frequency. Note that as frequency increases, the ratio wavelength of fluid vorticity to pore-throat diameter $\sqrt{2\,\nu_f/\omega}/\Lambda$ becomes insignificant, the transmission coefficient in equation 83 asymptotically approach to that of the Biot theory (second line of equation 76). Likewise, the filtration field in equation 84 tends to that of the Biot theory, equation 77.

To illustrate the robustness of the asymptotic expressions in this case, they are compared against the exact displacements fields computed using equation 80. The properties of both half-spaces are the same as those in Figure 8. Figure 9 shows the normalized displacements for the solid-frame and filtration displacement fields generated by the transmitted SH-wave. The asymptotes $A_{t_{\text{JKD}}}^{s^{\text{hi}}}$ and $A_{t_{\text{JKD}}}^{w^{\text{hi}}}$ are in good agreement with the corresponding exact solutions. By comparing with the solution of the Biot theory, the solid-frame displacement shows the same values in the low-frequency regime. In the high-frequency regime, there is now a smoother transition to the maximum value. Most importantly, the filtration field at the contact persists even with the dynamic permeability correction factor. The displacement has the same value in the high-frequency limit as in the Biot theory prediction. This means that the no-slip

boundary condition of the fluid is not satisfied.
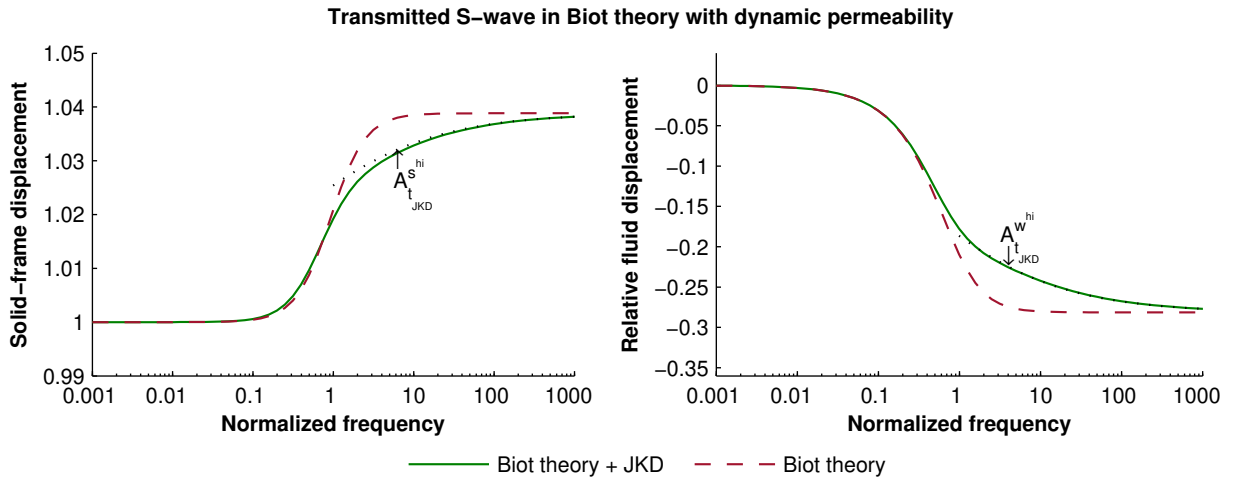
Figure 9. Displacement fields related to the transmitted wave in the Biot theory including the dynamic permeability term. The solid-frame field is in the left panel and the filtration field is in the right panel. The asymptotes for the solid-frame and filtration displacement fields are presented by the dotted-lines. The frequency is normalized by Ω_i. The displacements are normalized by the amplitude of the motion in the solid half-space generated by the incident wave. The properties of the half-spaces are the same as in Figure 8.

4.4 Reflection and transmission coefficients in the dCS theory

For the normal incident case, the permitted waves in the solid are given by equations 68 and 69. In the porous half-space, the transmitted waves permitted by the system of Helmholtz equations 18 are two down-going plane waves (equation 22). In terms of solid-frame and filtration displacements, the solution reads

$$\mathbf{u}_{y_t} = \begin{pmatrix} u_y^s \\ w_y \end{pmatrix} = t_{S_I} \begin{pmatrix} 1 \\ \gamma_{\beta_I} \end{pmatrix} e^{i\omega\, q_{\beta_I}\, z} + t_{S_{II}} \begin{pmatrix} \gamma_{\beta_{II}} \\ 1 \end{pmatrix} e^{i\omega\, q_{\beta_{II}}\, z} . \tag{85}$$

Herein, $q_{\beta_I} = 1/\beta_I$ and $q_{\beta_{II}} = 1/\beta_{II}$ are the respective vertical slowness for the normal incident case. The terms t_{S_I} and $t_{S_{II}}$ are the transmission coefficients of the state vector corresponding to fast and slow S-waves, respectively. Thus, t_{S_I} and $t_{S_I}\gamma_{\beta_I}$ are read off as the amplitudes of solid-frame and filtration fields, respectively, associated with the transmitted fast S-wave. Likewise, $t_{S_{II}}\gamma_{\beta_{II}}$ and $t_{S_{II}}$ are read off as the amplitudes of solid-frame and filtration fields, respectively, associated with the transmitted slow S-wave.

By substituting the displacements given in equations 68 and 69 into the expression

67 and the displacements of equation 85 into the expression 2, the stresses are obtained. Thereupon, applying the boundary conditions, equations 58, 60 and 62, the system of equations is

$$
\begin{pmatrix}
\rho\beta & (1+\frac{m_f}{\eta_0}\gamma_{\beta_I})\rho_m\beta_I & (\gamma_{\beta_{II}}+\frac{m_f}{\eta_0})\rho_m\beta_{II} \\
-1 & 1 & \gamma_{\beta_{II}} \\
0 & \gamma_{\beta_I} & 1
\end{pmatrix}
\begin{pmatrix}
r_S \\
t_{S_I} \\
t_{S_{II}}
\end{pmatrix}
=
\begin{pmatrix}
\rho\beta \\
1 \\
0
\end{pmatrix}.
\tag{86}
$$

It yields the following solution for the reflection and transmission coefficients for displacement fields

$$
t_{S_I} = \frac{2\rho\beta}{\rho\beta\left(1-\gamma_I\gamma_{II}\right)+\rho_m\beta_I+\gamma_I\rho_f\left(\beta_I-\beta_{II}\right)-\gamma_I\gamma_{II}\rho_m\beta_{II}}
\tag{87}
$$

$$
t_{S_{II}} = -\gamma_{\beta_I}t_{S_I}
\tag{88}
$$

$$
r_S = \left(1-\gamma_{\beta_I}\gamma_{\beta_{II}}\right)t_{S_I}-1.
\tag{89}
$$

From the second line of equation 85 it is apparent that for vanishing filtration field at the contact $z = 0$, the required condition is $t_{S_I}\gamma_{\beta_I} + t_{S_{II}} = 0$, which is precisely equation 88. Hence, the no-slip condition is satisfied.

By setting shear viscosity vanishing in $\boldsymbol{\nu}$ matrix, the dCS theory reduces to the standard Biot theory. In this case $\gamma_{\beta_I} = \gamma_{\beta_{Biot}}$, $\beta_I = \beta_{Biot}$, and, $\gamma_{\beta_{II}}$ and β_{II} go to zero; thus, the coefficients in equations 87 and 89 reduce to those in equations 72 and 73, respectively. The coefficient $t_{S_{II}}$ is meaningless, since, in this limit, the slow S-wave does not exist; hence, equation 88 is redundant.

For completeness, in the following I develop the asymptotic forms of the transmission coefficients t_{S_I} and $t_{S_{II}}$ and their associated filtration field. It allows us to determine the parameters controlling the filtration field at the contact and gives a comparison with the approximation in the Biot theory, equation 77.

By substituting the asymptotes 44 and 45 for shear velocities, and the elements of the $\boldsymbol{\beta}$ matrix on γ_{β_I} and $\gamma_{\beta_{II}}$, and retaining only the leading-order terms of their real and imaginary part, they are approximated for the low- and high-frequency regimes as

$$
\gamma_{\beta_{\mathrm{I}}} \approx
\begin{cases}
-\dfrac{\omega}{\Omega_{\mathrm{b}}}\eta_0\!\left(S\dfrac{\omega}{\Omega_{\mathrm{b}}}-i\right), & \omega \ll \Omega_{\mathrm{i}} \\[2em]
-\dfrac{\eta_0}{S}\left(1-i\left(\dfrac{1}{S}\dfrac{\Omega_{\mathrm{b}}}{\omega}-\alpha_\mu\dfrac{\omega}{\Omega_\beta}\dfrac{1-\frac{m_{\mathrm{f}}}{S}}{m_{\mathrm{f}}}\right)\right), & \Omega_{\mathrm{i}} \ll \omega \ll \Omega_\beta.
\end{cases}
\tag{90}
$$

$$
\gamma_{\beta_{\mathrm{II}}} \approx -\dfrac{\omega}{\Omega_\beta}\dfrac{m_{\mathrm{s}}}{m_{\mathrm{f}}}\left(\dfrac{\omega}{\Omega_\beta}\dfrac{m_{\mathrm{s}}}{m_{\mathrm{f}}}\alpha_\mu+i\right) \qquad \omega \ll \Omega_\beta .
\tag{91}
$$

Applying the approximations for velocities and eigenvectors in the exact expressions 87 and 88 of transmission coefficients, and retaining only the leading-order terms, I find

$$
t_{S_{\mathrm{I}}} \approx
\begin{cases}
\underbrace{\dfrac{2Z_\beta}{Z_\beta+Z_{\beta_{\mathrm{c}}}}}_{A_{t_{\mathrm{I}}}^{s^{\mathrm{lo}}}}\left[1-i\dfrac{\omega}{\Omega_{\mathrm{b}}}\dfrac{m_{\mathrm{f}}}{2}\dfrac{Z_{\beta_{\mathrm{c}}}}{Z_\beta+Z_{\beta_{\mathrm{c}}}}\right], & \omega \ll \Omega_{\mathrm{i}} \\[2em]
\underbrace{\dfrac{2Z_\beta}{Z_\beta+Z'_{\beta_{\mathrm{c}}}}}_{A_{t_{\mathrm{I}}}^{s^{\mathrm{hi}}}}\left[1-i\dfrac{1}{2}\dfrac{\Omega_{\mathrm{i}}}{\omega}\dfrac{m_{\mathrm{f}}}{S}\dfrac{Z'_{\beta_{\mathrm{c}}}}{Z_\beta+Z'_{\beta_{\mathrm{c}}}}+\underline{i\dfrac{1}{2}\dfrac{\omega}{\Omega_\beta}\dfrac{1}{S}\left(\alpha_\mu\dfrac{(S+1)Z'_{\beta_{\mathrm{c}}}}{Z_\beta+Z'_{\beta_{\mathrm{c}}}}+\eta_0\dfrac{m_{\mathrm{s}}}{m_{\mathrm{f}}}\dfrac{Z'_{\beta_{\mathrm{c}}}-2Z_\beta}{Z_\beta+Z'_{\beta_{\mathrm{c}}}}\right)}\right], & \Omega_{\mathrm{i}} \ll \omega \ll \Omega_\beta.
\end{cases}
\tag{92}
$$

The approximation 92 in the low-frequency regime corresponds to the expression 76 in the Biot theory. In the high-frequency regime, the amplitudes of the transmission S-wave in Biot and S_{I}-wave in dCS theory are equivalent. However, the imaginary term of the wave has an additional element, the underlined term, in the dCS case. This term is negligible at frequencies below $\Omega_\beta^\dagger$. Therefore, for $\omega < \Omega_\beta^\dagger$ the amplitude in both theories is the same.

In the dCS theory, the additional transmitted S_{II}-wave has the amplitude

$$t_{S_{\mathrm{II}}} \approx \begin{cases} \underbrace{\eta_0 \dfrac{\omega}{\Omega_b} \dfrac{2Z_\beta}{Z_\beta + Z_{\beta_c}}}_{A_{t_{\mathrm{II}}}^{w^{lo}}} \left[\dfrac{\omega}{\Omega_b}\left(S - \dfrac{m_f}{2}\dfrac{Z_{\beta_c}}{Z_\beta+Z_{\beta_c}}\right) - i \right], & \omega \ll \Omega_i. \\[3em] \underbrace{\eta_0 \dfrac{2Z_\beta}{S\ Z_\beta + Z'_{\beta_c}}}_{A_{t_{\mathrm{II}}}^{w^{hi}}} \left[1 - i\dfrac{1}{S}\dfrac{\Omega_i}{\omega}\left(S - m_f + \dfrac{m_f}{2}\dfrac{Z'_{\beta_c}}{Z_\beta+Z'_{\beta_c}}\right) \right. \\[2em] \left. + i\dfrac{1}{2}\dfrac{1}{S}\dfrac{\omega}{\Omega_\beta}\left(2\alpha_\mu \dfrac{S-m_f}{m_f} + \alpha_\mu \dfrac{(1+S)Z'_{\beta_c}}{Z_\beta+Z'_{\beta_c}} + \eta_0 \dfrac{m_s}{m_f}\dfrac{Z'_{\beta_c}-2Z_\beta}{Z_\beta+Z'_{\beta_c}}\right)\right], & \Omega_i \ll \omega \ll \Omega_\beta. \end{cases} \tag{93}$$

The transmitted fast S-wave generates a filtration displacement field at the contact per equation 85. The amplitude of this motion, $|t_{S_{\mathrm{I}}}\gamma_{\beta_{\mathrm{I}}}| = A_{t_{\mathrm{I}}}^w$, is approximated as

$$A_{t_{\mathrm{I}}}^w \approx \begin{cases} \underbrace{-\eta_0 \dfrac{\omega}{\Omega_b}\dfrac{2Z_\beta}{Z_\beta + Z_{\beta_c}}}_{A_{t_{\mathrm{I}}}^{w^{lo}}}, & \omega \ll \Omega_i. \\[3em] \underbrace{-\dfrac{\eta_0}{S}\dfrac{2Z_\beta}{Z_\beta + Z'_{\beta_c}}}_{A_{t_{\mathrm{I}}}^{w^{hi}}}, & \Omega_i \ll \omega \ll \Omega_\beta. \end{cases} \tag{94}$$

The terms $A_{t_{\mathrm{I}}}^{w^{lo}}$ and $A_{t_{\mathrm{I}}}^{w^{hi}}$ are the amplitudes of the filtration field associated to the fast S-wave in the low- and high-frequency regime, respectively. This amplitude is the same as that predicted in the Biot theory, in equation 77.

Likewise, per equation 85, the transmitted slow S-wave generates a filtration displacement field at the contact. Its amplitude, $|t_{S_{\mathrm{II}}}| = A_{t_{\mathrm{II}}}^w$, is approximated as

$$A_{t_{\mathrm{II}}}^w \approx \begin{cases} \underbrace{\eta_0 \dfrac{\omega}{\Omega_b}\dfrac{2Z_\beta}{Z_\beta + Z_{\beta_c}}}_{A_{t_{\mathrm{II}}}^{w^{lo}}}, & \omega \ll \Omega_i. \\[3em] \underbrace{\dfrac{\eta_0}{S}\dfrac{2Z_\beta}{Z_\beta + Z'_{\beta_c}}}_{A_{t_{\mathrm{II}}}^{w^{hi}}}, & \Omega_i \ll \omega \ll \Omega_\beta. \end{cases} \tag{95}$$

The terms $A_{t_{\mathrm{II}}}^{w^{lo}}$ and $A_{t_{\mathrm{II}}}^{w^{hi}}$ are, respectively, the amplitude of the filtration field generated by the transmitted S_{II}-wave in the low- and high-frequency regime. These amplitudes in equation 95 are equal and opposite to that generated by the S_{I}-wave, equation 94. Therefore, as both processes, the fast and slow S-waves, are generated, the net motion of the fluid at the contact is vanishing for the entire range of frequencies. This means that the no-slip condition for the fluid (equation 62) is satisfied. This is expected since in the dCS theory this boundary condition is part of the BVP, thereby ensuring that no field components are unconstrained.

4.4.1 Numerical example of solid-frame and filtration displacement fields at the contact

To numerically illustrate the motion generated at the contact, the amplitude of the solid-frame and filtration displacement fields generated by the transmission coefficients in equations 87 and 88 are computed. Herein, the properties of the solid an porous half-space are the same than in the Biot case, Figure 8. Figure 10 shows that the normalized amplitude of the solid-frame and filtration displacements have the same values as in the Biot theory. However, the generation of the S_{II}-wave at the contact generates a filtration displacement with the same magnitude and opposite sign. This is true for all frequencies, but its magnitude in the low-frequency regime is exponentially small. The S_{II}-wave also generates a negligibly small motion of the solid frame.

Transmitted fast S–wave in dCS theory

Transmitted slow S–wave in dCS theory

dCS theory — — — Biot theory
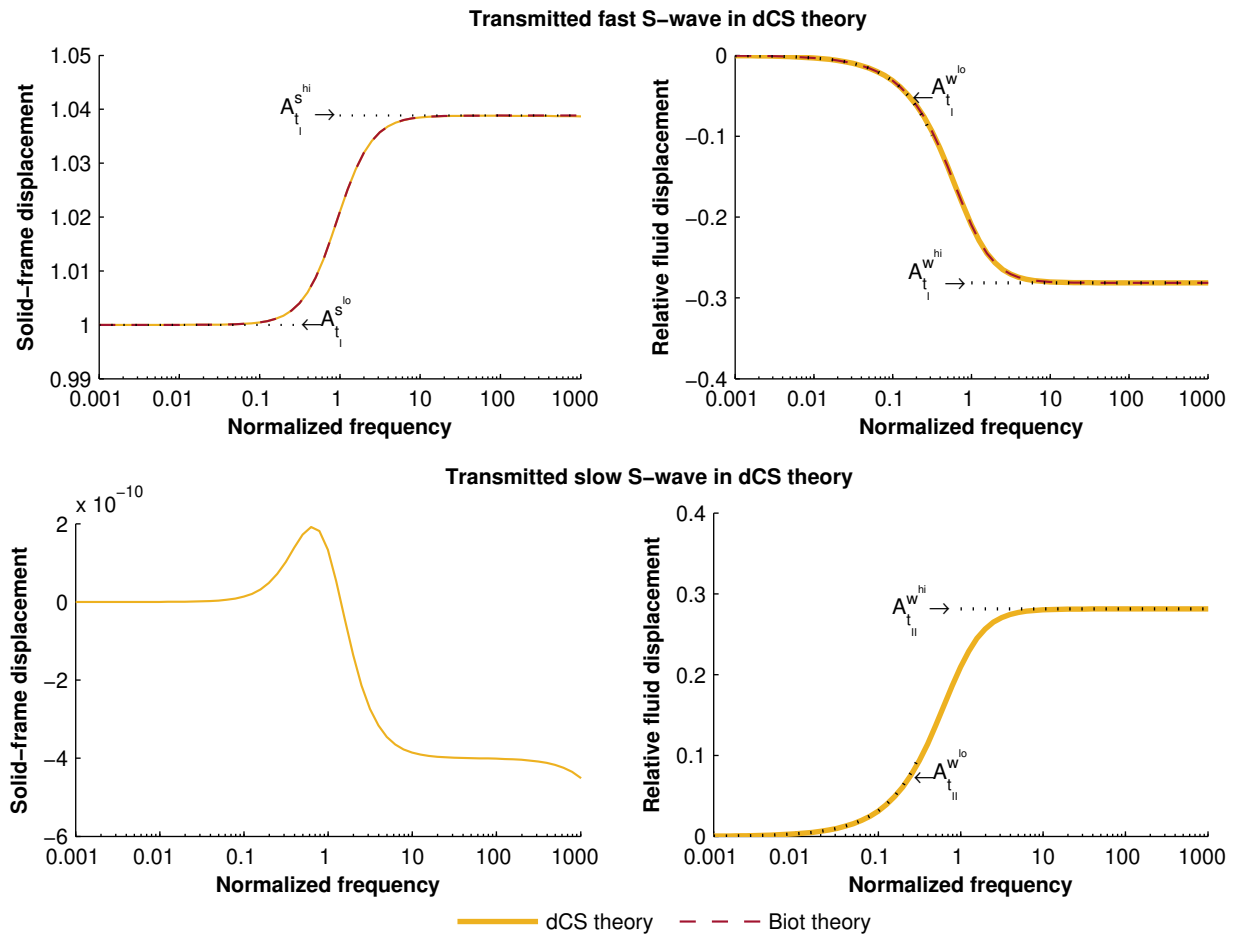
Figure 10. Displacement fields related to the transmitted wave in the dCS theory. The asymptotes for the solid-frame and filtration displacement field are presented by the black dotted-line. The frequency is normalized by the Biot critical frequency Ω_i. The displacements are normalized by the amplitude of the motion in the solid half-space generated by the incident wave. The properties of both half-spaces are the same as in Figure 8.

Chapter 5. Conversion scattering at a porous-porous plane interface

This chapter analyzes the role of the fluid viscous stress tensor in a single planar contact from the solution of the reflection-transmission problem. For that, I consider two poroelastic half-spaces in welded contact. The properties of these media are given in Appendix A. Both permeable and impermeable cases are considered. The reflection and transmission coefficients are computed for the displacement amplitudes (A_d) that are related to the potential amplitudes (A_p) by

$$A_d = V A_p, \tag{96}$$

where $V = \alpha_I,\ \alpha_{II},\ \beta_I,\ \beta_{II}$ stands for the velocity of the wave analyzed.

To analyze the effects of the fluid viscous stress tensor, I compare the solutions of the dCS theory with those obtained in the Biot theory using the relative difference of the magnitude of the coefficients in each approach. It is defined as

$$\text{Relative difference} = \frac{|A_{d_{Biot}}| - |A_{d_{dCS}}|}{|A_{d_{Biot}}|}, \tag{97}$$

The $|\cdot|$ means the magnitude of the coefficient, which is a complex number. Then, the positive values indicate that the amplitude predicted in the dCS theory is smaller than that in the Biot theory. In contrast, negative values account for larger amplitude in the dCS theory than in the Biot theory.

Section 5.1 introduces a geometric representation of slownesses in the poroelastic theory. Then, section 5.2 analyzes the scattered amplitudes for SH-waves incident in the contact of two porous media. The reflection and transmission coefficients for an incident fast SH-wave are analytically developed herein. After that, the amplitude of scattered waves from incident P- and SV-waves are numerically analyzed in section 5.3.

5.1 Geometric ray representation

In the geometrical representation of waves, the rays describe the wave propagation direction. In this case, the slowness can be defined in terms of the ray angle (θ), the angle between the ray and the z-axis. According to Snell's law, horizontal slowness is defined as

$$p = \frac{\sin(\theta_{P_I})}{\alpha_I} = \frac{\sin(\theta_{P_{II}})}{\alpha_{II}} = \frac{\sin(\theta_{S_I})}{\beta_I} = \frac{\sin(\theta_{S_{II}})}{\beta_{II}}, \tag{98}$$

where θ_{P_I}, $\theta_{P_{II}}$, θ_{S_I}, and $\theta_{S_{II}}$ are the angle of propagation for the fast P-, slow P-, fast S-, and slow S-waves, respectively. Then, the vertical slownesses are

$$q_{\alpha_I} = \frac{\cos(\theta_{P_I})}{\alpha_I}, \quad q_{\alpha_{II}} = \frac{\cos(\theta_{P_{II}})}{\alpha_{II}}, \quad q_{\beta_I} = \frac{\cos(\theta_{S_I})}{\beta_I}, \quad q_{\beta_{II}} = \frac{\cos(\theta_{S_{II}})}{\beta_{II}}. \tag{99}$$

Using the geometric representations of slownesses, the following terms related to the stresses (equations 34 and 35) are

$$2p\boldsymbol{\rho}\boldsymbol{\Omega}\mathbf{R}_\beta\boldsymbol{\Lambda}_\beta\mathbf{Q}_\beta = \begin{pmatrix} Z_{\tau S_I}\frac{\sin(2\theta_{S_I})}{\beta_I} & Z_{\tau S_{II}}\frac{\sin(2\theta_{S_{II}})}{\beta_{II}} \\ Z_{\sigma^f S_I}\frac{\sin(2\theta_{S_I})}{\beta_I} & Z_{\sigma^f S_{II}}\frac{\sin(2\theta_{S_{II}})}{\beta_{II}} \end{pmatrix}, \tag{100}$$

$$\boldsymbol{\rho}\boldsymbol{\Omega}\mathbf{R}_\beta\left(\mathbf{I} - 2p^2\boldsymbol{\Lambda}_\beta\right) = \begin{pmatrix} Z_{\tau S_I}\frac{\cos(2\theta_{S_I})}{\beta_I} & Z_{\tau S_{II}}\frac{\cos(2\theta_{S_{II}})}{\beta_{II}} \\ Z_{\sigma^f S_I}\frac{\cos(2\theta_{S_I})}{\beta_I} & Z_{\sigma^f S_{II}}\frac{\cos(2\theta_{S_{II}})}{\beta_{II}} \end{pmatrix}, \tag{101}$$

$$\boldsymbol{\rho}\boldsymbol{\Omega}\left(\mathbf{I} - 2p^2\boldsymbol{\beta}\right)\mathbf{R}_\alpha =$$
$$\begin{pmatrix} \underbrace{\chi_1 Z_{\tau S_I}\frac{\cos(2\theta_{S_I})}{\beta_I}}_{c_1} + \underbrace{\frac{\beta_I}{\beta_{II}}\chi_3 Z_{\tau S_{II}}\frac{\cos(2\theta_{S_{II}})}{\beta_I}}_{c_2} & \underbrace{\frac{\beta_{II}}{\beta_I}\chi_2 Z_{\tau S_I}\frac{\cos(2\theta_{S_I})}{\beta_{II}}}_{c_3} + \underbrace{\chi_4 Z_{\tau S_{II}}\frac{\cos(2\theta_{S_{II}})}{\beta_I}}_{c_4} \\ \underbrace{\chi_1 Z_{\sigma S_I}\frac{\cos(2\theta_{S_I})}{\beta_I}}_{c_5} + \underbrace{\frac{\beta_I}{\beta_{II}}\chi_3 Z_{\sigma S_{II}}\frac{\cos(2\theta_{S_{II}})}{\beta_I}}_{c_6} & \underbrace{\frac{\beta_{II}}{\beta_I}\chi_2 Z_{\sigma S_I}\frac{\cos(2\theta_{S_I})}{\beta_{II}}}_{c_7} + \underbrace{\chi_4 Z_{\sigma S_{II}}\frac{\cos(2\theta_{S_{II}})}{\beta_I}}_{c_8} \end{pmatrix}, \tag{102}$$

and

$$2p\boldsymbol{\rho\Omega\beta}\mathbf{R}_\alpha\mathbf{Q}_\alpha = \begin{pmatrix} \underbrace{\left(\dfrac{\beta_\mathrm{I}}{\alpha_\mathrm{I}}\chi_1 Z_{\tau\mathrm{S_I}} + \dfrac{\beta_\mathrm{I\!I}}{\alpha_\mathrm{I}}\chi_3 Z_{\tau\mathrm{S_{I\!I}}}\right)\dfrac{\sin(2\theta_{\mathrm{P_I}})}{\alpha_\mathrm{I}}}_{d_1} & \underbrace{\left(\dfrac{\beta_\mathrm{I}}{\alpha_\mathrm{I\!I}}\chi_2 Z_{\tau\mathrm{S_I}} + \dfrac{\beta_\mathrm{I\!I}}{\alpha_\mathrm{I\!I}}\chi_4 Z_{\tau\mathrm{S_{I\!I}}}\right)\dfrac{\sin(2\theta_{\mathrm{P_{I\!I}}})}{\alpha_\mathrm{I\!I}}}_{d_2} \\[2em] \underbrace{\left(\dfrac{\beta_\mathrm{I}}{\alpha_\mathrm{I}}\chi_1 Z_{\sigma\mathrm{S_I}} + \dfrac{\beta_\mathrm{I\!I}}{\alpha_\mathrm{I}}\chi_3 Z_{\sigma\mathrm{S_{I\!I}}}\right)\dfrac{\sin(2\theta_{\mathrm{P_I}})}{\alpha_\mathrm{I}}}_{d_3} & \underbrace{\left(\dfrac{\beta_\mathrm{I}}{\alpha_\mathrm{I\!I}}\chi_2 Z_{\sigma\mathrm{S_I}} + \dfrac{\beta_\mathrm{I\!I}}{\alpha_\mathrm{I\!I}}\chi_4 Z_{\sigma\mathrm{S_{I\!I}}}\right)\dfrac{\sin(2\theta_{\mathrm{P_{I\!I}}})}{\alpha_\mathrm{I\!I}}}_{d_4} \end{pmatrix}. \tag{103}$$

The terms c and d are introduced for compactness in establishing the reflection-transmission systems. The terms $Z_{\tau\mathrm{S_I}}$, $Z_{\tau\mathrm{S_{I\!I}}}$, $Z_{\sigma\mathrm{S_I}}$, and $Z_{\sigma\mathrm{S_{I\!I}}}$ are the elements of the shear waves impedance matrix $\mathbf{Z}_\beta$ that is defined as

$$\mathbf{Z}_\beta = \boldsymbol{\rho\Omega}\mathbf{R}_\beta\begin{pmatrix} \beta_\mathrm{I} & 0 \\ 0 & \beta_\mathrm{I\!I} \end{pmatrix} \equiv \begin{pmatrix} Z_{\tau\mathrm{S_I}} & Z_{\tau\mathrm{S_{I\!I}}} \\ Z_{\sigma^\mathrm{f}\mathrm{S_I}} & Z_{\sigma^\mathrm{f}\mathrm{S_{I\!I}}} \end{pmatrix}. \tag{104}$$

The interactions of P- and SV-waves are

$$\boldsymbol{\chi} = \mathbf{L}_\beta^T\mathbf{R}_\alpha \equiv \begin{pmatrix} \chi_1 & \chi_2 \\ \chi_3 & \chi_4 \end{pmatrix}, \tag{105}$$

where χ_1 gives the interaction of fast P- and fast S-waves, χ_2 gives the interaction of fast S- and slow P-waves, χ_3 is the interaction of the slow S- and the fast P-waves, and χ_4 is the interaction of the slow S- and slow P-waves.

5.2 SH-waves across a planar contact

For the case of SH-waves, an incident wave generates two reflected and two transmitted waves. Because the fast SH wave is the only propagating wave, the scattering of the slow S-waves, which are diffusive processes, is not expected. However, the reflection-transmission problem for those waves is established for completeness. Figure 11 shows the different kinds of incident, reflected and transmitted waves.

The incident and scattered waves are described by the plane wave solution 22, and the amplitude of the last ones are presented in a matrix as

$$\mathbf{x} = \left(\begin{array}{cc|cc} r_{\grave{S}_I\acute{S}_I} & r_{\grave{S}_{II}\acute{S}_I} & t_{\acute{S}_I\acute{S}_I} & t_{\acute{S}_{II}\acute{S}_I} \\[4pt] r_{\grave{S}_I\acute{S}_{II}} & r_{\grave{S}_{II}\acute{S}_{II}} & t_{\acute{S}_I\acute{S}_{II}} & t_{\acute{S}_{II}\acute{S}_{II}} \\ \hline t_{\grave{S}_I\grave{S}_I} & t_{\grave{S}_{II}\grave{S}_I} & r_{\acute{S}_I\grave{S}_I} & r_{\acute{S}_{II}\grave{S}_I} \\[4pt] t_{\grave{S}_I\grave{S}_{II}} & t_{\grave{S}_{II}\grave{S}_{II}} & r_{\acute{S}_I\grave{S}_{II}} & r_{\acute{S}_{II}\grave{S}_{II}} \end{array}\right). \tag{106}$$

Herein, r and t stand for the reflection and transmission coefficients, respectively. The sub-indexes identify the incident (first sub-index) and scattered (second sub-index) waves. Herein, ´and `identify the up-going and down-going waves, respectively.
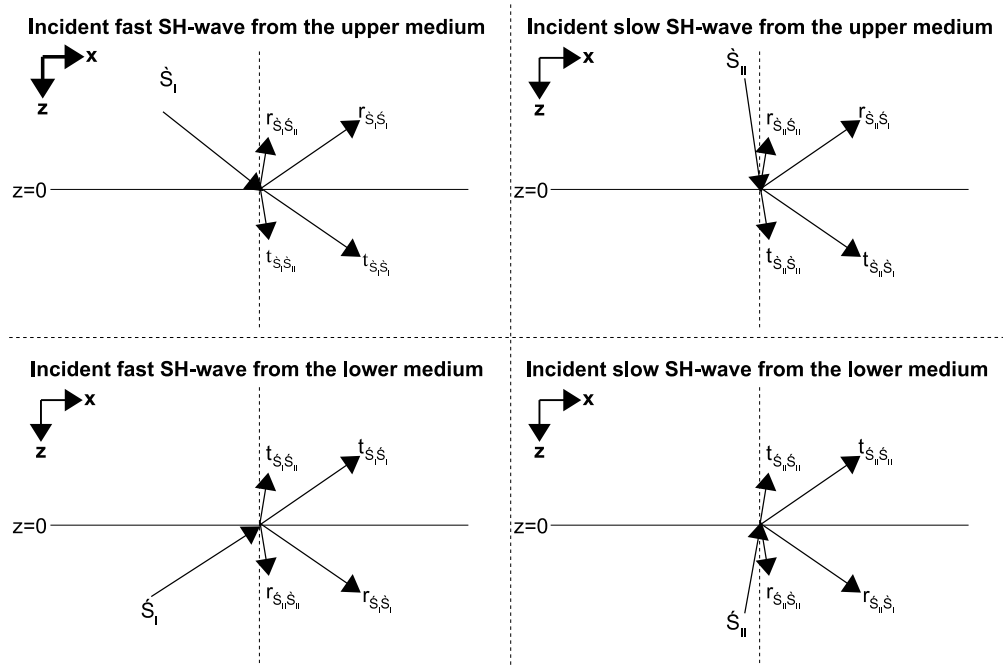
Figure 11. Schematic representation of the SH-waves scattered in a porous-porous contact.

The values of the scattering matrix 106 are obtained by solving the reflection and transmission problem for each incident wave.

5.2.1 Reflection and transmission coefficients for an impermeable contact

Let us consider two poroelastic half-spaces in an impermeable welded contact. The boundary is defined by the plane $z = 0$. The upper ($z<0$) and lower ($z>0$) media are identified by the superscripts (a) and (b), respectively. For an impermeable contact, the boundary conditions are defined by equations 50, 52, and 63. From the solution for

the SH-waves (equation 22) and their respective stresses (equation 23), the reflection and transmission system for the scattering matrix 106 is

$$\mathbf{A}_{SH}\mathbf{X}_{SH} = \mathbf{B}_{SH}. \tag{107}$$

Here,

$$\mathbf{A}_{SH} = \begin{pmatrix} -1 & -\gamma_{\beta_{\mathrm{II}}}^{(a)} & 1 & \gamma_{\beta_{\mathrm{II}}}^{(b)} \\ Z_{\tau S_I}^{(a)}\cos(\theta_{S_I}^{(a)}) & Z_{\tau S_{\mathrm{II}}}^{(a)}\cos(\theta_{S_{\mathrm{II}}}^{(a)}) & Z_{\tau S_I}^{(b)}\cos(\theta_{S_I}^{(b)}) & Z_{\tau S_{\mathrm{II}}}^{(b)}\cos(\theta_{S_{\mathrm{II}}}^{(b)}) \\ -\gamma_{\beta_I}^{(a)} & -1 & 0 & 0 \\ 0 & 0 & \gamma_{\beta_I}^{(b)} & 1 \end{pmatrix}, \tag{108}$$

and

$$\mathbf{B}_{SH} = \begin{pmatrix} 1 & \gamma_{\beta_{\mathrm{II}}}^{(a)} & -1 & -\gamma_{\beta_{\mathrm{II}}}^{(b)} \\ Z_{\tau S_I}^{(a)}\cos(\theta_{S_I}^{(a)}) & Z_{\tau S_{\mathrm{II}}}^{(a)}\cos(\theta_{S_{\mathrm{II}}}^{(a)}) & Z_{\tau S_I}^{(b)}\cos(\theta_{S_I}^{(b)}) & Z_{\tau S_{\mathrm{II}}}^{(b)}\cos(\theta_{S_{\mathrm{II}}}^{(b)}) \\ \gamma_{\beta_I}^{(a)} & 1 & 0 & 0 \\ 0 & 0 & -\gamma_{\beta_I}^{(b)} & -1 \end{pmatrix}. \tag{109}$$

In the limit to the Biot theory, the system is determined by the boundary conditions 50 and 52. Because the slow SH-wave does not exist in this limit, the reflection-transmission problem can be derived from equations 108 and 109 by removing, in both matrices, columns two and four, related to the reflected and transmitted slow S-waves. Also, rows three and four have to be removed because they correspond to the no-slip boundary condition of the fluid that is not accounted for in the Biot theory.

5.2.1.1 Effect of the fluid viscous stress tensor

To analyze the effect of the fluid viscous stress tensor, let us consider an incident fast SH-wave from the upper-medium. In this case, the solution for the system 107 gives the following reflection and transmission coefficients

$$t_{\dot{S}_I\dot{S}_I} = \frac{2\Delta_{R_\beta}^{(a)}Z_{\tau S_I}^{(a)}\cos(\theta_{\beta_I}^{(a)})}{\Delta_{R_\beta}^{(b)}\left(Z_{\tau S_I}^{(a)}\cos(\theta_{\beta_I}^{(a)}) - \gamma_{\beta_I}^{(a)}Z_{\tau S_{\mathrm{II}}}^{(a)}\cos(\theta_{\beta_{\mathrm{II}}}^{(a)})\right) + \Delta_{R_\beta}^{(a)}\left(Z_{\tau S_I}^{(b)}\cos(\theta_{\beta_I}^{(b)}) - \gamma_{\beta_I}^{(b)}Z_{\tau S_{\mathrm{II}}}^{(b)}\cos(\theta_{\beta_{\mathrm{II}}}^{(b)})\right)}, \tag{110}$$

$$t_{\dot{S}_I\dot{S}_{\mathrm{II}}} = -\gamma_{\beta_I}^{(b)}t_{\dot{S}_I\dot{S}_{I'}} \tag{111}$$

$$r_{\dot{S}_I \acute{S}_I} = t_{\dot{S}_I \dot{S}_I} - 1, \tag{112}$$

$$r_{\dot{S}_I \acute{S}_{II}} = -\gamma_{\beta_I}^{(a)} t_{\dot{S}_I \dot{S}_{I'}} \tag{113}$$

Herein, $\Delta_{R_\beta} = 1 - \gamma_{\beta_I}\gamma_{\beta_{II}}$ is the determinant of the $\mathbf{R}_\beta$ matrix.

The equation 110 shows that the amplitude of the transmitted wave is affected by the shear forces generated by the viscous fluid, introduced by the term $Z_{\tau S_{II}}$. Additionally, the term $\Delta_{R_\beta} \neq 1$ indicates that the displacements are affected by the generation of the slow S-wave.

Because the fluid viscous stress tensor is absent in the Biot theory, its effects are not present. It can be seen in the reflection and transmission coefficients which are defined as

$$t_{\dot{S}\dot{S}_{Biot}} = \frac{2Z_{S_{Biot}}^{(a)}\cos(\theta_{\beta_{Biot}}^{(a)})}{Z_{S_{Biot}}^{(a)}\cos(\theta_{\beta_{Biot}}^{(a)}) + Z_{S_{Biot}}^{(b)}\cos(\theta_{\beta_{Biot}}^{(b)})}, \tag{114}$$

$$r_{\dot{S}\acute{S}_{Biot}} = t_{\dot{S}\dot{S}_{Biot}} - 1. \tag{115}$$

The term $Z_{S_{Biot}} = (\rho_m + \rho_f \gamma_{\beta_{Biot}})\beta_{Biot}$ is the impedance for shear waves in the Biot theory. Herein, the coefficients 114 and 115 have the same form as a pure elastic solution, and the viscous forces of the fluid do not affect the coefficients.

The comparison of coefficients in both theories shows that the fluid viscous stress tensor in the dCS theory induces a change in the amplitude of the transmitted waves, which does not exist in the Biot theory. It is apparent in the limit of two porous media with the same properties. In such a case, the solution in the Biot theory predicts that the wave is wholly transmitted ($t_{\dot{S}\dot{S}_{Biot}} = 1$). In contrast, the transmission amplitude in the dCS theory is

$$t_{\dot{S}_I \dot{S}_I} = \frac{Z_{\tau S_I}\cos(\theta_{\beta_I})}{Z_{\tau S_I}\cos(\theta_{\beta_I}) - \gamma_I Z_{\tau S_{II}}\cos(\theta_{\beta_{II}})}. \tag{116}$$

The expression 116 shows that even though both media are the same, an impermeable surface causes a change in the amplitude. It is a consequence of the vanishing of the filtration displacement field at the impermeable surface that generates a change in the total stress by the factor $-\gamma_I Z_{\tau S_{II}}$. Such behavior is illustrated in Figure 12, which shows the amplitude of the scattered waves at the interface of two water-saturated

sintered glass beads porous samples (properties in Table 1 of Appendix A) with the same properties and an impermeable surface. It shows that the fast SH-wave is almost completely transmitted in the low-frequency regime ($\omega \ll \Omega_i$). Around the critical frequency ($\omega \sim \Omega_i$), this amplitude has a small increase that is barely perceptible in the plot. As the frequency is above Ω_i, the amplitude of the transmitted fast SH-wave decreases with frequency, and, in turn, the reflected fast SH-wave increases by the same magnitude. This behavior is also enhanced by the incident angle (θ_{β_I}). Additionally, the reflected and transmitted slow SH-waves are generated with the same amplitude in both media.
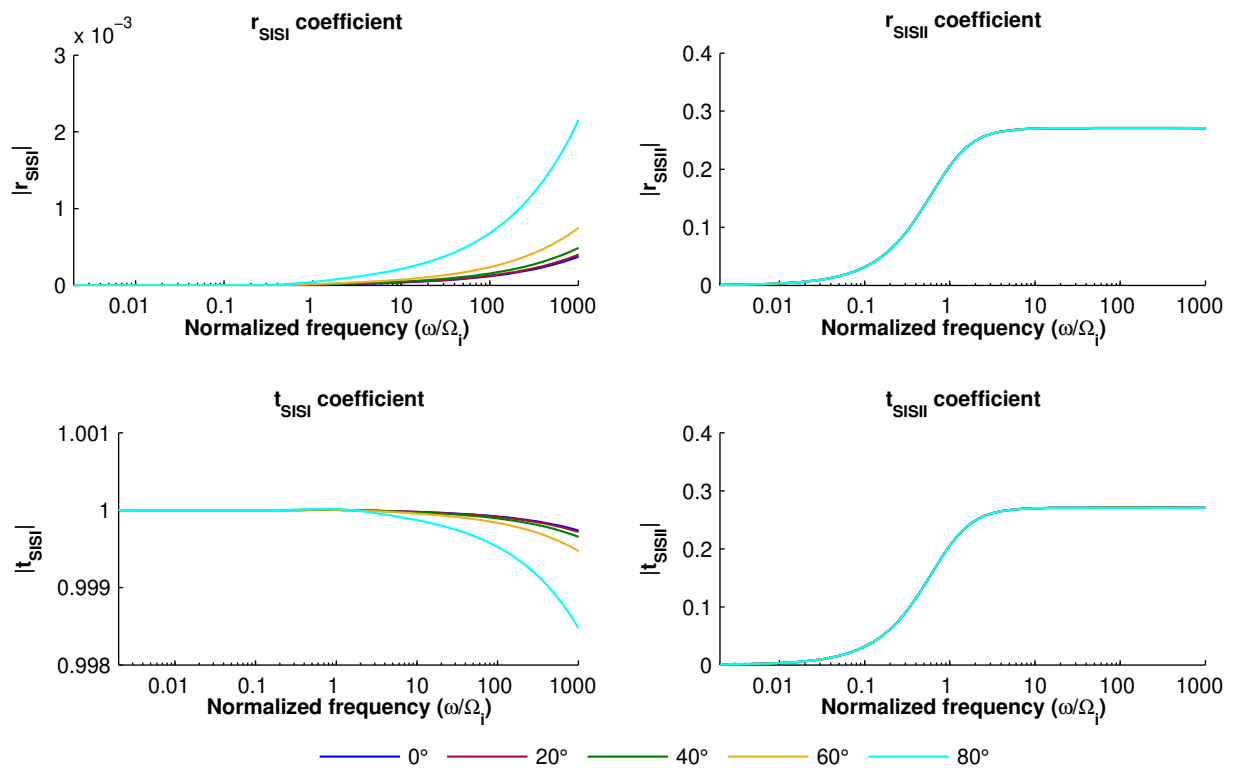
Figure 12. Amplitude of the reflection and transmission coefficients for a fast SH-wave incident at an impermeable contact of two porous media with the same properties. The amplitude is plotted as a function of frequency, and it is presented for the incident angles 0° (blue), 20° (red), 40° (green), 60° (yellow), and 80° (cyan).

The reflection and transmission coefficients for the case of two porous media with different properties, equations 110-113, are presented in Figure 13. The upper half-space is considered a Berea sandstone, which properties are in Table 2 of Appendix A, and the lower half-space is the sintered glass beads porous medium. This figure

shows the variation of reflection and transmission coefficients with the incident angle for $\omega = 0.01\Omega_i^{(b)}$, $\omega = \Omega_i^{(b)}$, $\omega = 10\Omega_i^{(b)}$, $\omega = 100\Omega_i^{(b)}$, and $\omega = 1000\Omega_i^{(b)}$. Where $\Omega_i^{(b)}$ is the critical frequency of the lower half-space. In that range of frequencies, there are critical angles for the fast SH wave that span from 65.8° at $\omega = 1000\Omega_i^{(b)}$ to 76.3° at $\omega = 0.01\Omega_i^{(b)}$. The amplitude of the scattered waves is governed by the contrast in elastic properties and density. It has the same behavior than in the Biot theory. Moreover, the fluid viscous stress tensor causes an additional effect of minor impact in the amplitude.
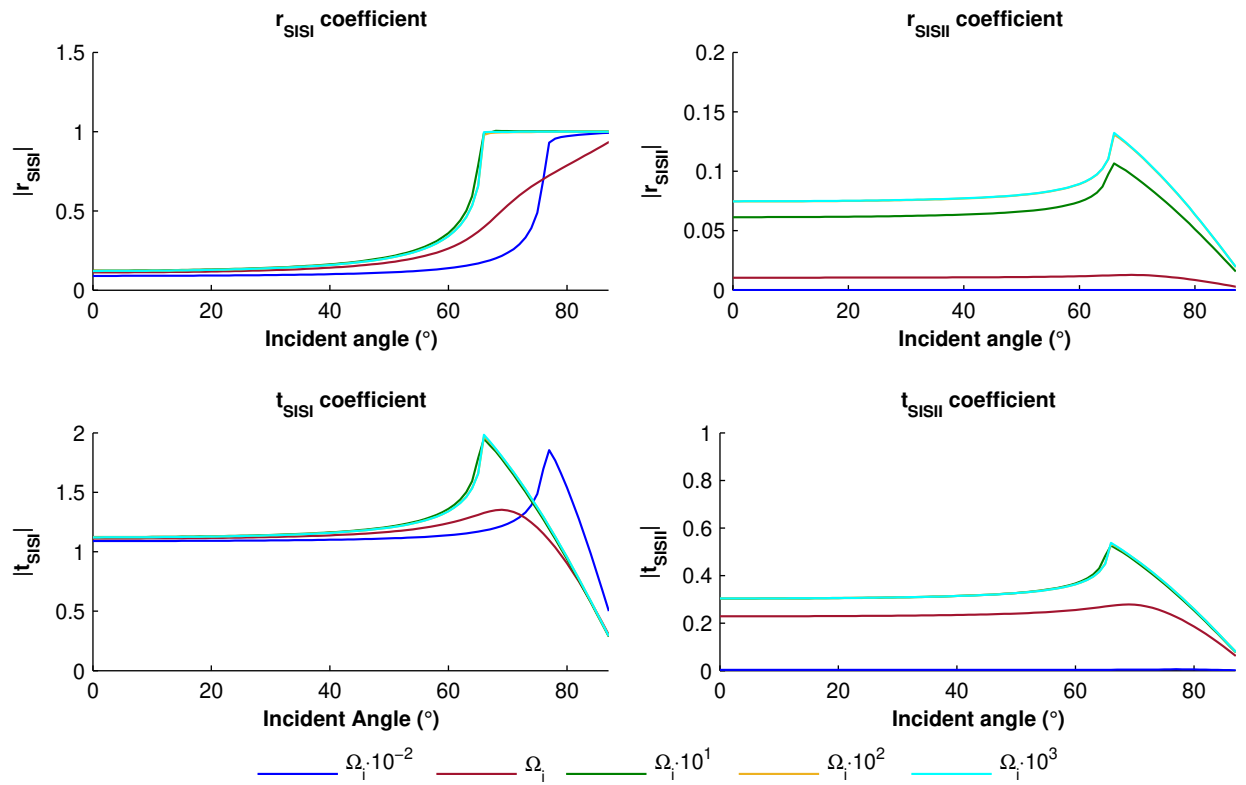
Figure 13. Amplitude of the reflection and transmission coefficients for a fast SH-wave incident at an impermeable contact of two porous media. The upper-medium is a Berea sandstone, and the lower is a sintered glass beads porous medium. The amplitudes are presented respect to incident angle for the $\Omega_i \cdot 10^{-2}$ (blue), Ω_i (red), $\Omega_i \cdot 10^1$ (green), $\Omega_i \cdot 10^2$ (yellow), and $\Omega_i \cdot 10^3$ (cyan) frequencies.

The relative difference of the reflected and transmitted fast SH-waves is presented in Figure 14. The relative difference is computed only with the fast S-waves. Figure 14 shows that the amplitudes predicted in the dCS theory are smaller than those of the Biot theory. The reduction in amplitude due to the viscous stress tensor is of the same order as that observed in Figure 13. However, it is smaller than the change in

amplitude generated by the contrast in elastic properties.
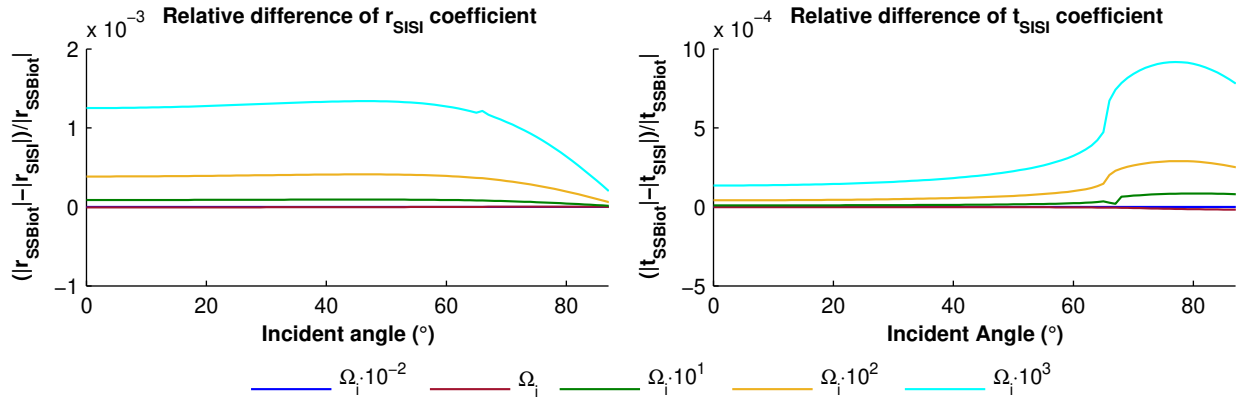
Figure 14. Relative difference of the reflection and transmission coefficients for a fast SH-wave incident at an impermeable contact of two porous media. The upper-medium is a Berea sandstone, and the lower is a sintered glass beads porous medium. The amplitudes are presented respect to incident angle for the $\Omega_i \cdot 10^{-2}$ (blue), Ω_i (red), $\Omega_i \cdot 10^1$ (green), $\Omega_i \cdot 10^2$ (yellow), and $\Omega_i \cdot 10^3$ (cyan) frequencies.

5.2.2 Reflection and transmission coefficients for a permeable contact

For a permeable contact, the boundary conditions are defined by equations 50, 52, 64 and 65. In this case, the system 107 holds; however, the terms **A** and **B** change to

$$
\mathbf{A}_{\text{SH}} = \begin{pmatrix}
-1 & -\gamma_{\beta_{\mathbb{II}}}^{(a)} & 1 & \gamma_{\beta_{\mathbb{II}}}^{(b)} \\
Z_{\tau S_I}^{(a)}\cos(\theta_{S_I}^{(a)}) & Z_{\tau S_{\mathbb{II}}}^{(a)}\cos(\theta_{S_{\mathbb{II}}}^{(a)}) & Z_{\tau S_I}^{(b)}\cos(\theta_{S_I^{(b)}}^{(b)}) & Z_{\tau S_{\mathbb{II}}}^{(b)}\cos(\theta_{S_{\mathbb{II}}}^{(b)}) \\
-\gamma_{\beta_I}^{(a)} & -1 & \gamma_{\beta_I}^{(b)} & 1 \\
Z_{\sigma S_I}^{(a)}\cos(\theta_{S_I}^{(a)}) & Z_{\sigma S_{\mathbb{II}}}^{(a)}\cos(\theta_{S_{\mathbb{II}}}^{(a)}) & Z_{\sigma S_I}^{(b)}\cos(\theta_{S_I^{(b)}}^{(b)}) & Z_{\sigma S_{\mathbb{II}}}^{(b)}\cos(\theta_{S_{\mathbb{II}}}^{(b)})
\end{pmatrix}
\tag{117}
$$

$$
\mathbf{B}_{\text{SH}} = \begin{pmatrix}
1 & \gamma_{\beta_{\mathbb{II}}}^{(a)} & -1 & -\gamma_{\beta_{\mathbb{II}}}^{(b)} \\
Z_{\tau S_I}^{(a)}\cos(\theta_{S_I}^{(a)}) & Z_{\tau S_{\mathbb{II}}}^{(a)}\cos(\theta_{S_{\mathbb{II}}}^{(a)}) & Z_{\tau S_I}^{(b)}\cos(\theta_{S_I}^{(b)}) & Z_{\tau S_{\mathbb{II}}}^{(b)}\cos(\theta_{S_{\mathbb{II}}}^{(b)}) \\
\gamma_{\beta_I}^{(a)} & 1 & -\gamma_{\beta_I}^{(b)} & -1 \\
Z_{\sigma S_I}^{(a)}\cos(\theta_{S_I}^{(a)}) & Z_{\sigma S_{\mathbb{II}}}^{(a)}\cos(\theta_{S_{\mathbb{II}}}^{(a)}) & Z_{\sigma S_I}^{(b)}\cos(\theta_{S_I}^{(b)}) & Z_{\sigma S_{\mathbb{II}}}^{(b)}\cos(\theta_{S_{\mathbb{II}}}^{(b)})
\end{pmatrix},
\tag{118}
$$

The Biot theory determines the system by the same boundary conditions as in the previous case. They are 50 and 52. Therefore, there is no difference between the permeable and impermeable interfaces.

5.2.2.1 Effect of the fluid viscous stress tensor

To analyze the effect of the fluid viscous stress tensor in a permeable contact, let me examine the coefficients for an incident fast SH-wave from the upper-medium. In this case, the reflection and transmission coefficients are

$$
t_{\acute{S}_I\grave{S}_I} = \frac{2\left(g_1\Delta_{Z_\beta}^{(a)}\cos(\theta_{S_I}^{(a)})\cos(\theta_{S_{II}}^{(a)}) + f_2\Delta_{R_\beta}^{(a)}\right)}{\Delta_{R_\beta}^{(b)}\Delta_{Z_\beta}^{(a)}\cos(\theta_{S_I}^{(a)})\cos(\theta_{S_{II}}^{(a)}) + f_2g_2 + f_3\delta_{\gamma_{\beta_{II}}} + \Delta_{R_\beta}^{(a)}\Delta_{Z_\beta}^{(b)}\cos(\theta_{S_I}^{(b)})\cos(\theta_{S_{II}}^{(b)}) + f_1g_1 + f_4\delta_{\gamma_{\beta_I}}},
$$
$$(119)$$

$$
t_{\acute{S}_I\grave{S}_{II}} = \frac{2\left(\delta_{\gamma_{\beta_I}}\Delta_{Z_\beta}^{(a)}\cos(\theta_{S_I}^{(a)})\cos(\theta_{S_{II}}^{(a)}) - f_3\Delta_{R_\beta}^{(b)}\right)}{\Delta_{R_\beta}^{(b)}\Delta_{Z_\beta}^{(a)}\cos(\theta_{S_I}^{(a)})\cos(\theta_{S_{II}}^{(a)}) + f_2g_2 + f_3\delta_{\gamma_{\beta_{II}}} + \Delta_{R_\beta}^{(a)}\Delta_{Z_\beta}^{(b)}\cos(\theta_{S_I}^{(b)})\cos(\theta_{S_{II}}^{(b)}) + f_1g_1 + f_4\delta_{\gamma_{\beta_I}}},
$$
$$(120)$$

$$
r_{\acute{S}_I\acute{S}_I} = \frac{\Delta_{R_\beta}^{(b)}\Delta_{Z_\beta}^{(a)}\cos(\theta_{S_I}^{(a)})\cos(\theta_{S_{II}}^{(a)}) + f_2g_2 + f_3\delta_{\gamma_{\beta_{II}}} - \Delta_{R_\beta}^{(a)}\Delta_{Z_\beta}^{(b)}\cos(\theta_{S_I}^{(b)})\cos(\theta_{S_{II}}^{(b)}) - f_1g_1 - f_4\delta_{\gamma_{\beta_I}}}{\Delta_{R_\beta}^{(b)}\Delta_{Z_\beta}^{(a)}\cos(\theta_{S_I}^{(a)})\cos(\theta_{S_{II}}^{(a)}) + f_2g_2 + f_3\delta_{\gamma_{\beta_{II}}} + \Delta_{R_\beta}^{(a)}\Delta_{Z_\beta}^{(b)}\cos(\theta_{S_I}^{(b)})\cos(\theta_{S_{II}}^{(b)}) + f_1g_1 + f_4\delta_{\gamma_{\beta_I}}},
$$
$$(121)$$

$$
r_{\acute{S}_I\acute{S}_{II}} = \frac{-2\left(f_3g_1 + f_2\delta_{\gamma_{\beta_I}}\right)}{\Delta_{R_\beta}^{(b)}\Delta_{Z_\beta}^{(a)}\cos(\theta_{S_I}^{(a)})\cos(\theta_{S_{II}}^{(a)}) + f_2g_2 + f_3\delta_{\gamma_{\beta_{II}}} + \Delta_{R_\beta}^{(a)}\Delta_{Z_\beta}^{(b)}\cos(\theta_{S_I}^{(b)})\cos(\theta_{S_{II}}^{(b)}) + f_1g_1 + f_4\delta_{\gamma_{\beta_I}}}.
$$
$$(122)$$

Herein Δ_{Z_β} is the determinant of the $\mathbf{Z}_\beta$ matrix. The terms $\delta_{\gamma_{\beta_I}} = \gamma_{\beta_I}^{(a)} - \gamma_{\beta_I}^{(b)}$ and $\delta_{\gamma_{\beta_{II}}} = \gamma_{\beta_{II}}^{(a)} - \gamma_{\beta_{II}}^{(b)}$ are the differences of γ_{β_I} and $\gamma_{\beta_{II}}$ terms, respectively. Also, the following terms are introduced

$$
f_1 = \left(Z_{\tau S_I}^{(b)}Z_{\sigma S_{II}}^{(a)} - Z_{\tau S_{II}}^{(a)}Z_{\sigma S_I}^{(b)}\right)\cos(\theta_{S_I}^{(b)})\cos(\theta_{S_{II}}^{(a)}), \tag{123}
$$

$$
f_2 = \left(Z_{\tau S_I}^{(a)}Z_{\sigma S_{II}}^{(b)} - Z_{\tau S_{II}}^{(b)}Z_{\sigma S_I}^{(a)}\right)\cos(\theta_{S_I}^{(a)})\cos(\theta_{S_{II}}^{(b)}), \tag{124}
$$

$$
f_3 = \left(Z_{\tau S_I}^{(a)}Z_{\sigma S_I}^{(b)} - Z_{\tau S_I}^{(b)}Z_{\sigma S_I}^{(a)}\right)\cos(\theta_{S_I}^{(a)})\cos(\theta_{S_I}^{(b)}), \tag{125}
$$

$$
f_4 = \left(Z_{\sigma S_{II}}^{(a)}Z_{\tau S_{II}}^{(b)} - Z_{\sigma S_{II}}^{(b)}Z_{\tau S_{II}}^{(a)}\right)\cos(\theta_{S_{II}}^{(a)})\cos(\theta_{S_{II}}^{(b)}), \tag{126}
$$

$$
g_1 = 1 - \gamma_{\beta_I}^{(a)}\gamma_{\beta_{II}}^{(b)}, \tag{127}
$$

$$
g_2 = 1 - \gamma_{\beta_I}^{(b)}\gamma_{\beta_{II}}^{(a)}. \tag{128}
$$

The coefficients 119 to 122 show that the interaction of the saturating fluids across the contact affects the reflection and transmission coefficients even in a permeable surface. Such an interaction affects all scattered waves, not only the slow SH-waves. As expected, in the limit of two porous media with the same properties, the incident wave is not scattered. Instead, the wave is completely transmitted as if it was a

homogeneous medium.

Figure 15 shows the reflection and transmission coefficients for the case of a Berea sandstone in a permeable contact with a sintered glass beads porous medium. The medium properties are the same than in Figure 13. In this case, the amplitude of the scattered waves shows the same behavior as the scattered waves in an impermeable contact, as they are shown in Figure 13. However, the relative differences with respect to the coefficients in the Biot theory, which are presented in Figure 16, are one order of magnitude smaller than in the impermeable contact (Figure 14). Even so, the effects of the fluid viscous stress tensor are present in the SH-wave scattering in a permeable contact.
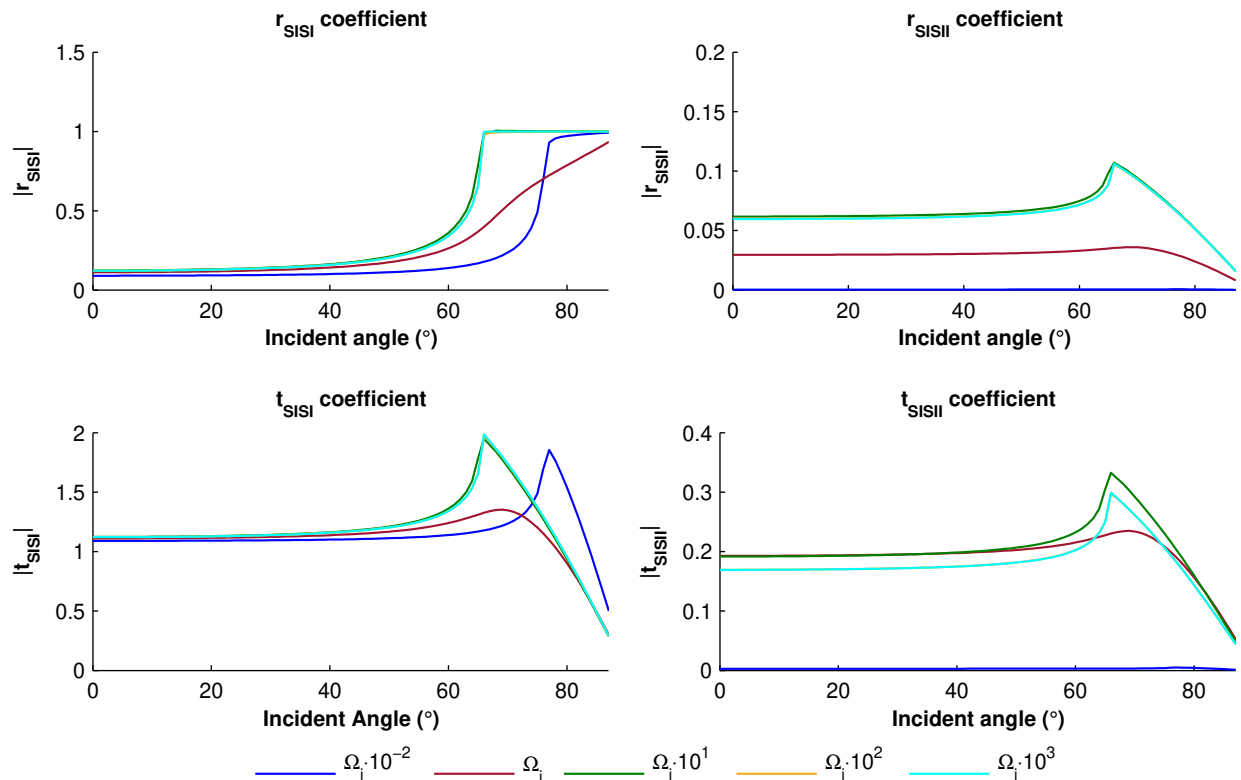
Figure 15. Amplitude of the reflection and transmission coefficients for a fast SH-wave incident at a permeable contact of two porous media. The upper-medium is a Berea sandstone, and the lower is a sintered glass beads porous medium. The amplitudes are plotted as a function of the incident angle, and they are presented for the angular frequencies $\Omega_i \cdot 10^{-2}$ (blue), Ω_i (red), $\Omega_i \cdot 10^1$ (green), $\Omega_i \cdot 10^2$ (yellow), and $\Omega_i \cdot 10^3$ (cyan).
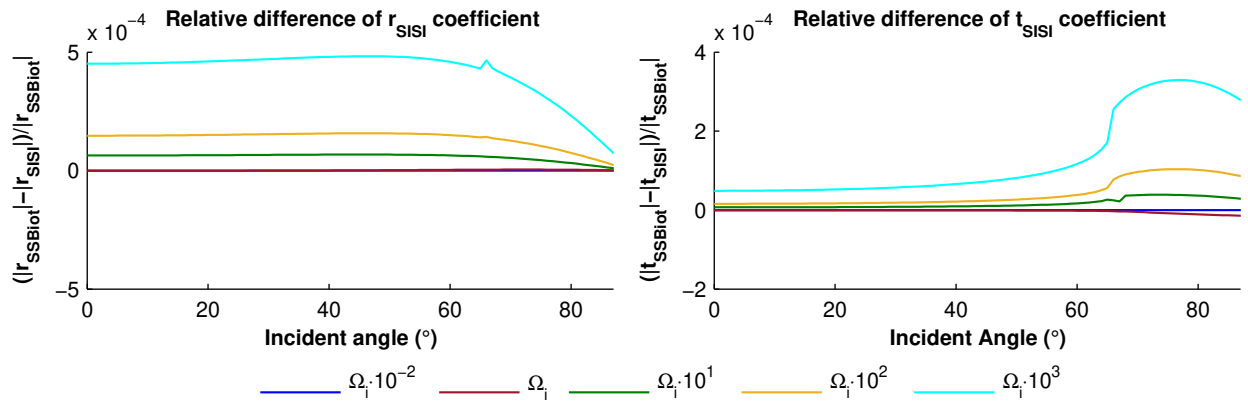
Figure 16. Relative difference of the reflection and transmission coefficients for a fast SH-wave incident at a permeable contact of two porous media. The upper-medium is a Berea sandstone, and the lower is a sintered glass beads porous medium. The amplitudes are plotted as a function of the incident angle, and they are presented for the angular frequencies $\Omega_i \cdot 10^{-2}$ (blue), Ω_i (red), $\Omega_i \cdot 10^1$ (green), $\Omega_i \cdot 10^2$ (yellow), and $\Omega_i \cdot 10^3$ (cyan).

5.3 P- and SV-waves across a planar contact

For the case of P- and SV-waves, the incident wave generates four reflected and four transmitted waves. Figure 17 shows a scheme of the scattered waves for the incident fast waves, and Figure 18 shows those waves for the incident slow waves.
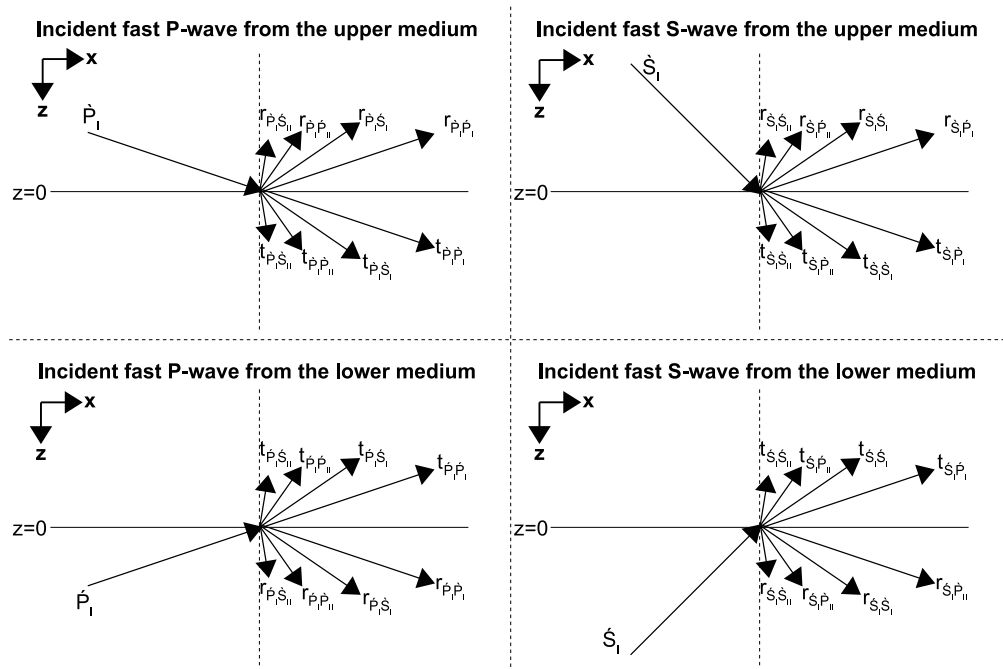
Figure 17. Schematic representation of the P- and SV-waves scattered from the fast waves incident in a porous-porous contact.
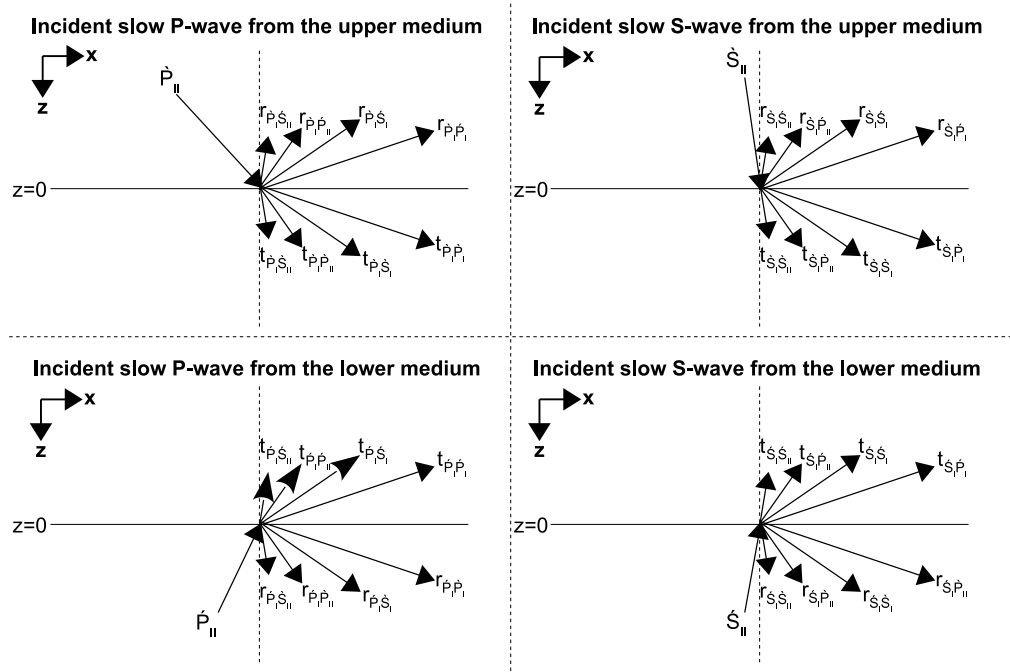
Figure 18. Schematic representation of the P- and SV-waves scattered from the slow waves incident in a porous-porous contact.

The incident and scattered P-waves are described by the plane wave solution 30; whereas the solution 31 describes the S-waves. The amplitude coefficients of these scattered waves, presented in a matrix, are

$$
\mathbf{X}_{\mathrm{PSV}} = \left(
\begin{array}{cccc|cccc}
r_{\grave{P}_I\acute{P}_I} & r_{\grave{P}_{II}\acute{P}_I} & r_{\grave{S}_I\acute{P}_I} & r_{\grave{S}_{II}\acute{P}_I} & t_{\acute{P}_I\acute{P}_I} & t_{\acute{P}_{II}\acute{P}_I} & t_{\acute{S}_I\acute{P}_I} & t_{\acute{S}_{II}\acute{P}_I} \\
r_{\grave{P}_I\acute{P}_{II}} & r_{\grave{P}_{II}\acute{P}_{II}} & r_{\grave{S}_I\acute{P}_{II}} & r_{\grave{S}_{II}\acute{P}_{II}} & t_{\acute{P}_I\acute{P}_{II}} & t_{\acute{P}_{II}\acute{P}_{II}} & t_{\acute{S}_I\acute{P}_{II}} & t_{\acute{S}_{II}\acute{P}_{II}} \\
r_{\grave{P}_I\acute{S}_I} & r_{\grave{P}_{II}\acute{S}_I} & r_{\grave{S}_I\acute{S}_I} & r_{\grave{S}_{II}\acute{S}_I} & t_{\acute{P}_I\acute{S}_I} & t_{\acute{P}_{II}\acute{S}_I} & t_{\acute{S}_I\acute{S}_I} & t_{\acute{S}_{II}\acute{S}_I} \\
r_{\grave{P}_I\acute{S}_{II}} & r_{\grave{P}_{II}\acute{S}_{II}} & r_{\grave{S}_I\acute{S}_{II}} & r_{\grave{S}_{II}\acute{S}_{II}} & t_{\acute{P}_I\acute{S}_{II}} & t_{\acute{P}_{II}\acute{S}_{II}} & t_{\acute{S}_I\acute{S}_{II}} & t_{\acute{S}_{II}\acute{S}_{II}} \\
\hline
t_{\grave{P}_I\grave{P}_I} & t_{\grave{P}_{II}\grave{P}_I} & t_{\grave{S}_I\grave{P}_I} & t_{\grave{S}_{II}\grave{P}_I} & r_{\acute{P}_I\grave{P}_I} & r_{\acute{P}_{II}\grave{P}_I} & r_{\acute{S}_I\grave{P}_I} & r_{\acute{S}_{II}\grave{P}_I} \\
t_{\grave{P}_I\grave{P}_{II}} & t_{\grave{P}_{II}\grave{P}_{II}} & t_{\grave{S}_I\grave{P}_{II}} & t_{\grave{S}_{II}\grave{P}_{II}} & r_{\acute{P}_I\grave{P}_{II}} & r_{\acute{P}_{II}\grave{P}_{II}} & r_{\acute{S}_I\grave{P}_{II}} & r_{\acute{S}_{II}\grave{P}_{II}} \\
t_{\grave{P}_I\grave{S}_I} & t_{\grave{P}_{II}\grave{S}_I} & t_{\grave{S}_I\grave{S}_I} & t_{\grave{S}_{II}\grave{S}_I} & r_{\acute{P}_I\grave{S}_I} & r_{\acute{P}_{II}\grave{S}_I} & r_{\acute{S}_I\grave{S}_I} & r_{\acute{S}_{II}\grave{S}_I} \\
t_{\grave{P}_I\grave{S}_{II}} & t_{\grave{P}_{II}\grave{S}_{II}} & t_{\grave{S}_I\grave{S}_{II}} & t_{\grave{S}_{II}\grave{S}_{II}} & r_{\acute{P}_I\grave{S}_{II}} & r_{\acute{P}_{II}\grave{S}_{II}} & r_{\acute{S}_I\grave{S}_{II}} & r_{\acute{S}_{II}\grave{S}_{II}}
\end{array}
\right). \tag{129}
$$

The values of the scattering matrix 129 are obtained by solving the reflection and transmission problem for the incident P- and SV-waves.

5.3.1 Reflection and transmission coefficients for an impermeable contact

For the case of incident P- and SV-waves in an impermeable contact, the boundary conditions for establishing the reflection and transmission problem are the equations 49 to 52, 55, and 63. By substituting the displacements in terms of potentials (equations 32 and 33) and their respective stresses (equations 34 and 35) in the boundary conditions, the reflection and transmission system for the scattering matrix 129 is

$$\mathbf{A}_{\text{PSV}}\,\mathbf{X}_{\text{PSV}} = \mathbf{B}_{\text{PSV}}. \tag{130}$$

Herein

$\mathbf{A}_{\text{PSV}} =$

$$
\begin{pmatrix}
\cos(\theta_{P_I}^{(a)}) & \gamma_{\alpha_{II}}^{(a)}\cos(\theta_{P_{II}}^{(a)}) & -\sin(\theta_{S_I}^{(a)}) & -\gamma_{\beta_{II}}^{(a)}\sin(\theta_{S_{II}}^{(a)}) \\
-\sin(\theta_{P_I}^{(a)}) & -\gamma_{\alpha_{II}}^{(a)}\sin(\theta_{P_{II}}^{(a)}) & -\cos(\theta_{S_I}^{(a)}) & -\gamma_{\beta_{II}}^{(a)}\cos(\theta_{S_{II}}^{(a)}) \\
-c_1^{(a)}\cos(2\theta_{S_I}^{(a)})-c_2^{(a)}\cos(2\theta_{S_{II}}^{(a)}) & -c_3^{(a)}\cos(2\theta_{S_I}^{(a)})-c_4^{(a)}\cos(2\theta_{S_{II}}^{(a)}) & Z_{\tau S_I}^{(a)}\sin(2\theta_{S_I}^{(a)}) & Z_{\tau S_{II}}^{(a)}\sin(2\theta_{S_{II}}^{(a)}) \\
d_1^{(a)}\sin(2\theta_{P_I}^{(a)}) & d_2^{(a)}\sin(2\theta_{P_{II}}^{(a)}) & Z_{\tau S_I}^{(a)}\cos(2\theta_{S_I}^{(a)}) & Z_{\tau S_{II}}^{(a)}\cos(2\theta_{S_{II}}^{(a)}) \\
\gamma_{\alpha_I}^{(a)}\cos(\theta_{P_I}^{(a)}) & \cos(\theta_{P_{II}}^{(a)}) & -\gamma_{\beta_I}^{(a)}\sin(\theta_{S_I}^{(a)}) & -\sin(\theta_{S_{II}}^{(a)}) \\
0 & 0 & 0 & 0 \\
-\gamma_{\alpha_I}^{(a)}\sin(\theta_{P_I}^{(a)}) & -\sin(\theta_{P_{II}}^{(a)}) & -\gamma_{\beta_I}^{(a)}\cos(\theta_{S_I}^{(a)}) & -\cos(\theta_{S_{II}}^{(a)}) \\
0 & 0 & 0 & 0
\end{pmatrix}
$$

$$
\begin{pmatrix}
\cos(\theta_{P_I}^{(b)}) & \gamma_{\alpha_{II}}^{(b)}\cos(\theta_{P_{II}}^{(b)}) & \sin(\theta_{S_I}^{(b)}) & \gamma_{\beta_{II}}^{(b)}\sin(\theta_{S_{II}}^{(b)}) \\
\sin(\theta_{P_I}^{(b)}) & \gamma_{\alpha_{II}}^{(b)}\sin(\theta_{P_{II}}^{(b)}) & -\cos(\theta_{S_I}^{(b)}) & -\gamma_{\beta_{II}}^{(b)}\cos(\theta_{S_{II}}^{(b)}) \\
c_1^{(b)}\cos(2\theta_{S_I}^{(b)})+c_2^{(b)}\cos(2\theta_{S_{II}}^{(b)}) & c_3^{(b)}\cos(2\theta_{S_I}^{(b)})+c_4^{(b)}\cos(2\theta_{S_{II}}^{(b)}) & Z_{\tau S_I}^{(b)}\sin(2\theta_{S_I}^{(b)}) & Z_{\tau S_{II}}^{(b)}\sin(2\theta_{S_{II}}^{(b)}) \\
d_1^{(b)}\sin(2\theta_{P_I}^{(b)}) & d_2^{(b)}\sin(2\theta_{P_{II}}^{(b)}) & -Z_{\tau S_I}^{(b)}\cos(2\theta_{S_I}^{(b)}) & -Z_{\tau S_{II}}^{(b)}\cos(2\theta_{S_{II}}^{(b)}) \\
0 & 0 & 0 & 0 \\
\gamma_{\alpha_I}^{(b)}\cos(\theta_{P_I}^{(b)}) & \cos(\theta_{P_{II}}^{(b)}) & \gamma_{\beta_I}^{(b)}\sin(\theta_{S_I}^{(b)}) & \sin(\theta_{S_{II}}^{(b)}) \\
0 & 0 & 0 & 0 \\
\gamma_{\alpha_I}^{(b)}\sin(\theta_{P_I}^{(b)}) & \sin(\theta_{P_{II}}^{(b)}) & -\gamma_{\beta_I}^{(b)}\cos(\theta_{S_I}^{(b)}) & -\cos(\theta_{S_{II}}^{(b)})
\end{pmatrix},
$$

$$\tag{131}$$

and

$$\mathbf{B}_{PSV} =$$

$$
\begin{pmatrix}
\cos(\theta_{P_I}^{(a)}) & \gamma_{\alpha_{II}}^{(a)}\cos(\theta_{P_{II}}^{(a)}) & \sin(\theta_{S_I}^{(a)}) & \gamma_{\beta_{II}}^{(a)}\sin(\theta_{S_{II}}^{(a)}) & \cos(\theta_{P_I}^{(b)}) & \gamma_{\alpha_{II}}^{(b)}\cos(\theta_{P_{II}}^{(b)}) & -\sin(\theta_{S_I}^{(b)}) & -\gamma_{\beta_{II}}^{(b)}\sin(\theta_{S_{II}}^{(b)}) \\[4pt]
\sin(\theta_{P_I}^{(a)}) & \gamma_{\alpha_{II}}^{(a)}\sin(\theta_{P_{II}}^{(a)}) & -\cos(\theta_{S_I}^{(a)}) & -\gamma_{\beta_{II}}^{(a)}\cos(\theta_{S_{II}}^{(a)}) & -\sin(\theta_{P_I}^{(b)}) & -\gamma_{\alpha_{II}}^{(b)}\sin(\theta_{P_{II}}^{(b)}) & -\cos(\theta_{S_I}^{(b)}) & -\gamma_{\beta_{II}}^{(b)}\cos(\theta_{S_{II}}^{(b)}) \\[4pt]
c_1^{(a)}\cos(2\theta_{S_I}^{(a)})+c_2^{(a)}\cos(2\theta_{S_{II}}^{(a)}) & c_3^{(a)}\cos(2\theta_{S_I}^{(a)})+c_4^{(a)}\cos(2\theta_{S_{II}}^{(a)}) & Z_{\tau S_I}^{(a)}\sin(2\theta_{S_I}^{(a)}) & Z_{\tau S_{II}}^{(a)}\sin(2\theta_{S_{II}}^{(a)}) & -c_1^{(b)}\cos(2\theta_{S_I}^{(b)})-c_2^{(b)}\cos(2\theta_{S_{II}}^{(b)}) & -c_3^{(b)}\cos(2\theta_{S_I}^{(b)})-c_4^{(b)}\cos(2\theta_{S_{II}}^{(b)}) & Z_{\tau S_I}^{(b)}\sin(2\theta_{S_I}^{(b)}) & Z_{\tau S_{II}}^{(b)}\sin(2\theta_{S_{II}}^{(b)}) \\[4pt]
d_1^{(a)}\sin(2\theta_{P_I}^{(a)}) & d_2^{(a)}\sin(2\theta_{P_{II}}^{(a)}) & -Z_{\tau S_I}^{(a)}\cos(2\theta_{S_I}^{(a)}) & -Z_{\tau S_{II}}^{(a)}\cos(2\theta_{S_{II}}^{(a)}) & d_1^{(b)}\sin(2\theta_{P_I}^{(b)}) & d_2^{(b)}\sin(2\theta_{P_{II}}^{(b)}) & Z_{\tau S_I}^{(b)}\cos(2\theta_{S_I}^{(b)}) & Z_{\tau S_{II}}^{(b)}\cos(2\theta_{S_{II}}^{(b)}) \\[4pt]
\gamma_{\alpha_I}^{(a)}\cos(\theta_{P_I}^{(a)}) & \cos(\theta_{P_{II}}^{(a)}) & \gamma_{\beta_I}^{(a)}\sin(\theta_{S_I}^{(a)}) & \sin(\theta_{S_{II}}^{(a)}) & \gamma_{\alpha_I}^{(b)}\cos(\theta_{P_I}^{(b)}) & \cos(\theta_{P_{II}}^{(b)}) & -\gamma_{\beta_I}^{(b)}\sin(\theta_{S_I}^{(b)}) & -\sin(\theta_{S_{II}}^{(b)}) \\[4pt]
0 & 0 & 0 & 0 & 0 & 0 & 0 & 0 \\[4pt]
\gamma_{\alpha_I}^{(a)}\sin(\theta_{P_I}^{(a)}) & \sin(\theta_{P_{II}}^{(a)}) & -\gamma_{\beta_I}^{(a)}\cos(\theta_{S_I}^{(a)}) & -\cos(\theta_{S_{II}}^{(a)}) & -\gamma_{\alpha_I}^{(b)}\sin(\theta_{P_I}^{(b)}) & -\sin(\theta_{P_{II}}^{(b)}) & -\gamma_{\beta_I}^{(b)}\cos(\theta_{S_I}^{(b)}) & -\cos(\theta_{S_{II}}^{(b)}) \\[4pt]
0 & 0 & 0 & 0 & 0 & 0 & 0 & 0
\end{pmatrix}.
$$

$$(132)$$

In the limit to the Biot theory, the system is determined by the boundary conditions 49 to 52, and 55. The reflection and transmission problem can be derived from equations 131 and 132 by removing, in both matrices, columns four and eight, which are related to the reflected and transmitted slow S-waves, respectively. Also, rows seven and eight, which correspond to the no-slip condition of the fluid, have to be removed.

5.3.1.1 Effect of the fluid viscous stress tensor

To examine the impact of the fluid viscous stress tensor, the numerical solution of the system 130 is computed by the Gauss-Jordan elimination method. The pseudocode

for this solution is described in section B.2 of Appendix B.

Figure 19 shows the reflection and transmission coefficients from a fast P-wave traveling across two water-saturated sintered glass beads porous media with the same properties (Table 1 of Appendix A) and an impermeable surface. This figure shows the variation of reflection and transmission coefficients with the incident angle for $\omega = 0.01\Omega_i$, $\omega = \Omega_i$, $\omega = 10\Omega_i$, $\omega = 100\Omega_i$, and $\omega = 1000\Omega_i$. In the low-frequency regime, the incident wave is almost completely transmitted without generating scattered waves. However, in the high-frequency regime, the impermeable contact without any change in properties causes the scattering of the incident fast-P wave. It reduces the amplitude of the transmitted fast P-wave and generates a reflected fast P-wave with the same magnitude. These amplitudes reduce with increasing incident angle, whereas the reflected and transmitted fast S-waves increase with incident angle. The reflected and transmitted slow P-waves have the same behavior. These have an amplitude of 0.12 at the normal incident angle, and the amplitude decreases with increasing the incident angle.The reflected and transmitted slow S-wave amplitude increases with the incident angle.

Although it is not reported before, the scattered waves in an impermeable surface have a similar behavior in the Biot theory. However, the effect of the fluid viscous stress tensor, in the dCS theory, causes a small difference in the amplitude of the scattered waves. It is observed in the relative differences of the coefficients shown in Figure 20. These differences have a negative value for the reflected fast P- and transmitted slow S-waves. In contrast, the rest of the scattered waves show a positive value that increases with the incident angle. The most significant relative difference is observed in the reflected fast P-wave. The reflected and transmitted fast S-waves show the same relative difference with opposite sign and a magnitude in the order of 10^{-2}, one order of magnitude larger than the effects observed in the SH case. The scattered slow P-waves are also affected by the fluid viscous stress tensor in the order of 10^{-3}.

For an incident fast S-wave traveling across two water-saturated sintered glass beads porous media with the same properties, the reflection and transmission coefficients are strongly affected by the impermeable surface (Figure 21). At the normal incident angle ($\theta_{\beta_I} = 0$), the fast S-wave is transmitted with a small reduction in am-
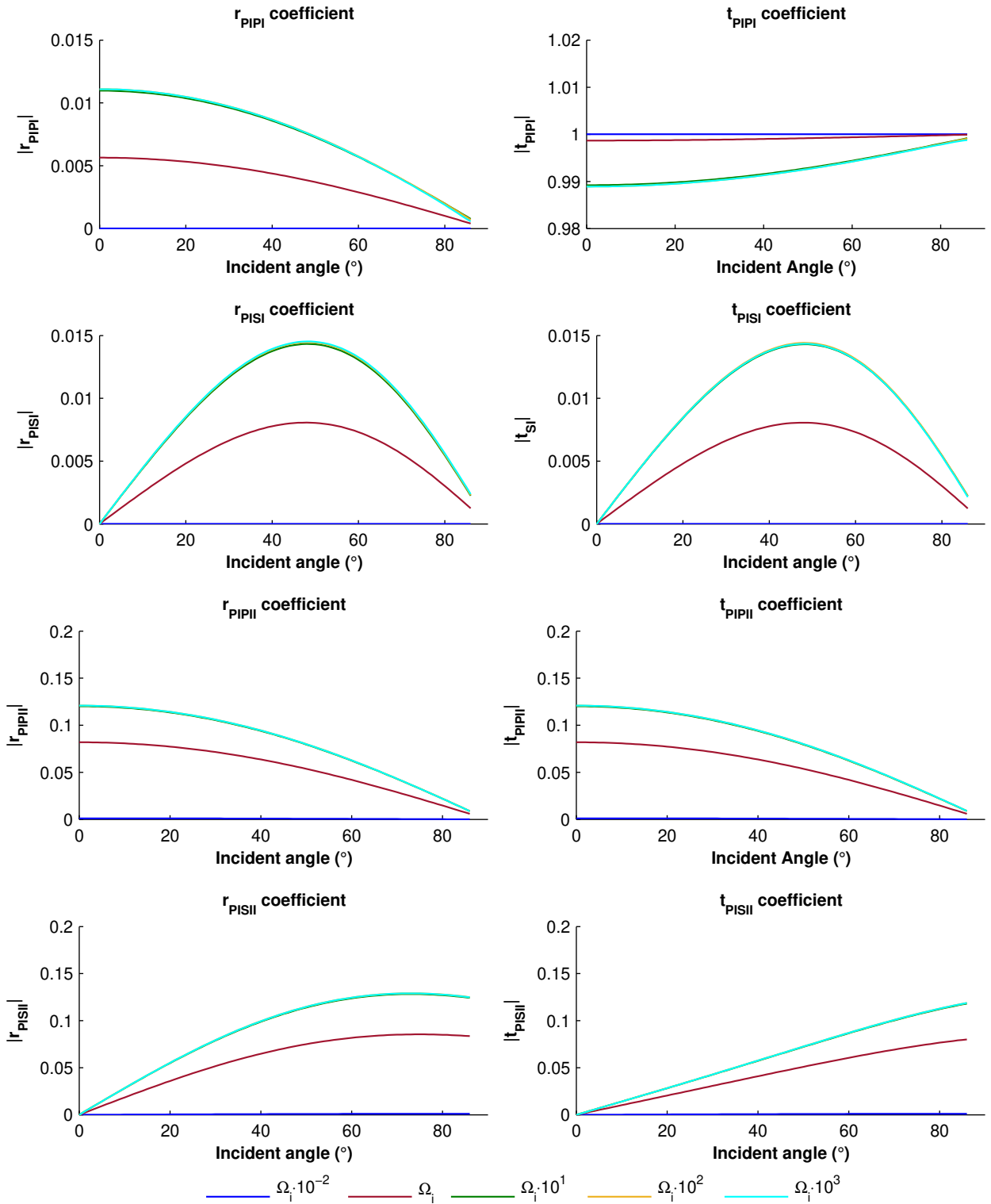
Figure 19. Amplitude of the reflection and transmission coefficients for a fast P-wave incident at an impermeable contact of two water-saturated sintered glass beads porous media with the same properties. The amplitudes are plotted as a function of incident angle, and they are presented for the angular frequencies $\Omega_i \cdot 10^{-2}$ (blue), Ω_i (red), $\Omega_i \cdot 10^1$ (green), $\Omega_i \cdot 10^2$ (yellow), and $\Omega_i \cdot 10^3$ (cyan).
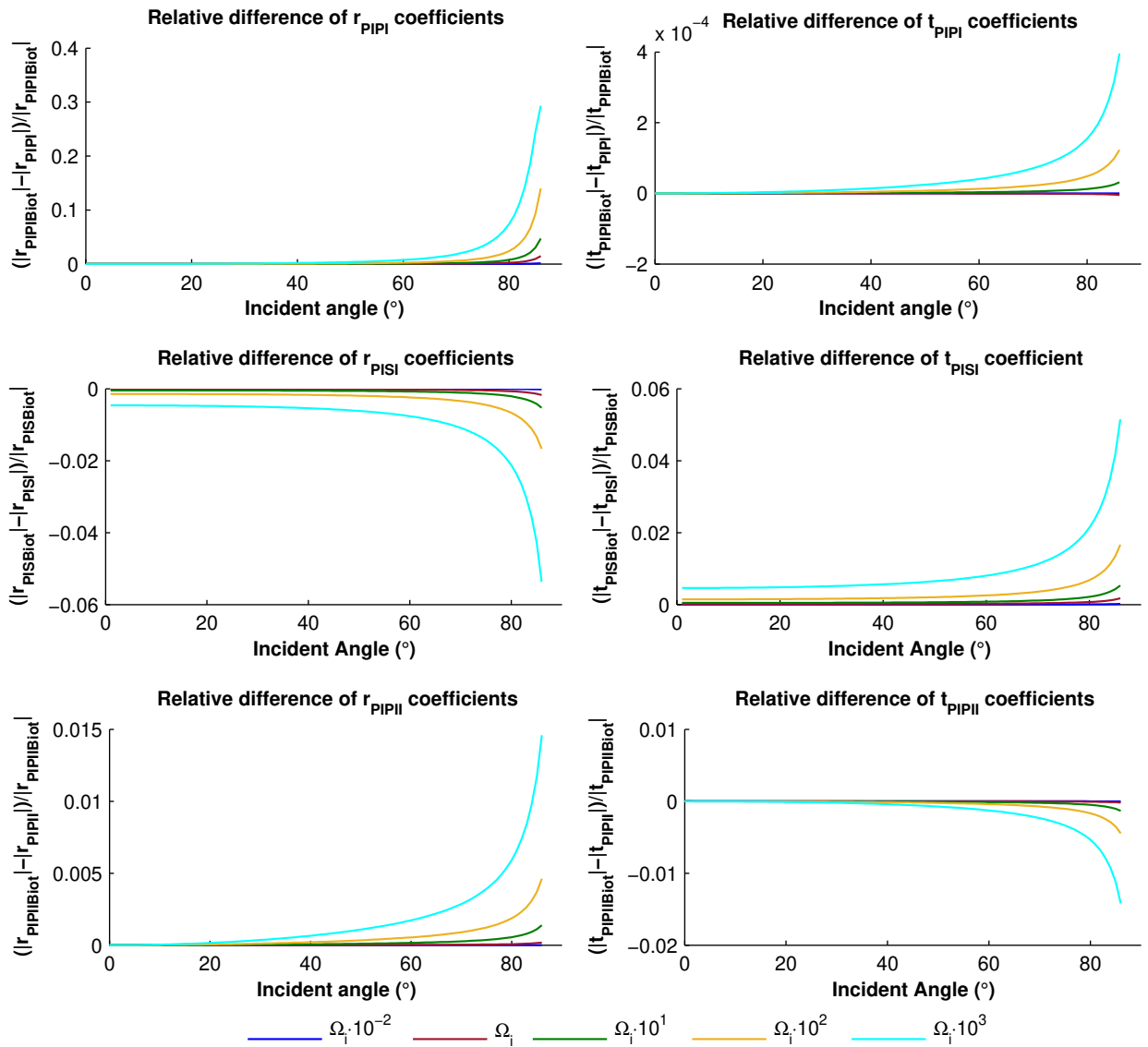
Figure 20. Relative difference of the reflection and transmission coefficients for a fast P-wave incident at an impermeable contact of two water-saturated sintered glass beads porous media with the same properties. The differences are plotted as a function of incident angle, and they are presented for the angular frequencies $\Omega_i \cdot 10^{-2}$ (blue), Ω_i (red), $\Omega_i \cdot 10^1$ (green), $\Omega_i \cdot 10^2$ (yellow), and $\Omega_i \cdot 10^3$ (cyan).

plitude, as in the SH case. However, its amplitude is reduced with increasing incident angle, and it is almost completely reflected above 80°. The fast and slow P-waves are generated at non-normal incident angles, and they have the same behavior in the reflected and transmitted waves. The fast-P waves have an amplitude in the order of 10^{-2} (0.02 in its maximum value), and the slow P-waves achieve amplitudes of 10^{-1} (0.3 in its maximum value). The reflected and transmitted slow S-waves show the same value as the SH case at the normal incident angle, but as the angle increases, the amplitude decrease.

The relative difference for these coefficients, Figure 21, shows that this effect also appears in the Biot theory. The viscous stress tensor causes a negative relative difference for the reflected fast and slow P-waves, whereas the rest of the scattered waves have a positive value. The reflected fast S-wave shows a significant difference at low incident angles, but at these angles, the amplitude of the reflected fast S-wave is small. Additionally, the magnitude of the relative difference for the reflected and transmitted fast P-waves is in the order of 10^{-2}.

For the case of a Berea sandstone in impermeable contact with a sintered glass beads porous medium, the reflection and transmission coefficients from an incident fast P-wave are in Figure 23. In this case, the amplitude of the scattered fast waves has a larger value than those in Figure 19 where the change in elastic properties does not exist. The reflected slow P- and slow S-waves have a smaller amplitude due to the larger tortuosity in the Berea sandstone. The transmitted slow waves have amplitudes in the same order as the scattered fast waves.

The contrast in properties of the media governs the amplitude of the scattered waves. Moreover, the fluid viscous stress tensor causes an effect that is observed in the relative differences shown in Figure 24. It shows a positive value for the transmitted fast P-wave and the reflected fast S- and slow P-waves. The reflected fast P-, transmitted fast S- and slow P-waves have a negative value. This effect increases with the incident angle. It is larger in the slow P-waves with a magnitude of 10^{-3}. The relative difference in the scattered fast waves is smaller. It has a magnitude of 10^{-4} for fast S-waves and 10^{-5} for fast P-waves.

For a fast S-wave incident at the impermeable contact of a Berea sandstone and a sintered glass beads porous medium, the reflection and transmission coefficients are in Figure 25. In this case, there are critical angles for the fast P-wave that span from 29.6° at $\omega = 1000\Omega_i^{(b)}$ to 29.7° at $\omega = 0.01\Omega_i^{(b)}$, and critical angles for the fast S-wave that span from 65.8° at $\omega = 1000\Omega_i^{(b)}$ to 76.3° at $\omega = 0.01\Omega_i^{(b)}$. The amplitude of the scattered fast waves has a larger value than in Figure 21 where the change in elastic properties does not exist. The reflected slow P- and slow S-waves have a smaller amplitude due to the large tortuosity in the Berea sandstone, and the transmitted slow waves have amplitudes in the same order as the scattered fast waves.
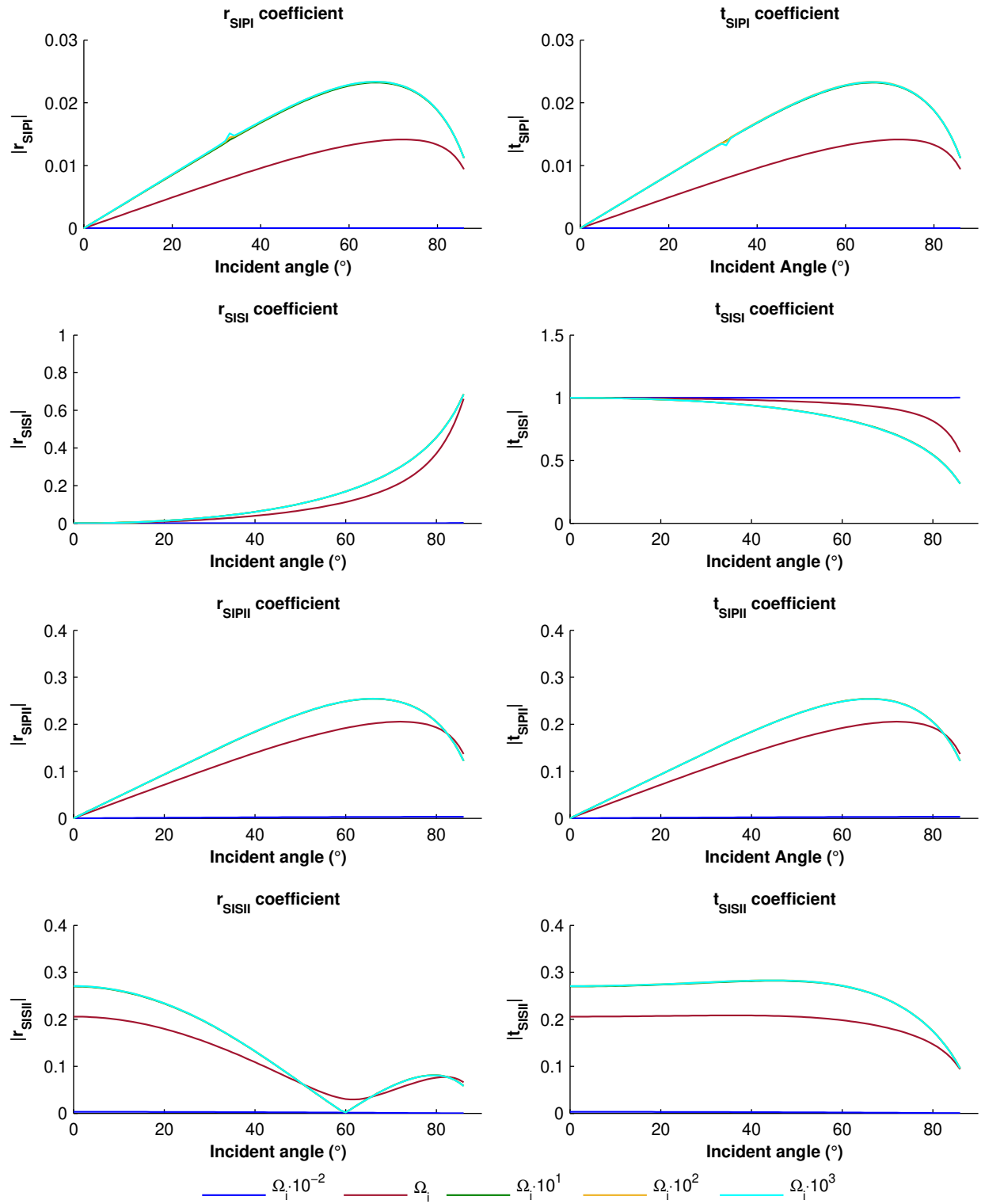
Figure 21. Amplitude of the reflection and transmission coefficients for a fast S-wave incident at an impermeable contact of two porous media with the same properties. The amplitudes are plotted as a function of incident angle, and they are presented for the angular frequencies $\Omega_i \cdot 10^{-2}$ (blue), Ω_i (red), $\Omega_i \cdot 10^1$ (green), $\Omega_i \cdot 10^2$ (yellow), and $\Omega_i \cdot 10^3$ (cyan).
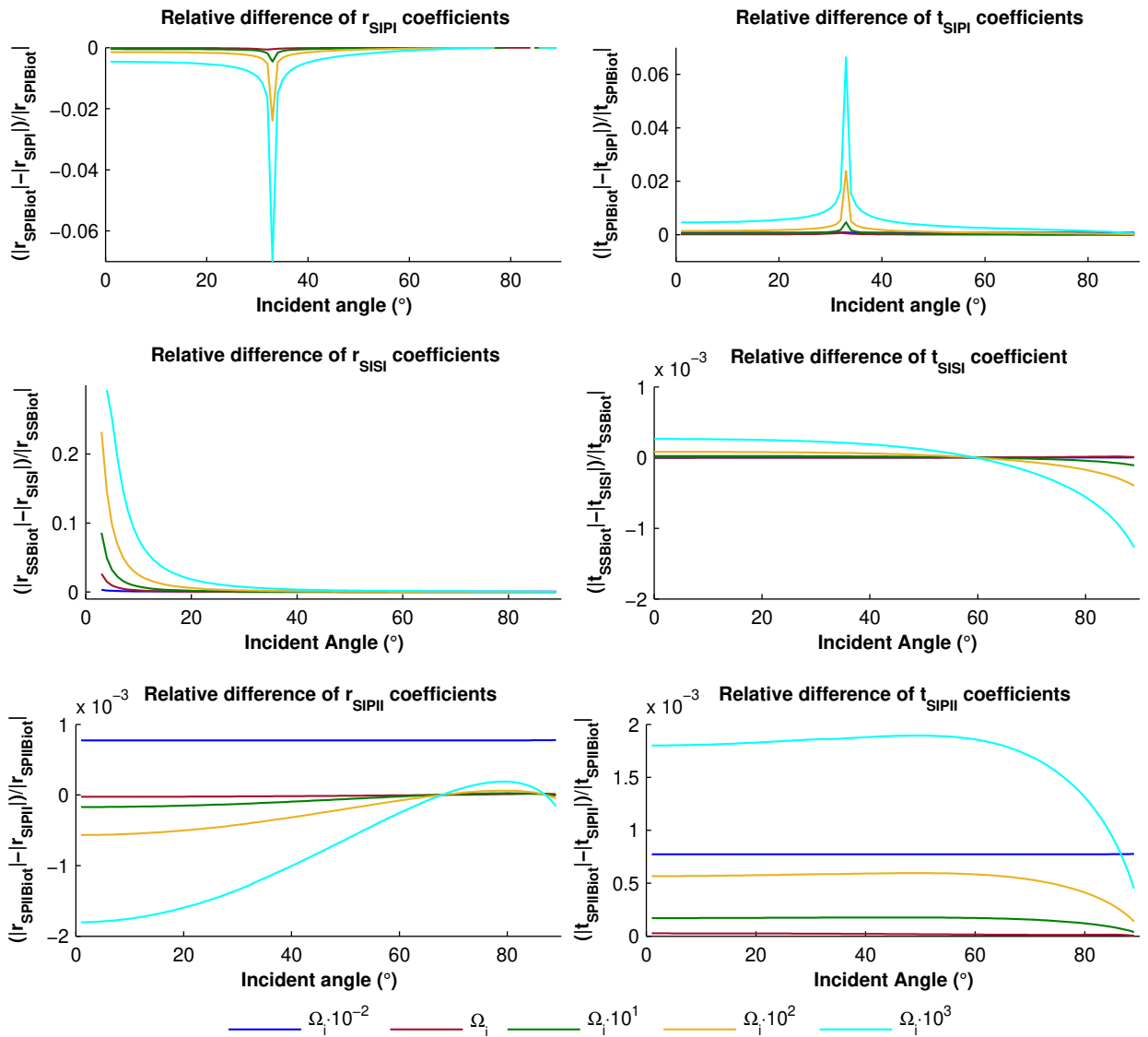
Figure 22. Relative difference of the reflection and transmission coefficients for a fast S-wave incident at an impermeable contact of two porous media with the same properties. The differences are plotted as a function of incident angle, and they are presented for the angular frequencies $\Omega_i \cdot 10^{-2}$ (blue), Ω_i (red), $\Omega_i \cdot 10^1$ (green), $\Omega_i \cdot 10^2$ (yellow), and $\Omega_i \cdot 10^3$ (cyan).

The fluid viscous stress tensor effects are observed in the relative differences shown in Figure 26. The transmitted fast P- and S-waves show a negative difference above their critical angle. However, above that angle, the waves are not transmitted anymore. For an incident fast S-wave, the fluid viscous stress tensor causes a change in amplitude of the same order in all scattered waves.
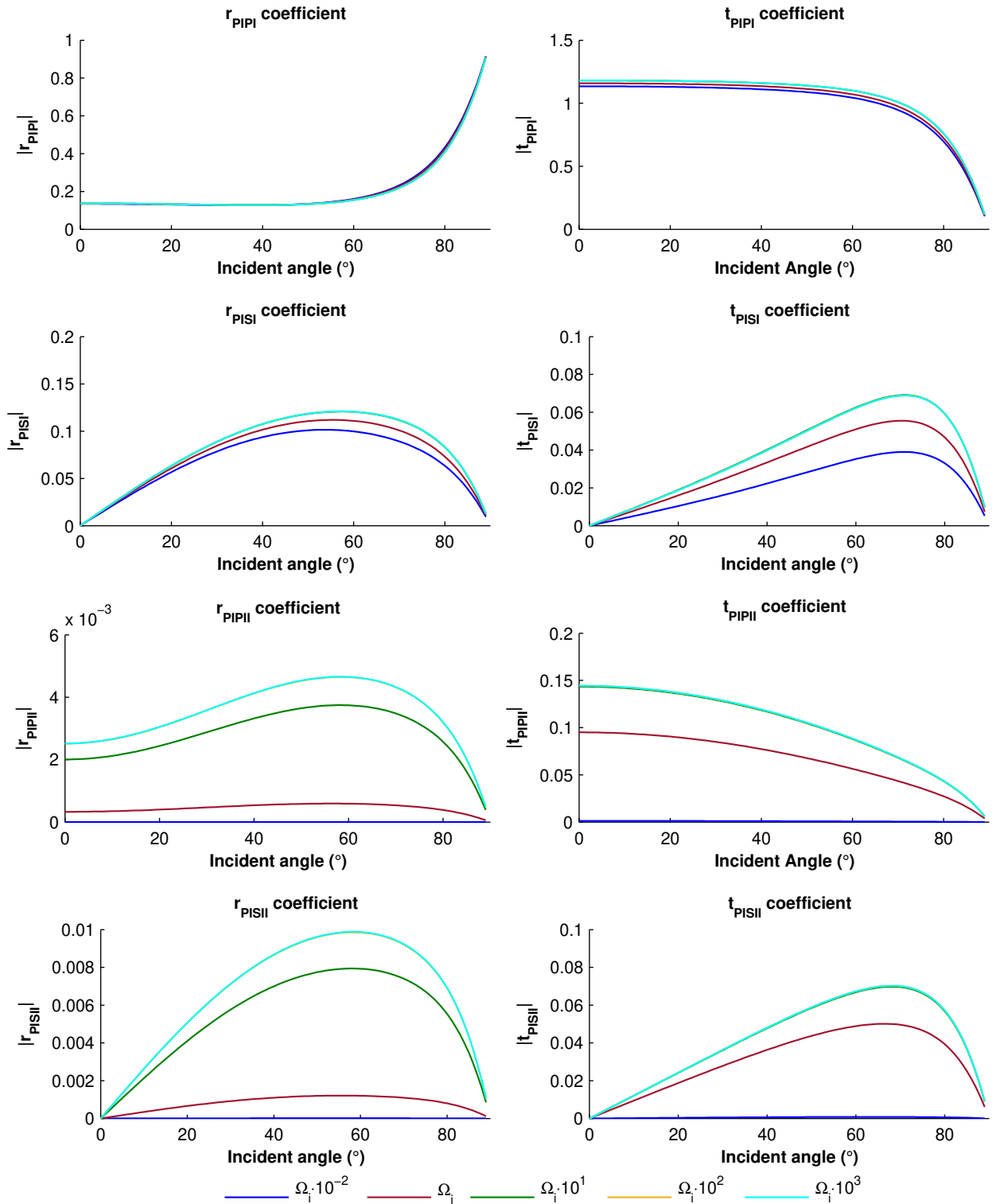
Figure 23. Amplitude of the reflection and transmission coefficients for a fast P-wave incident at an impermeable contact of two porous media. The upper-medium is a Berea sandstone, and the lower is a sintered glass beads porous medium. The amplitudes are plotted as a function of incident angle, and they are presented for the angular frequencies $\Omega_i \cdot 10^{-2}$ (blue), Ω_i (red), $\Omega_i \cdot 10^1$ (green), $\Omega_i \cdot 10^2$ (yellow), and $\Omega_i \cdot 10^3$ (cyan).
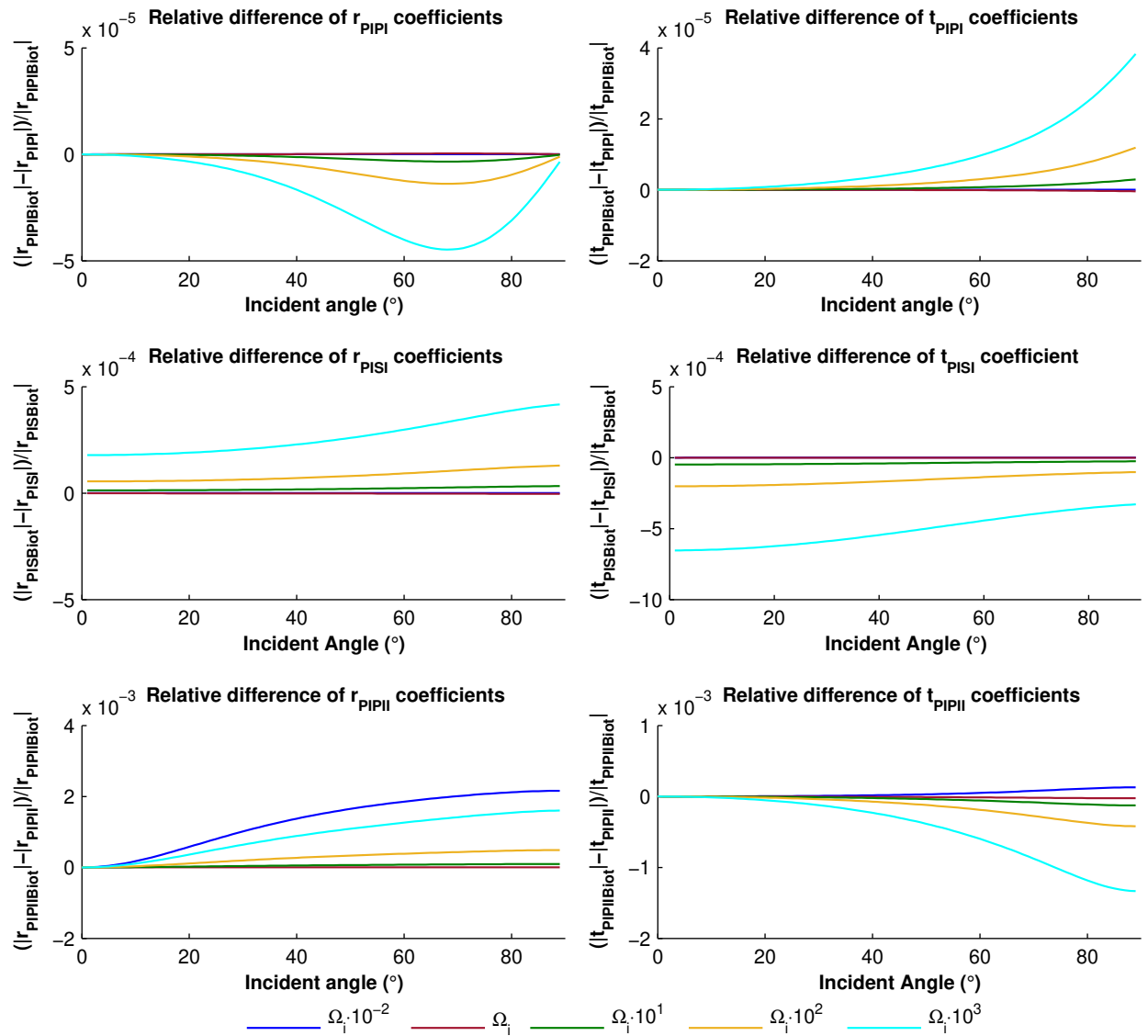
Figure 24. Relative difference of the reflection and transmission coefficients for a fast P-wave incident at an impermeable contact of two porous media. The upper-medium is a Berea sandstone, and the lower is a sintered glass beads porous medium. The differences are plotted as a function of incident angle, and they are presented for the angular frequencies $\Omega_i \cdot 10^{-2}$ (blue), Ω_i (red), $\Omega_i \cdot 10^1$ (green), $\Omega_i \cdot 10^2$ (yellow), and $\Omega_i \cdot 10^3$ (cyan).
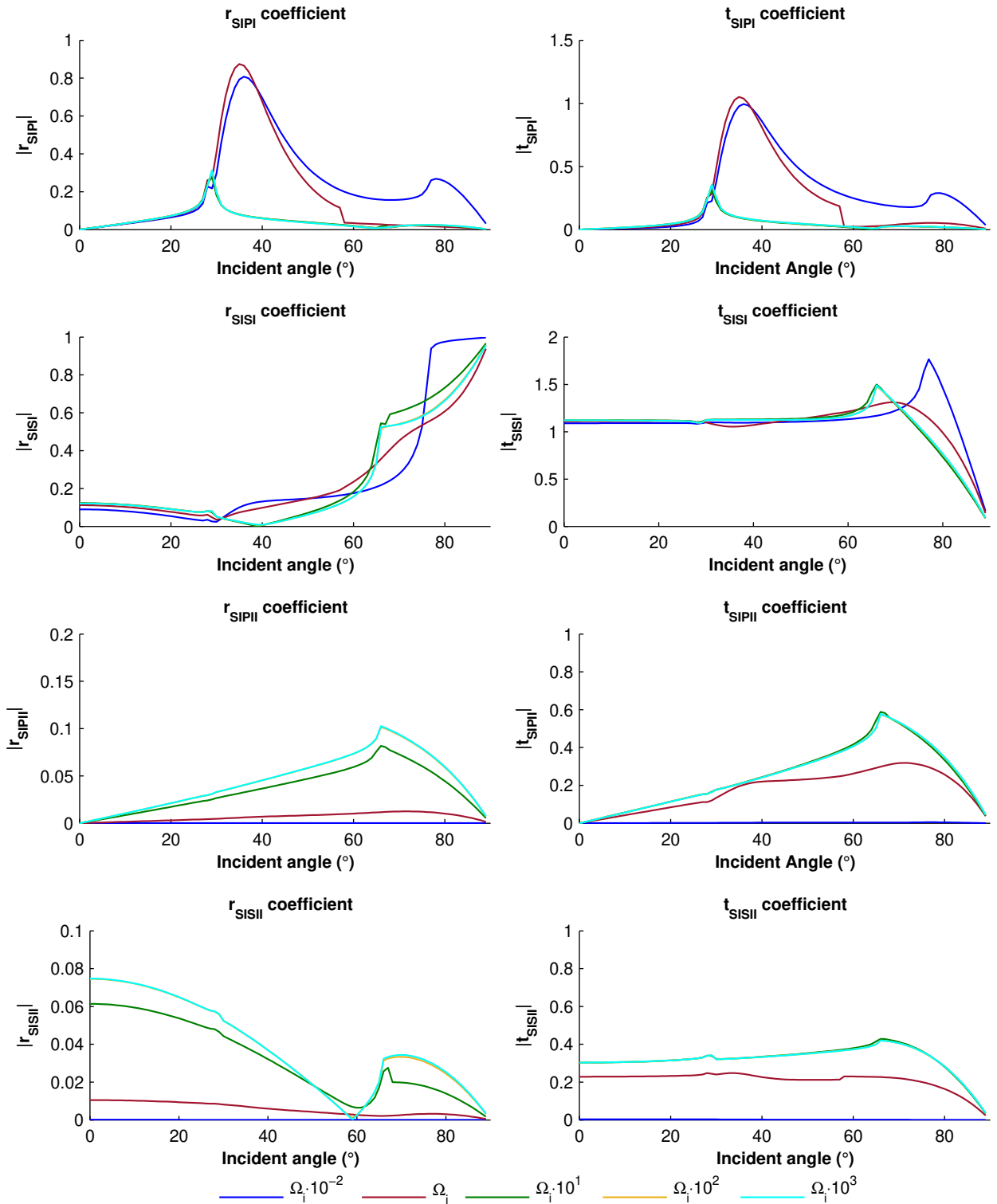
Figure 25. Amplitude of the reflection and transmission coefficients for a fast S-wave incident at an impermeable contact of two porous media. The upper-medium is a Berea sandstone, and the lower is a sintered glass beads porous medium. The amplitudes are plotted as a function of incident angle, and they are presented for the angular frequencies $\Omega_i \cdot 10^{-2}$ (blue), Ω_i (red), $\Omega_i \cdot 10^1$ (green), $\Omega_i \cdot 10^2$ (yellow), and $\Omega_i \cdot 10^3$ (cyan).
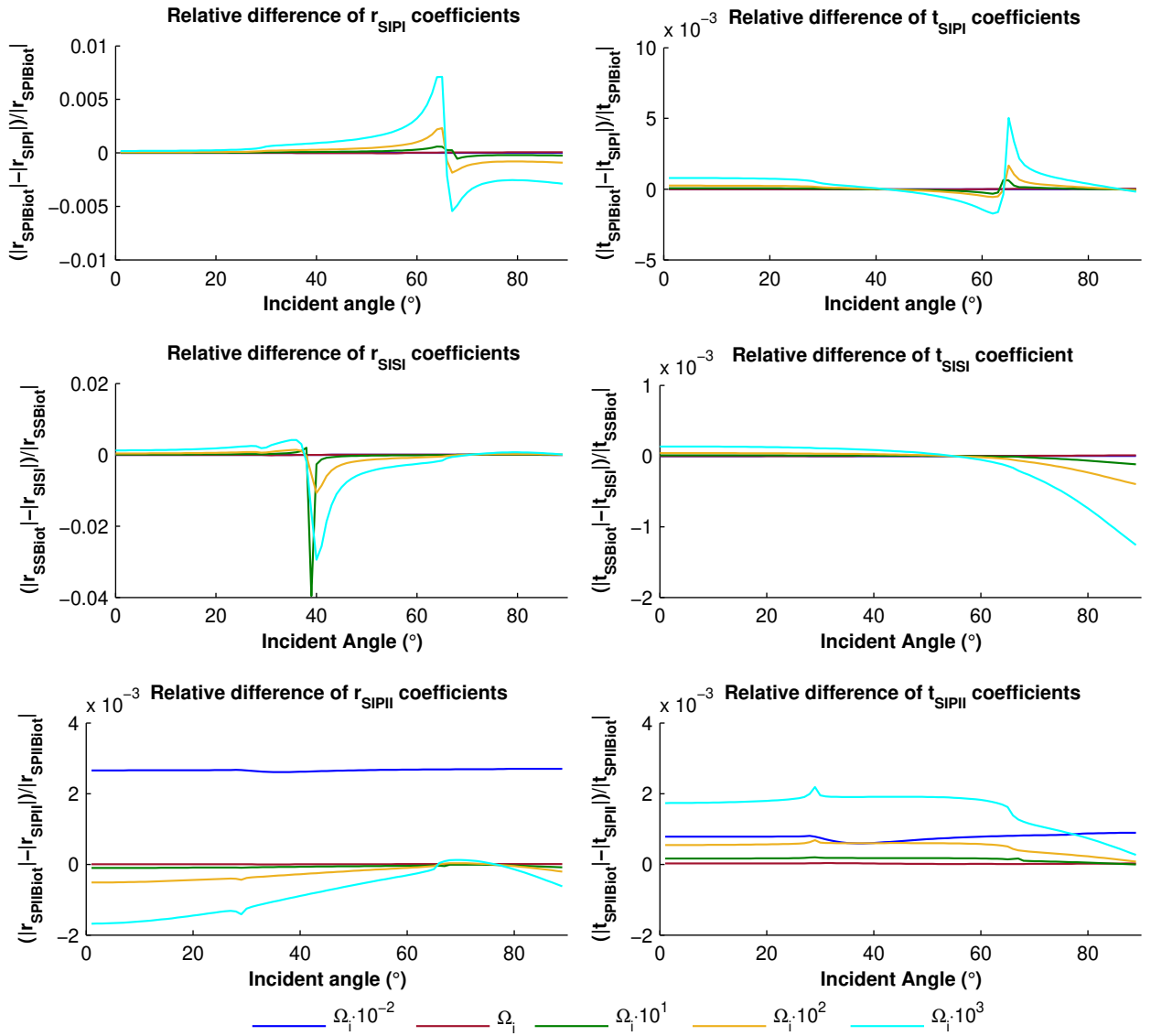
Figure 26. Relative difference of the reflection and transmission coefficients for a fast S-wave incident at an impermeable contact of two porous media. The upper-medium is a Berea sandstone, and the lower is a sintered glass beads porous medium. The differences are plotted as a function of incident angle, and they are presented for the angular frequencies $\Omega_i \cdot 10^{-2}$ (blue), Ω_i (red), $\Omega_i \cdot 10^1$ (green), $\Omega_i \cdot 10^2$ (yellow), and $\Omega_i \cdot 10^3$ (cyan).

5.3.2 Reflection and transmission coefficients for a permeable contact

For the case of incident P- and SV-waves in a permeable contact, the boundary conditions for establishing the reflection and transmission problem are the equations 49 to 54, 64, and 65. By substituting the displacements in terms of potentials (equations 32 and 33) and their respective stresses (equations 34 and 35) in the boundary conditions, the reflection and transmission system for the scattering matrix 129 is the same

equation 130, with the matrix $\mathbf{A}_{PSV}$ and $\mathbf{B}_{PSV}$ changed to

$\mathbf{A}_{PSV} =$

$$
\left(
\begin{array}{cccc}
\cos(\theta_{P_I}^{(\alpha)}) & \gamma_{\alpha_{II}}^{(\alpha)}\cos(\theta_{P_{II}}^{(\alpha)}) & -\sin(\theta_{S_I}^{(\alpha)}) & -\gamma_{\beta_{II}}^{(\alpha)}\sin(\theta_{S_{II}}^{(\alpha)}) \\
-\sin(\theta_{P_I}^{(\alpha)}) & -\gamma_{\alpha_{II}}^{(\alpha)}\sin(\theta_{P_{II}}^{(\alpha)}) & -\cos(\theta_{S_I}^{(\alpha)}) & -\gamma_{\beta_{II}}^{(\alpha)}\cos(\theta_{S_{II}}^{(\alpha)}) \\
-c_1^{(\alpha)}\cos(2\theta_{S_I}^{(\alpha)})-c_2^{(\alpha)}\cos(2\theta_{S_{II}}^{(\alpha)}) & -c_3^{(\alpha)}\cos(2\theta_{S_I}^{(\alpha)})-c_4^{(\alpha)}\cos(2\theta_{S_{II}}^{(\alpha)}) & Z_{\tau S_I}^{(\alpha)}\sin(2\theta_{S_I}^{(\alpha)}) & Z_{\tau S_{II}}^{(\alpha)}\sin(2\theta_{S_{II}}^{(\alpha)}) \\
d_1^{(\alpha)}\sin(2\theta_{P_I}^{(\alpha)}) & d_2^{(\alpha)}\sin(2\theta_{P_{II}}^{(\alpha)}) & Z_{\tau S_I}^{(\alpha)}\cos(2\theta_{S_I}^{(\alpha)}) & Z_{\tau S_{II}}^{(\alpha)}\cos(2\theta_{S_{II}}^{(\alpha)}) \\
\gamma_{\alpha_I}^{(\alpha)}\cos(\theta_{P_I}^{(\alpha)}) & \cos(\theta_{P_{II}}^{(\alpha)}) & -\gamma_{\beta_I}^{(\alpha)}\sin(\theta_{S_I}^{(\alpha)}) & -\sin(\theta_{S_{II}}^{(\alpha)}) \\
-c_5^{(\alpha)}\cos(2\theta_{S_I}^{(\alpha)})-c_6^{(\alpha)}\cos(2\theta_{S_{II}}^{(\alpha)}) & -c_7^{(\alpha)}\cos(2\theta_{S_I}^{(\alpha)})-c_8^{(\alpha)}\cos(2\theta_{S_{II}}^{(\alpha)}) & Z_{\tau S_I}^{(\alpha)}\sin(2\theta_{S_I}^{(\alpha)}) & Z_{\tau S_{II}}^{(\alpha)}\sin(2\theta_{S_{II}}^{(\alpha)}) \\
-\gamma_{\alpha_I}^{(\alpha)}\sin(\theta_{P_I}^{(\alpha)}) & -\sin(\theta_{P_{II}}^{(\alpha)}) & -\gamma_{\beta_I}^{(\alpha)}\cos(\theta_{S_I}^{(\alpha)}) & -\cos(\theta_{S_{II}}^{(\alpha)}) \\
d_3^{(\alpha)}\sin(2\theta_{P_I}^{(\alpha)}) & d_4^{(\alpha)}\sin(2\theta_{P_{II}}^{(\alpha)}) & Z_{\tau S_I}^{(\alpha)}\cos(2\theta_{S_I}^{(\alpha)}) & Z_{\tau S_{II}}^{(\alpha)}\cos(2\theta_{S_{II}}^{(\alpha)})
\end{array}
\right.
$$

$$
\left.
\begin{array}{cccc}
\cos(\theta_{P_I}^{(b)}) & \gamma_{\alpha_{II}}^{(b)}\cos(\theta_{P_{II}}^{(b)}) & \sin(\theta_{S_I}^{(b)}) & \gamma_{\beta_{II}}^{(b)}\sin(\theta_{S_{II}}^{(b)}) \\
\sin(\theta_{P_I}^{(b)}) & \gamma_{\alpha_{II}}^{(b)}\sin(\theta_{P_{II}}^{(b)}) & -\cos(\theta_{S_I}^{(b)}) & -\gamma_{\beta_{II}}^{(b)}\cos(\theta_{S_{II}}^{(b)}) \\
c_1^{(b)}\cos(2\theta_{S_I}^{(b)})+c_2^{(b)}\cos(2\theta_{S_{II}}^{(b)}) & c_3^{(b)}\cos(2\theta_{S_I}^{(b)})+c_4^{(b)}\cos(2\theta_{S_{II}}^{(b)}) & Z_{\tau S_I}^{(b)}\sin(2\theta_{S_I}^{(b)}) & Z_{\tau S_{II}}^{(b)}\sin(2\theta_{S_{II}}^{(b)}) \\
d_1^{(b)}\sin(2\theta_{P_I}^{(b)}) & d_2^{(b)}\sin(2\theta_{P_{II}}^{(b)}) & -Z_{\tau S_I}^{(b)}\cos(2\theta_{S_I}^{(b)}) & -Z_{\tau S_{II}}^{(b)}\cos(2\theta_{S_{II}}^{(b)}) \\
\gamma_{\alpha_I}^{(b)}\cos(\theta_{P_I}^{(b)}) & \cos(\theta_{P_{II}}^{(b)}) & \gamma_{\beta_I}^{(b)}\sin(\theta_{S_I}^{(b)}) & \sin(\theta_{S_{II}}^{(b)}) \\
c_5^{(b)}\cos(2\theta_{S_I}^{(b)})+c_6^{(b)}\cos(2\theta_{S_{II}}^{(b)}) & c_7^{(b)}\cos(2\theta_{S_I}^{(b)})+c_8^{(b)}\cos(2\theta_{S_{II}}^{(b)}) & Z_{\tau S_I}^{(b)}\sin(2\theta_{S_I}^{(b)}) & Z_{\tau S_{II}}^{(b)}\sin(2\theta_{S_{II}}^{(b)}) \\
\gamma_{\alpha_I}^{(b)}\sin(\theta_{P_I}^{(b)}) & \sin(\theta_{P_{II}}^{(b)}) & -\gamma_{\beta_I}^{(b)}\cos(\theta_{S_I}^{(b)}) & -\cos(\theta_{S_{II}}^{(b)}) \\
d_3^{(b)}\sin(2\theta_{P_I}^{(b)}) & d_4^{(b)}\sin(2\theta_{P_{II}}^{(b)}) & -Z_{\tau S_I}^{(b)}\cos(2\theta_{S_I}^{(b)}) & -Z_{\tau S_{II}}^{(b)}\cos(2\theta_{S_{II}}^{(b)})
\end{array}
\right),
$$

(133)

and

$$\mathbf{B}_{\text{PSV}} =$$

$$
\left(
\begin{array}{cccc}
\cos(\theta_{P_\text{I}}^{(a)}) & \gamma_{\alpha_\text{II}}^{(a)}\cos(\theta_{P_\text{II}}^{(a)}) & \sin(\theta_{S_\text{I}}^{(a)}) & \gamma_{\beta_\text{II}}^{(a)}\sin(\theta_{S_\text{II}}^{(a)}) \\
\sin(\theta_{P_\text{I}}^{(a)}) & \gamma_{\alpha_\text{II}}^{(a)}\sin(\theta_{P_\text{II}}^{(a)}) & -\cos(\theta_{S_\text{I}}^{(a)}) & -\gamma_{\beta_\text{II}}^{(a)}\cos(\theta_{S_\text{II}}^{(a)}) \\
c_1^{(a)}\cos(2\theta_{S_\text{I}}^{(a)})+c_2^{(a)}\cos(2\theta_{S_\text{II}}^{(a)}) & c_3^{(a)}\cos(2\theta_{S_\text{I}}^{(a)})+c_4^{(a)}\cos(2\theta_{S_\text{II}}^{(a)}) & Z_{\tau S_\text{I}}^{(a)}\sin(2\theta_{S_\text{I}}^{(a)}) & Z_{\tau S_\text{II}}^{(a)}\sin(2\theta_{S_\text{II}}^{(a)}) \\
d_1^{(a)}\sin(2\theta_{P_\text{I}}^{(a)}) & d_2^{(a)}\sin(2\theta_{P_\text{II}}^{(a)}) & -Z_{\tau S_\text{I}}^{(a)}\cos(2\theta_{S_\text{I}}^{(a)}) & -Z_{\tau S_\text{II}}^{(a)}\cos(2\theta_{S_\text{II}}^{(a)}) \\
\gamma_{\alpha_\text{I}}^{(a)}\cos(\theta_{P_\text{I}}^{(a)}) & \cos(\theta_{P_\text{II}}^{(a)}) & \gamma_{\beta_\text{I}}^{(a)}\sin(\theta_{S_\text{I}}^{(a)}) & \sin(\theta_{S_\text{II}}^{(a)}) \\
c_5^{(a)}\cos(2\theta_{S_\text{I}}^{(a)})+c_6^{(a)}\cos(2\theta_{S_\text{II}}^{(a)}) & c_7^{(a)}\cos(2\theta_{S_\text{I}}^{(a)})+c_8^{(a)}\cos(2\theta_{S_\text{II}}^{(a)}) & Z_{\tau S_\text{I}}^{(a)}\sin(2\theta_{S_\text{I}}^{(a)}) & Z_{\tau S_\text{II}}^{(a)}\sin(2\theta_{S_\text{II}}^{(a)}) \\
\gamma_{\alpha_\text{I}}^{(a)}\sin(\theta_{P_\text{I}}^{(a)}) & \sin(\theta_{P_\text{II}}^{(a)}) & -\gamma_{\beta_\text{I}}^{(a)}\cos(\theta_{S_\text{I}}^{(a)}) & -\cos(\theta_{S_\text{II}}^{(a)}) \\
d_3^{(a)}\sin(2\theta_{P_\text{I}}^{(a)}) & d_4^{(a)}\sin(2\theta_{P_\text{II}}^{(a)}) & -Z_{\tau S_\text{I}}^{(a)}\cos(2\theta_{S_\text{I}}^{(a)}) & -Z_{\tau S_\text{II}}^{(a)}\cos(2\theta_{S_\text{II}}^{(a)})
\end{array}
\right.
$$

$$
\left.
\begin{array}{cccc}
\cos(\theta_{P_\text{I}}^{(b)}) & \gamma_{\alpha_\text{II}}^{(b)}\cos(\theta_{P_\text{II}}^{(b)}) & -\sin(\theta_{S_\text{I}}^{(b)}) & -\gamma_{\beta_\text{II}}^{(b)}\sin(\theta_{S_\text{II}}^{(b)}) \\
-\sin(\theta_{P_\text{I}}^{(b)}) & -\gamma_{\alpha_\text{II}}^{(b)}\sin(\theta_{P_\text{II}}^{(b)}) & -\cos(\theta_{S_\text{I}}^{(b)}) & -\gamma_{\beta_\text{II}}^{(b)}\cos(\theta_{S_\text{II}}^{(b)}) \\
-c_1^{(b)}\cos(2\theta_{S_\text{I}}^{(b)})-c_2^{(b)}\cos(2\theta_{S_\text{II}}^{(b)}) & -c_3^{(b)}\cos(2\theta_{S_\text{I}}^{(b)})-c_4^{(b)}\cos(2\theta_{S_\text{II}}^{(b)}) & Z_{\tau S_\text{I}}^{(b)}\sin(2\theta_{S_\text{I}}^{(b)}) & Z_{\tau S_\text{II}}^{(b)}\sin(2\theta_{S_\text{II}}^{(b)}) \\
d_1^{(b)}\sin(2\theta_{P_\text{I}}^{(b)}) & d_2^{(b)}\sin(2\theta_{P_\text{II}}^{(b)}) & Z_{\tau S_\text{I}}^{(b)}\cos(2\theta_{S_\text{I}}^{(b)}) & Z_{\tau S_\text{II}}^{(b)}\cos(2\theta_{S_\text{II}}^{(b)}) \\
\gamma_{\alpha_\text{I}}^{(b)}\cos(\theta_{P_\text{I}}^{(b)}) & \cos(\theta_{P_\text{II}}^{(b)}) & -\gamma_{\beta_\text{I}}^{(b)}\sin(\theta_{S_\text{I}}^{(b)}) & -\sin(\theta_{S_\text{II}}^{(b)}) \\
-c_5^{(b)}\cos(2\theta_{S_\text{I}}^{(b)})-c_6^{(b)}\cos(2\theta_{S_\text{II}}^{(b)}) & -c_7^{(b)}\cos(2\theta_{S_\text{I}}^{(b)})-c_8^{(b)}\cos(2\theta_{S_\text{II}}^{(b)}) & Z_{\tau S_\text{I}}^{(b)}\sin(2\theta_{S_\text{I}}^{(b)}) & Z_{\tau S_\text{II}}^{(b)}\sin(2\theta_{S_\text{II}}^{(b)}) \\
-\gamma_{\alpha_\text{I}}^{(b)}\sin(\theta_{P_\text{I}}^{(b)}) & -\sin(\theta_{P_\text{II}}^{(b)}) & -\gamma_{\beta_\text{I}}^{(b)}\cos(\theta_{S_\text{I}}^{(b)}) & -\cos(\theta_{S_\text{II}}^{(b)}) \\
d_3^{(b)}\sin(2\theta_{P_\text{I}}^{(b)}) & d_4^{(b)}\sin(2\theta_{P_\text{II}}^{(b)}) & Z_{\tau S_\text{I}}^{(b)}\cos(2\theta_{S_\text{I}}^{(b)}) & Z_{\tau S_\text{II}}^{(b)}\cos(2\theta_{S_\text{II}}^{(b)})
\end{array}
\right).
$$

$$(134)$$

In the limit to the Biot theory, the system is determined by the boundary conditions 49 to 54. As in the impermeable contact, the reflection and transmission problem can be derived from equations 133 and 134 by removing, in both matrices, columns four and eight, which are related to the reflected and transmitted slow S-waves, respectively. Also, rows seven and eight have to be removed. These rows correspond to the continuity of fluid motion and fluid stresses in the tangential direction, which the Biot theory does not define.

5.3.2.1 Effect of the fluid viscous stress tensor

To examine the impact of the fluid viscous stress tensor in a permeable contact, the numerical solution of the system 130 is computed by the Gauss-Jordan elimination method, as in the impermeable case. The pseudocode for this solution is described in section B.2 of Appendix B, too.

As in the case of SH-waves, the fluid viscous stress tensor also affects the scattered waves in a permeable contact. Figure 27 shows the reflection and transmission coefficients for an incident fast P-wave traveling across the permeable contact of the Berea sandstone and the sintered glass beads porous medium. The amplitude of the scattered fast waves shows the same behavior that the scattered waves in an impermeable contact (Figure 23) with a smaller magnitude. However, such a difference is so small that is not appreciable. The reflected slow waves are one order of magnitude larger than that in the impermeable case, whereas the transmitted slow waves have almost the same values.

The relative differences are presented in Figure 28. Herein, the difference of the scattered fast waves has the same magnitude as that in the case of the impermeable contact (Figure 24). The relative differences for the reflected and transmitted slow P-wave are one order of magnitude smaller.

For a fast S-wave incident at the permeable contact of a Berea sandstone and a sintered glass beads porous medium, the reflection and transmission coefficients are in Figure 29. In the high-frequency regime, the amplitude of the reflected and transmitted fast S-waves is smaller than that of the scattered fast S-waves in an impermeable contact (Figure 25). The reflected and transmitted fast P-waves are also smaller, but their difference is not significant enough to be observed in the plots. The reflected slow P- and S-waves show different behavior and a larger amplitude than the corresponding waves in the impermeable case. The transmitted slow P and S-waves show the same behavior with a smaller amplitude.
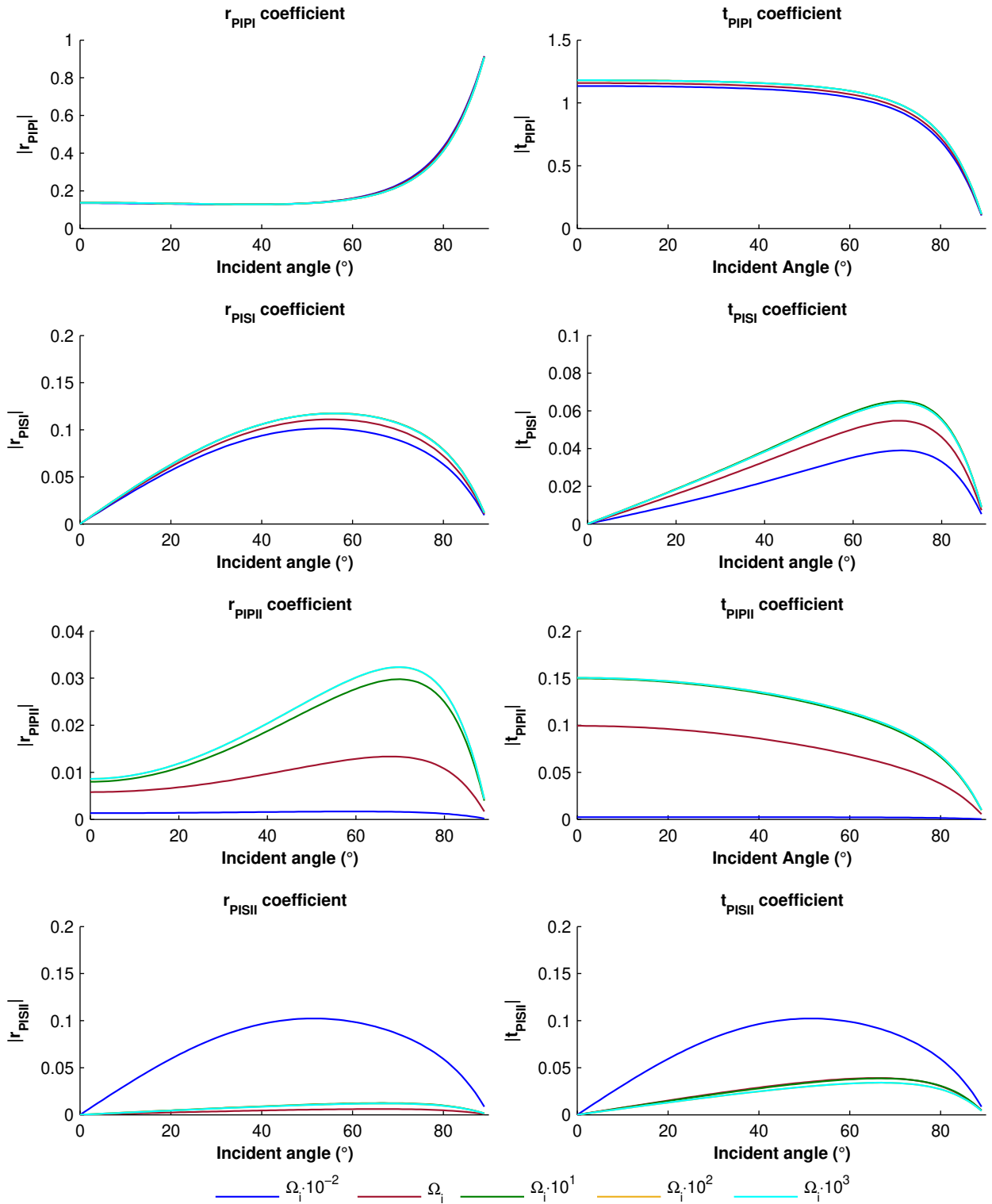
Figure 27. Amplitude of the reflection and transmission coefficients for a fast P-wave incident at a permeable contact of two porous media. The upper-medium is a Berea sandstone, and the lower is a sintered glass beads porous medium. The amplitudes are plotted as a function of incident angle, and they are presented for the angular frequencies $\Omega_i \cdot 10^{-2}$ (blue), Ω_i (red), $\Omega_i \cdot 10^1$ (green), $\Omega_i \cdot 10^2$ (yellow), and $\Omega_i \cdot 10^3$ (cyan).
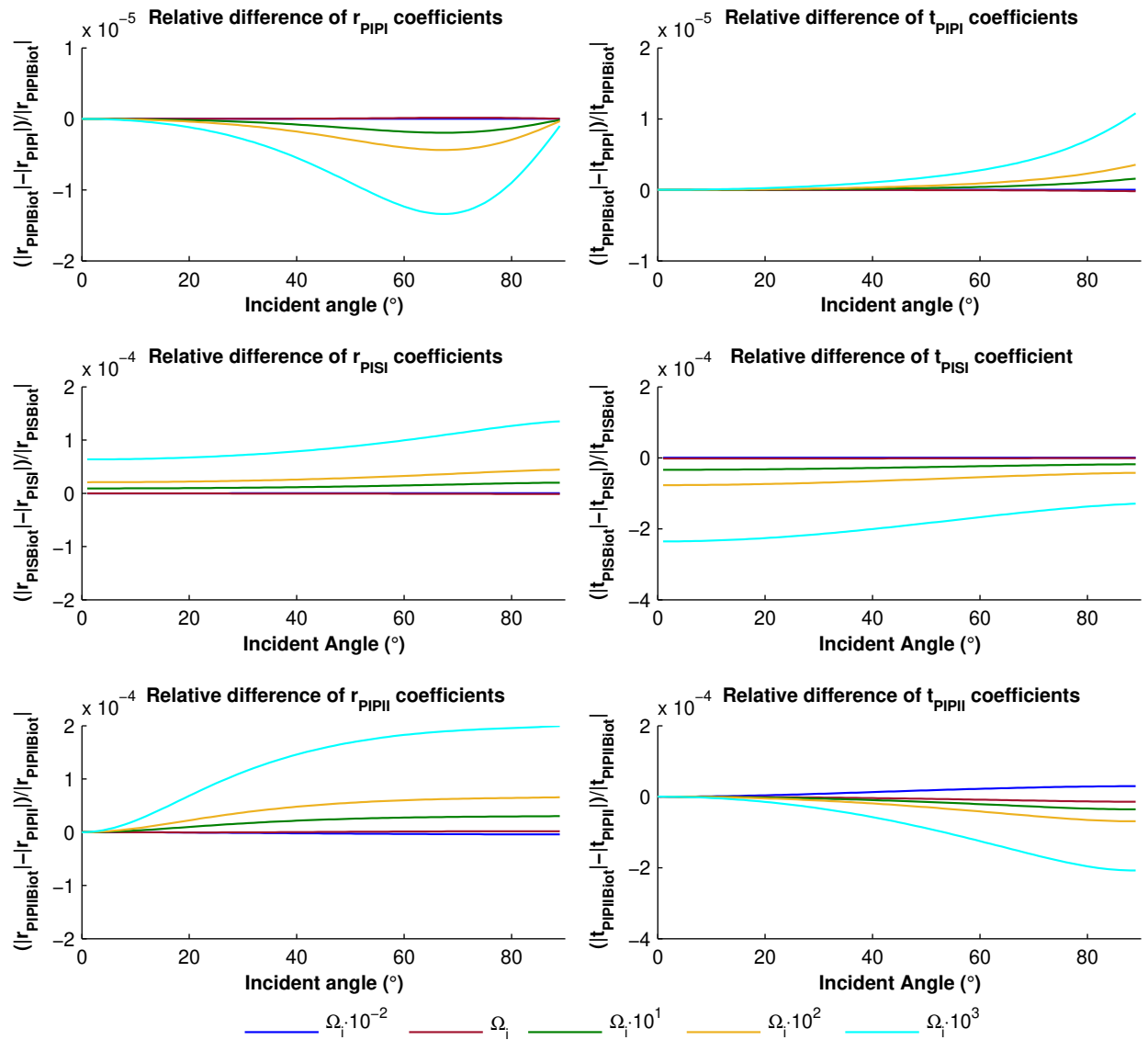
Figure 28. Relative difference of the reflection and transmission coefficients for a fast P-wave incident at a permeable contact of two porous media. The upper-medium is a Berea sandstone, and the lower is a sintered glass beads porous medium. The differences are plotted as a function of incident angle, and they are presented for the angular frequencies $\Omega_i \cdot 10^{-2}$ (blue), Ω_i (red), $\Omega_i \cdot 10^1$ (green), $\Omega_i \cdot 10^2$ (yellow), and $\Omega_i \cdot 10^3$ (cyan).

The relative differences are presented in Figure 30. Herein, the difference of the reflected fast P-wave is one order of magnitude smaller than that in the case of the impermeable contact (Figure 26). The difference of the transmitted fast P-wave shows a similar behavior. The difference for the reflected and transmitted fast S-waves are one order of magnitude smaller. In contrast, the relative difference for the reflected and transmitted slow P-waves are in the same order of magnitude.
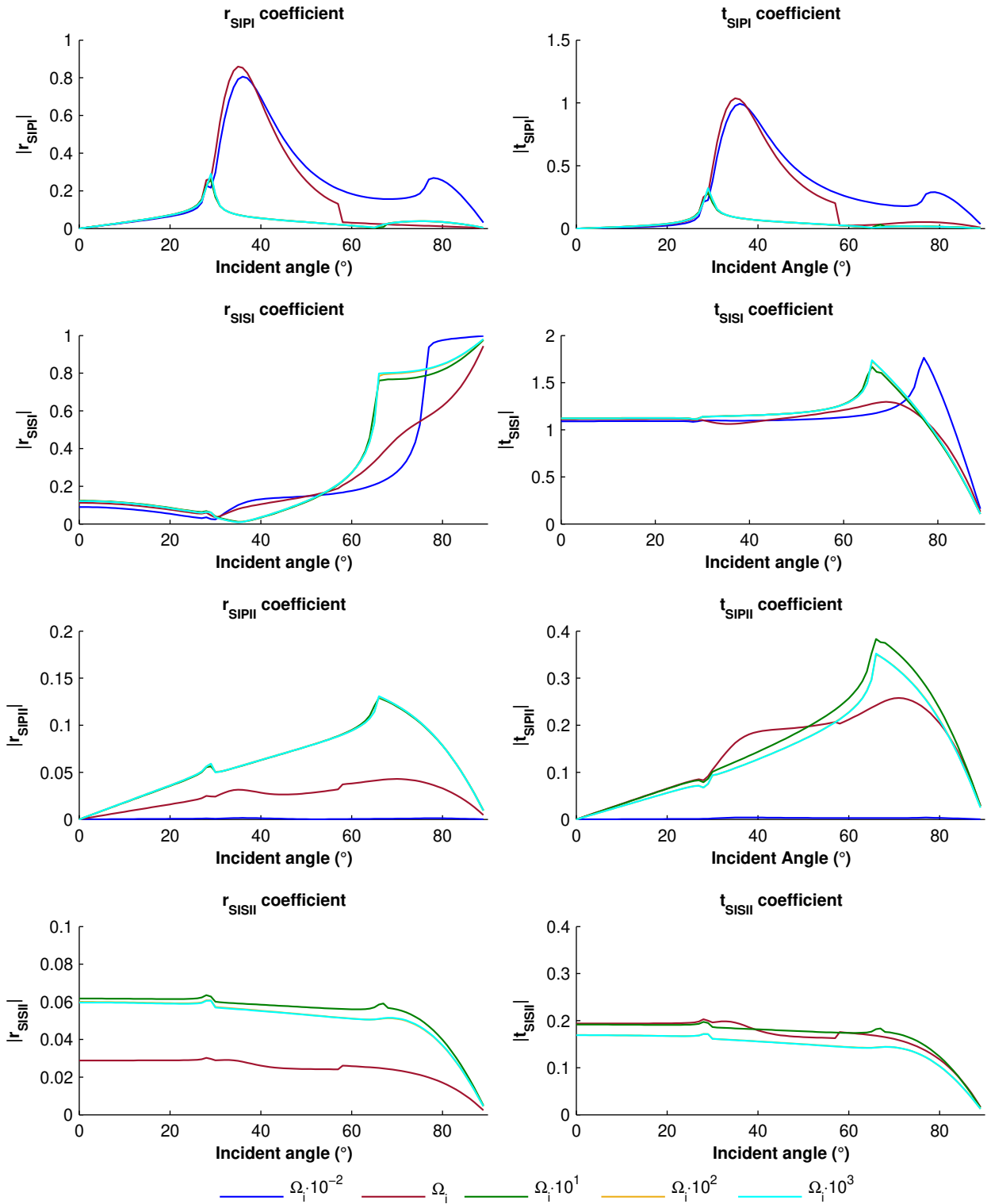
Figure 29. Amplitude of the reflection and transmission coefficients for a fast S-wave incident at a permeable contact of two porous media. The upper-medium is a Berea sandstone, and the lower is a sintered glass beads porous medium. The amplitudes are plotted as a function of incident angle, and they are presented for the angular frequencies $\Omega_i \cdot 10^{-2}$ (blue), Ω_i (red), $\Omega_i \cdot 10^1$ (green), $\Omega_i \cdot 10^2$ (yellow), and $\Omega_i \cdot 10^3$ (cyan).
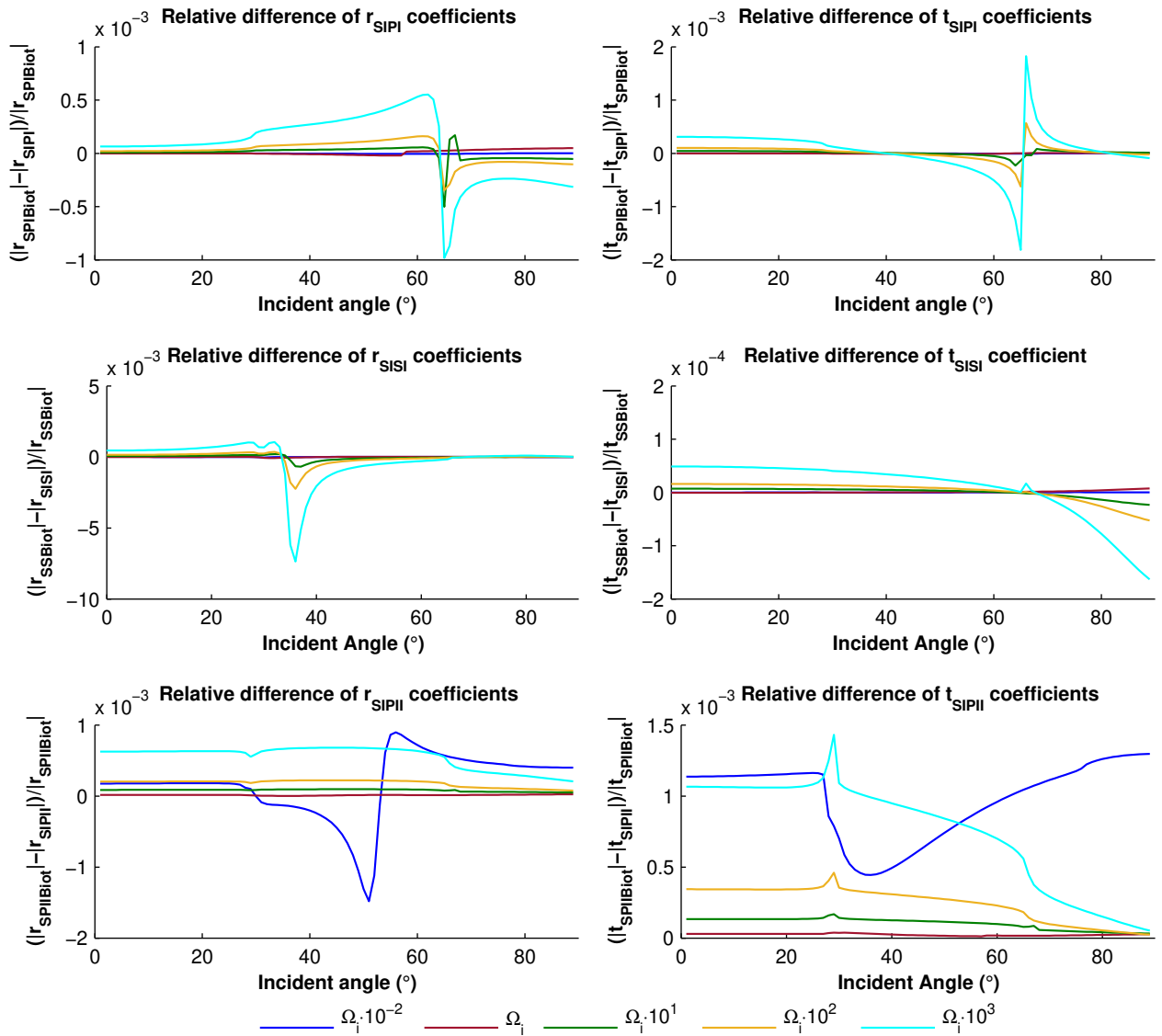
Figure 30. Relative difference of the reflection and transmission coefficients for a fast S-wave incident at a permeable contact of two porous media. The upper-medium is a Berea sandstone, and the lower is a sintered glass beads porous medium. The differences are plotted as a function of incident angle, and they are presented for the angular frequencies $\Omega_i \cdot 10^{-2}$ (blue), Ω_i (red), $\Omega_i \cdot 10^1$ (green), $\Omega_i \cdot 10^2$ (yellow), and $\Omega_i \cdot 10^3$ (cyan).

Chapter 6.   Conversion scattering in a stack of plane poroelastic layers

This chapter analyzes the role of the fluid viscous stress tensor in a stack of planar poroelastic layers. For that, I consider a down-going fast P- or S-wave incident at the upper layer and travels across a stack of N plane layers. Both permeable and impermeable cases are considered. The wave propagation across a stack of layers is solved by the reflectivity method.

As in the case of single contact, the scattering is generated by various factors different from the fluid viscous stress tensor. However, the relative difference of the solution in the Biot and dCS theories (equation 97) allow us to separate the effect of the fluid viscous stress tensor.

Section 6.1 presents the Kennett reflectivity method (Kennett, 1983) extended for poroelastic layers. After that, the conversion scattering for the case of an incident fast SH-wave is analyzed in section 6.2. Then, section 6.3 presents the analysis of conversion scattering for incident P- and SV-waves.

6.1   The reflectivity method for a stack of plane poroelastic layers

To analyze the wave propagation across a layering medium, let us consider an incident down-going fast P- or S- wave coming from the top of a stack of N plane layers in-between of two porous half-spaces (Figure 31). In the lower half-space only down-going waves exist, and the scattered waves in the upper half-space propagate in the up-going direction. Although both reflected and transmitted waves are generated across the stack, I focus on analyzing transmitted waves at the lower half-space because they travel once across the contacts.

The wave propagation across the layered medium is semi-analytically solved by Kennett's reflectivity method (Kennett, 1983). It uses the medium geometry, which is homogeneous in the horizontal direction, to solve the wave propagation in the frequency-wavenumber ($\omega - k$) domain by applying a double Fourier transform. In such

a domain, the governing equations for poroelastic wave propagation are represented as a system of first-order equations.
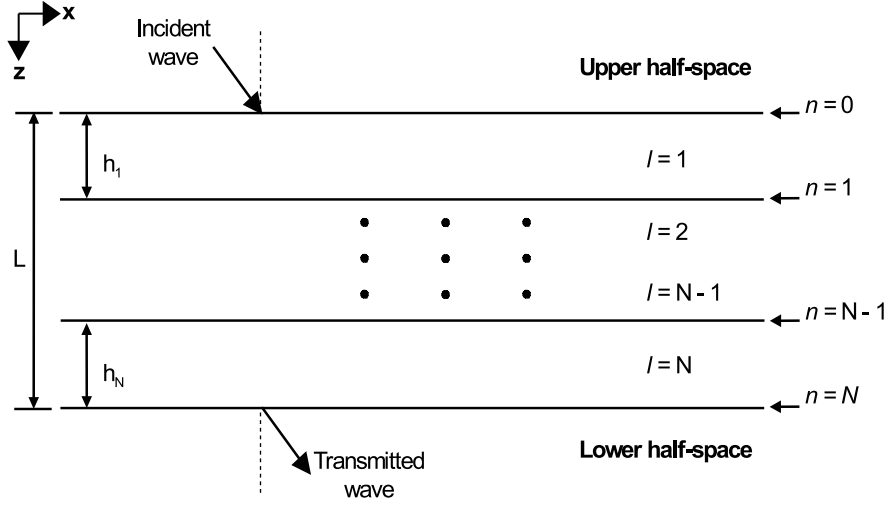
Figure 31. Conversion scattering in a stack of N plane poroelastic layer in between of two porous half-spaces. The terms l and n are the numbers of layers and contacts, respectively. The term h is the layer thickness, and L is the total length of the stack.

6.1.1 Formulation for SH-waves in frequency-wavenumber domain

The governing equations for SH-waves in the $\omega - k$ domain are

$$
\frac{\partial}{\partial z}\begin{pmatrix} \mathbf{u}_y \\ \boldsymbol{\Omega}^{-1}\boldsymbol{\rho}^{-1}\boldsymbol{\tau}_{yz} \end{pmatrix} = \underbrace{\begin{pmatrix} \mathbf{0} & \boldsymbol{\beta}^{-1} \\ (\boldsymbol{\beta}k^2 - \omega^2\mathbf{I}) & \mathbf{0} \end{pmatrix}}_{\boldsymbol{\alpha}_{\mathrm{SH}}} \underbrace{\begin{pmatrix} \mathbf{u}_y \\ \boldsymbol{\Omega}^{-1}\boldsymbol{\rho}^{-1}\boldsymbol{\tau}_{yz} \end{pmatrix}}_{\mathbf{b}_{\mathrm{SH}}}. \tag{135}
$$

By applying the transformation $\mathbf{b}_{\mathrm{SH}} = \mathbf{D}_{\mathrm{SH}}\mathbf{v}_{\mathrm{SH}}$, where $\mathbf{D}_{\mathrm{SH}}$ is the eigenvector matrix of $\boldsymbol{\alpha}_{\mathrm{SH}}$, the system 135 is diagonalized. For a homogeneous medium, it has the solution

$$
\mathbf{v}_{\mathrm{SH}} = \left(\underbrace{e^{-i\omega z q_{\beta_{\mathrm{I}}}} b_{\mathrm{I}}^-}_{S_{\mathrm{I}}^-}, \quad \underbrace{e^{-i\omega z q_{\beta_{\mathrm{II}}}} b_{\mathrm{II}}^-}_{S_{\mathrm{II}}^-}, \quad \underbrace{e^{i\omega z q_{\beta_{\mathrm{I}}}} b_{\mathrm{I}}^+}_{S_{\mathrm{I}}^+}, \quad \underbrace{e^{i\omega z q_{\beta_{\mathrm{II}}}} b_{\mathrm{II}}^+}_{S_{\mathrm{II}}^+} \right)^T. \tag{136}
$$

The elements S_{I}^- and S_{II}^- are, respectively, the up-going fast and slow S-waves, and S_{I}^+ and S_{II}^+ are the down-going fast and slow S-waves, respectively.

6.1.2 Formulation for P- and SV-waves in frequency-wavenumber domain

For the case of P- and SV-waves, the governing equations are the 8 × 8 system

$$
\frac{\partial}{\partial z}
\begin{pmatrix}
\mathbf{u}_z \\
\mathbf{u}_x \\
\boldsymbol{\Omega}^{-1}\boldsymbol{\rho}^{-1}\boldsymbol{\tau}_{zz} \\
\boldsymbol{\Omega}^{-1}\boldsymbol{\rho}^{-1}\boldsymbol{\tau}_{xz}
\end{pmatrix}
=
$$

$$
\underbrace{
\begin{pmatrix}
0 & -ik\left(\mathbf{I}-2\boldsymbol{\alpha}^{-1}\boldsymbol{\beta}\right) & \boldsymbol{\alpha}^{-1} & 0 \\
-ik\mathbf{I} & 0 & 0 & \boldsymbol{\beta}^{-1} \\
-\omega^2\mathbf{I} & 0 & 0 & -ik\mathbf{I} \\
0 & 4k^2\boldsymbol{\beta}\left(\mathbf{I}-\boldsymbol{\alpha}^{-1}\boldsymbol{\beta}\right)-\omega^2\mathbf{I} & -ik\left(\mathbf{I}-2\boldsymbol{\beta}\boldsymbol{\alpha}^{-1}\right) & 0
\end{pmatrix}
}_{\boldsymbol{\alpha}_{\mathrm{PSV}}}
\underbrace{
\begin{pmatrix}
\mathbf{u}_z \\
\mathbf{u}_x \\
\boldsymbol{\Omega}^{-1}\boldsymbol{\rho}^{-1}\boldsymbol{\tau}_{zz} \\
\boldsymbol{\Omega}^{-1}\boldsymbol{\rho}^{-1}\boldsymbol{\tau}_{xz}
\end{pmatrix}
}_{\mathbf{b}_{\mathrm{PSV}}}.
\tag{137}
$$

As in the case of SH waves, by applying the transformation $\mathbf{b}_{\mathrm{PSV}} = \mathbf{D}_{\mathrm{PSV}}\mathbf{v}_{\mathrm{PSV}}$, where $\mathbf{D}_{\mathrm{PSV}}$ is the eigenvector matrix of $\boldsymbol{\alpha}_{\mathrm{PSV}}$, the system 137 is diagonalized. Then, for a homogeneous medium, it has the solution

$$
\mathbf{v}_{\mathrm{PSV}} = \Bigg(
\underbrace{e^{-i\omega z q_{\alpha_{\mathrm{I}}}}a_{\mathrm{I}}^-}_{P_{\mathrm{I}}^-},\;
\underbrace{e^{-i\omega z q_{\alpha_{\mathrm{II}}}}a_{\mathrm{II}}^-}_{P_{\mathrm{II}}^-},\;
\underbrace{e^{-i\omega z q_{\beta_{\mathrm{I}}}}b_{\mathrm{I}}^-}_{S_{\mathrm{I}}^-},\;
\underbrace{e^{-i\omega z q_{\beta_{\mathrm{II}}}}b_{\mathrm{II}}^-}_{S_{\mathrm{II}}^-},
$$

$$
\underbrace{e^{i\omega z q_{\alpha_{\mathrm{I}}}}a_{\mathrm{I}}^+}_{P_{\mathrm{I}}^+},\;
\underbrace{e^{i\omega z q_{\alpha_{\mathrm{II}}}}a_{\mathrm{II}}^+}_{P_{\mathrm{II}}^+},\;
\underbrace{e^{i\omega z q_{\beta_{\mathrm{I}}}}b_{\mathrm{I}}^+}_{S_{\mathrm{I}}^+},\;
\underbrace{e^{i\omega z q_{\beta_{\mathrm{II}}}}b_{\mathrm{II}}^+}_{S_{\mathrm{II}}^+}
\Bigg)^T.
\tag{138}
$$

The elements P_{I}^- and P_{II}^- are, respectively, the up-going fast and slow P-waves, and P_{I}^+ and P_{II}^+ are the down-going fast and slow P-waves, respectively.

6.1.3 Recursive solution for wave propagation across a stack of porous layers

Kennett's reflectivity method (Kennett, 1983) shows that the wave propagation across a stack can be computed by iteratively applying the plane wave solution for each homogeneous layer (equations 136 and 138) and, then, the reflection and transmission coefficients at each contact. It gives an exact solution in the $\omega - k$ domain.

For a down-going wave incident from the upper-medium, the solution for total re-

flected ($\mathbf{R}^D$) and transmitted ($\mathbf{T}^D$) waves is first established at the contact of the last layer (N) and the lower half-space as if it was the only interface. At this contact, the amplitudes $\mathbf{R}_N^D$ and $\mathbf{T}_N^D$ are the reflection ($\mathbf{r}_N^D$) and transmission ($\mathbf{t}_N^D$) coefficients for down-going waves incident at a single contact, which are developed in Chapter 5. The terms $\mathbf{r}^D$ and $\mathbf{t}^D$ for the case of P- and SV-waves are 4×4 matrix, and they are composed of the upper- and lower-left blocks of $\mathbf{X}_{PSV}$ matrix (equation 129), respectively. For the case of SH-waves, they are 2×2 matrices composed by the upper- and lower-left blocks of $\mathbf{X}_{SH}$ matrix (equation 106), respectively.

Then, the response of the layer $N-1$ is added to the amplitudes $\mathbf{R}_N^D$ and $\mathbf{T}_N^D$. For that, the wavefields are propagated at the contact $N-1$, in between layers N and $N-1$, using the plane wave solution in the homogeneous porous layer N. At the top of layer N, the amplitudes of the total reflected and transmitted wavefields are

$$\mathbf{R}'^D_N = \mathbf{E}_N^D \mathbf{R}_N^D \mathbf{E}_N^D, \tag{139}$$

$$\mathbf{T}'^D_N = \mathbf{T}_N^D \mathbf{E}_N^D. \tag{140}$$

$\mathbf{E}_N^D$ is a diagonal matrix that includes the phase effects due to propagating the wavefields from the bottom to the top of the layer $l = N$. For SH-waves, it is defined as

$$\mathbf{E}_N^D = \text{Diag} \left\{ e^{i\omega q_{\beta_{\mathrm{I}}}^N h_N} \,,\, e^{i\omega q_{\beta_{\mathrm{II}}}^N h_N} \right\}. \tag{141}$$

For the case of P- and SV-waves, it is

$$\mathbf{E}_N^D = \text{Diag} \left\{ e^{i\omega q_{\alpha_{\mathrm{I}}}^N h_N} \,,\, e^{i\omega q_{\alpha_{\mathrm{II}}}^N h_N} \,,\, e^{i\omega q_{\beta_{\mathrm{I}}}^N h_N} \,,\, e^{i\omega q_{\beta_{\mathrm{II}}}^N h_N} \right\}. \tag{142}$$

The elements q_w^N are the vertical slowness for the $w = P_{\mathrm{I}}$-, P_{II}-, S_{I}-, S_{II}-waves in the layer N, and h_N is the layer thickness.

After that, the scattering of the wavefields at the contact $N-1$ is included in the total reflection matrix $\mathbf{R}^D$ by

$$\mathbf{R}_{N-1}^D = \mathbf{r}_{N-1}^D + \mathbf{t}_{N-1}^U \mathbf{R}'^D_N \left[\mathbf{I} - \mathbf{r}_N^U \mathbf{R}'^D_N \right]^{-1} \mathbf{t}_{N-1}^D. \tag{143}$$

In equation 143, the effects of the waves reflected at the contact $n = N-1$ are included

by the term $\mathbf{r}^{D}_{N-1}$. The terms $\mathbf{r}^{U}$ and $\mathbf{t}^{U}$ are, respectively, the reflection and transmission coefficients for up-going waves incident at a single contact. For the case of P- and SV-waves, they are 4 × 4 matrix composed of the upper- and lower-right blocks of $\mathbf{X}_{PSV}$ matrix (equation 129), respectively. For the case of SH-waves, they are 2 × 2 matrices composed by the upper- and lower-right blocks of $\mathbf{X}_{SH}$ matrix (equation 106), respectively. The term $\left[\mathbf{I} - \mathbf{r}^{U}_{N} \mathbf{R}'^{D}_{N}\right]^{-1}$ describes all the interactions that exist between the scattered waves at the contact $n = N-1$ and the scattered waves generated in the stack below the contact. This term is usually replaced by a series expansion as

$$\left[\mathbf{I} - \mathbf{r}^{U}_{N} \mathbf{R}'^{D}_{N}\right]^{-1} \approx \mathbf{I} + \mathbf{r}^{U}_{N} \mathbf{R}'^{D}_{N} + \mathbf{r}^{U}_{N} \mathbf{R}'^{D}_{N} \mathbf{r}^{U}_{N} \mathbf{R}'^{D}_{N} + \dots \ , \tag{144}$$

where the identity matrix $\mathbf{I}$ accounts for the waves that travels once across the layer, and $\mathbf{r}^{U}_{N} \mathbf{R}'^{D}_{N}$, $\mathbf{r}^{U}_{N} \mathbf{R}'^{D}_{N} \mathbf{r}^{U}_{N} \mathbf{R}'^{D}_{N}$, and higher order terms describes waves with multiple reflections in the layers (Kennett, 1983).

The scattering effects on the wavefields $\mathbf{T}^{D}$ become

$$\mathbf{T}^{D}_{N-1} = \mathbf{T}'^{D}_{N} \left[\mathbf{I} - \mathbf{r}^{U}_{N-1} \mathbf{R}'^{D}_{N}\right]^{-1} \mathbf{t}^{D}_{N-1}. \tag{145}$$

It includes the direct transmission and the multiple reflections that are transmitted at the bottom. The multiple reflections can be removed from $\mathbf{T}^{D}$ by substituting the series expansion 144 and retaining only the identity matrix.

The above steps are repeated iteratively until the layer 1 is added to the stack. Thereafter, the matrices $\mathbf{R}^{D}$ and $\mathbf{T}^{D}$ give the total reflection and transmission amplitudes for waves that come from the upper half-space and are scattered in the stack of layers.

This methodology has been implemented in C parallelized by OpenMP. The pseudocode of this implementation is described in section B.3 of Appendix B.

6.2   SH-waves across a stack of layers

To analyze the effects of the fluid viscous stress tensor in a stack of porous layers, first, let us consider the simplest case of a down-going fast SH-wave traveling across a

stack of layers. The total transmission is given by $\mathbf{T}^D\mathbf{d}$. Herein, $\mathbf{d} = [A_{SH}, \, 0]^T$ describes the incident wavefield, and A_{SH} is the amplitude of the incident fast SH-wave, which for this case is taken as 1. In order to remove the influence of reverberations, I vanish the multiple reflections in the calculus of $\mathbf{T}^D$.

The total transmitted fast SH-wave is given by the element (1,1) of $\mathbf{T}^D\mathbf{d}$, and it can be represented as

$$\left(\mathbf{T}^D\mathbf{d}\right)_{1,1} = T^D_{S_I S_I} \sum_{m=1}^{m=N} e^{i\omega q^m_{\beta_I} h^m}, \tag{146}$$

where $T^D_{S_I S_I}$ is the amplitude of the transmitted fast SH-wave that includes all the scattering effects. The term $\sum_{m=1}^{m=N} e^{i\omega q^m_{\beta_I} h^m}$ describes the propagation of the wave across all the layers; this is, the change in phase because of propagation and reduction in amplitude due to the intrinsic attenuation of the fast S-wave. Because the last one exists even if the viscous stress tensor is not taken into account, I focus on the analysis of $T^D_{S_I S_I}$.

Figure 32 shows the amplitude of a fast SH-wave that travels in the normal direction of a stack of ten, one hundred, and one thousand water-saturated sintered glass beads porous layers with the same properties and impermeable surfaces. The layer thickness is one millimeter in all the cases. So, the total thickness for the stack of ten, one hundred, and one thousand are one centimeter, ten centimeters, and one meter, respectively. The properties of porous media are in Table 1 of Appendix A. The magnitude of $T^D_{S_I S_I}$, which includes all scattering effects, is presented in the left panel, and the relative difference is presented in the right panel. Such a difference is computed using the expression 97 in order to observe only the effect of the fluid viscous stress tensor. Herein, the amplitude $T^D_{S_I S_I}$ reduces inversely proportional to the number of layers, and that reduction in amplitude is enhanced with the frequency. Around the critical frequency Ω_i, the amplitude for the case of one thousand layers shows a small increment. It must exist in the low-frequency regime for all number of layers; however, it is only noticeable for the case of one thousand layers around the critical angle.

Because the wave travels in the normal direction and all multiples are removed, the amplitude $T^D_{S_I S_I}$ corresponds to the product of transmission coefficients at each contact. In this case of the same properties in each layer, the amplitude can be analytically

solved. It is

$$T^D_{S_I S_I} = \left(\frac{1}{1 - \gamma_I \frac{Z_{\tau S_{II}}}{Z_{\tau S_I}}} \right)^N \tag{147}$$
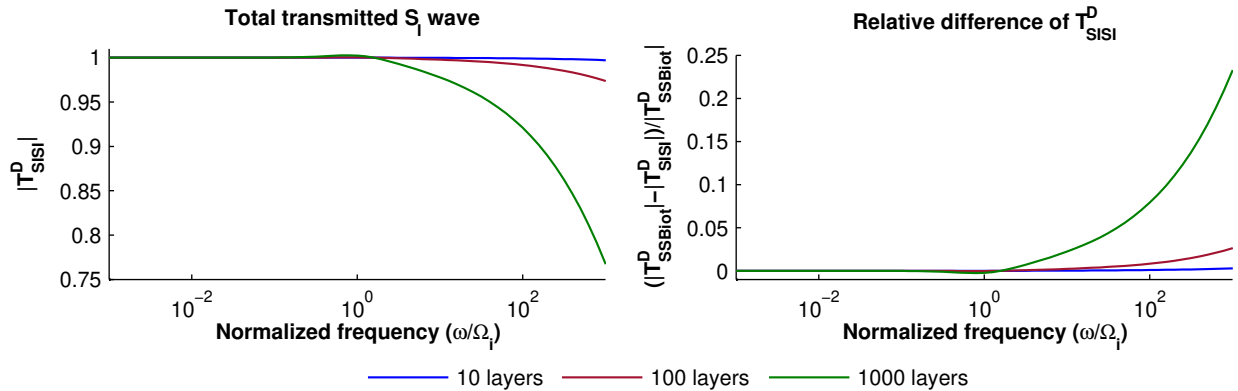
Figure 32. Total transmitted amplitude of a SH wave that travels across a stack of sintered glass beads porous layers with same properties and impermeable surfaces. The frequency is normalized by the Biot critical frequency Ω_i.

Equation 147 is asymptotically expanded in terms of the end-member properties and critical frequencies by applying the asymptotic forms of shear velocities (equations 44 and 45), γ_{β_I} (equation 90), and $\gamma_{\beta_{II}}$ (equation 91). It leads to

$$|T^D_{S_I S_I}| \approx \begin{cases} \left(\dfrac{1}{1 - 2\frac{\omega}{\Omega_b}\left(\eta_0 m_f \frac{\omega}{\Omega_\beta} \frac{\omega}{\Omega_b}\right)^{1/2}} \right)^{N/2}, & \omega \ll \Omega_i. \\[4mm] \left(\dfrac{1}{1 + \frac{2}{s}\left(\frac{\eta_0}{2} \frac{m_f}{s - m_f} \frac{\omega}{\Omega_\beta}\right)^{1/2}} \right)^{N/2}, & \Omega_i \ll \omega \ll \Omega_\beta. \end{cases} \tag{148}$$

The asymptotic form of $|T^D_{S_I S_I}|$ shows that the amplitude decrement observed in the high-frequency regime is dependent on the number of layers. In contrast, the layer thickness is not part of the scattering effects. It is because the generation of slow S-wave is causing this change in amplitude. Then, as it is dissipated very close to its origin, it cannot interact with the waves in other contacts, even if the layer thickness is in the order of the average pore size.

Although the reduction in amplitude is a consequence of the fluid viscous stress

tensor, it is not directly controlled by the viscosity. Instead, is the ratio $\Omega_\beta = \mu_0/\mu_f$ that controls the magnitude of the effect. It means that a fluid with high viscosity saturating a stiff porous rock may cause the same effect than a fluid with low viscosity within a soft porous sample. Moreover, the end-member properties that affect the decrement are the porosity (η_0), tortuosity (S), and the fluid mass fraction (m_f).

The effects of porosity and tortuosity are observed in Figure 33 where the stacks of layers used in Figure 32 are now composed of Berea sandstone (properties in Table 2 of Appendix A), which has a smaller porosity and larger tortuosity than the sintered glass beads porous medium. The change in amplitude shows the same behavior. It reduces with frequency and number of layers; however, the decrement has a smaller magnitude.
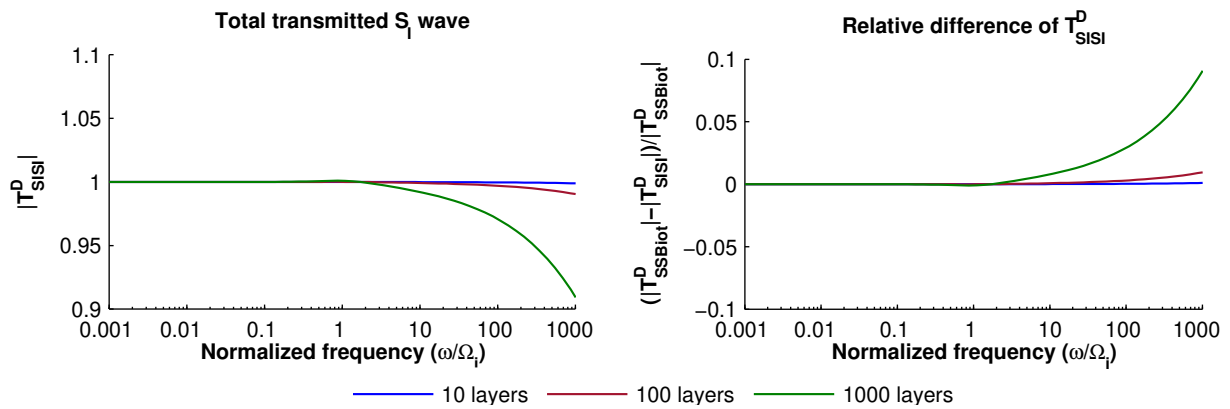
Figure 33. Total transmitted amplitude of a SH-wave that travels across a stack of Berea sandstone layers with same properties and impermeable surfaces. The frequency is normalized by the Biot critical frequency Ω_i.

Figure 34 shows the amplitude $|T^D_{S_I S_I}|$ for a SH-wave that travels at different incident angles. The stack is composed of one thousand Berea sandstone layers with the same properties and impermeable surfaces. It shows that the behavior observed in the normal direction is persistent for the case of non-normal incident angles; it is, the amplitude decreases with frequency. Moreover, as the incident angle increases, the amplitude decreases, and it achieves a relative difference larger than that observed in a stack of sintered glass beads porous media (Figure 32).
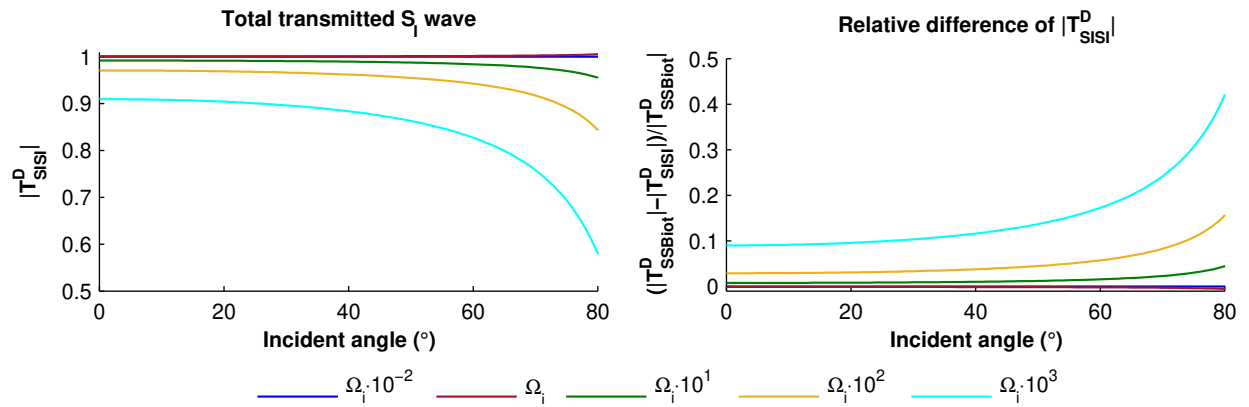
Figure 34. Total transmitted amplitude of a SH-wave that travels across a stack of Berea sandstone layers with same properties and impermeable surfaces. The amplitudes are plotted as a function of the incident angle, and they are presented for the angular frequencies $\Omega_i \cdot 10^{-2}$ (blue), Ω_i (red), $\Omega_i \cdot 10^1$ (green), $\Omega_i \cdot 10^2$ (yellow), and $\Omega_i \cdot 10^3$ (cyan)

The effect of the fluid viscous stress tensor in a stack with change in porosity is presented in Figures 35 and 36. For that, I consider a stack of one thousand Berea sandstone layers with the same properties, except for the porosity that alternates values of 0.2 and 0.21. The variation in porosity is small to reduce the scattering due to a change in stiffness. Even so, the fluid viscous stress tensor effects are present with this small change. For the case of impermeable interfaces, the amplitude $|T^D_{S_I S_I}|$ is presented in Figure 35. It shows that the amplitude of the total transmission reduces with increasing frequency and incident angle. It is the same behavior in the case of the same porosity in all layers. However, in the case of permeable surfaces, the effect of the fluid viscous stress tensor is small (Figure 36). In this case, the total transmission does not have a large variation with the frequency as the impermeable case. It shows a change in the low- and high-frequency regimes, but the reduction in amplitude related to scattering into the slow S-wave is not perceptible. It is because the effect of the fluid viscous stress tensor, in this case, is two orders of magnitude smaller than the case of impermeable interfaces, as the relative difference shows. Thus, the reduction in amplitude due to the transition from low- to high-frequency regime is the only observed in the plot.

Figure 35. Total transmitted amplitude of a SH-wave that travels across a stack of layers with impermeable surfaces. The stack is composed of one thousand Berea sandstone layers with same properties, except for the porosity that alternates values of 0.2 and 0.21. The amplitudes are plotted as a function of the incident angle, and they are presented for the angular frequencies $\Omega_i \cdot 10^{-2}$ (blue), Ω_i (red), $\Omega_i \cdot 10^1$ (green), $\Omega_i \cdot 10^2$ (yellow), and $\Omega_i \cdot 10^3$ (cyan)

Figure 36. Total transmitted amplitude of a SH-wave that travels across a stack of layers with permeable surfaces. The stack is composed of one thousand Berea sandstone layers with same properties, except for the porosity that alternates values of 0.2 and 0.21. The amplitudes are plotted as a function of the incident angle, and they are presented for the angular frequencies $\Omega_i \cdot 10^{-2}$ (blue), Ω_i (red), $\Omega_i \cdot 10^1$ (green), $\Omega_i \cdot 10^2$ (yellow), and $\Omega_i \cdot 10^3$ (cyan)

6.3 P- and SV- waves across a stack of layers

This section analyzes the effects of the fluid viscous stress tensor on P- and SV-waves across the stack of porous layers. In this case, the incident wavefields are $\mathbf{d}_{P_I} = [A_{P_I}, 0, 0, 0]^T$ for the fast P-wave, and $\mathbf{d}_{S_I} = [0, 0, A_{S_I}, 0]^T$ for the fast S-wave. In order to remove the influence of reverberation, the multiple reflections are neglected in the calculus of $\mathbf{T}^D$. The total transmitted fast P- and SV-waves are given by the

elements (1,1) and (3,1) of $\mathbf{T}^D\mathbf{d}$, respectively. They can be represented as

$$\left(\mathbf{T}^D\mathbf{d}_{P_I}\right)_{1,1} = T^D_{P_I P_I} \sum_{m=1}^{m=N} e^{i\omega q^m_{\alpha_I} h^m}, \tag{149}$$

$$\left(\mathbf{T}^D\mathbf{d}_{S_I}\right)_{3,1} = T^D_{S_I S_I} \sum_{m=1}^{m=N} e^{i\omega q^m_{\beta_I} h^m}. \tag{150}$$

The elements $T^D_{P_I P_I}$ and $T^D_{S_I S_I}$ are, respectively, the amplitude of the transmitted fast P- and SV-waves. They include all the scattering effects.

Figure 37 shows the amplitudes $|T^D_{P_I P_I}|$ and $|T^D_{S_I S_I}|$ at different incident angles. The stack is composed of one thousand Berea sandstone layers with the same properties and impermeable surfaces. The amplitude $|T^D_{P_I P_I}|$ shows a complete transmission in the low-frequency regime. In the high-frequency regime, there is a reduction in amplitude at the normal incident angle due to the generation of slow P waves, and the amplitude increase with the angle. The relative difference with respect to the Biot value shows that the effect of the fluid viscous stress tensor for the fast P-wave is small. It increases with the incident angle, and it is in the order of 10^{-5}. The amplitude $|T^D_{S_I S_I}|$ in the normal direction shows the same behavior than that in the SH-wave. At the non-normal incident angle, the amplitude rapidly decays with increasing angle. It is because of the scattering into P-waves. The effect of the fluid viscous stress tensor is in the same order that in the SH case, as it is observed in the relative difference. This effect reduces with the incident angle.

The effect of the fluid viscous stress tensor in a stack with change in porosity is presented in Figures 38 and 39. For that, I consider a stack of one thousand Berea sandstone layers with the same properties, except for the porosity that alternates values of 0.2 and 0.21. The variation in porosity is small to reduce the scattering due to a change in stiffness. Even so, the fluid viscous stress tensor effects are present with this small change. For the case of impermeable interfaces, the amplitudes $|T^D_{P_I P_I}|$ and $|T^D_{S_I S_I}|$ are presented in Figure 38. $|T^D_{P_I P_I}|$ has an amplitude of 0.98 due to the scattering waves. In this case, the effect of the fluid viscous stress tensor causes a reduction in amplitude of two times the value in the case of the same porosity in all layers. It is in the order of 10^{-5}. The amplitude $|T^D_{S_I S_I}|$ shows the same behavior as the case of the same porosity in all layers.
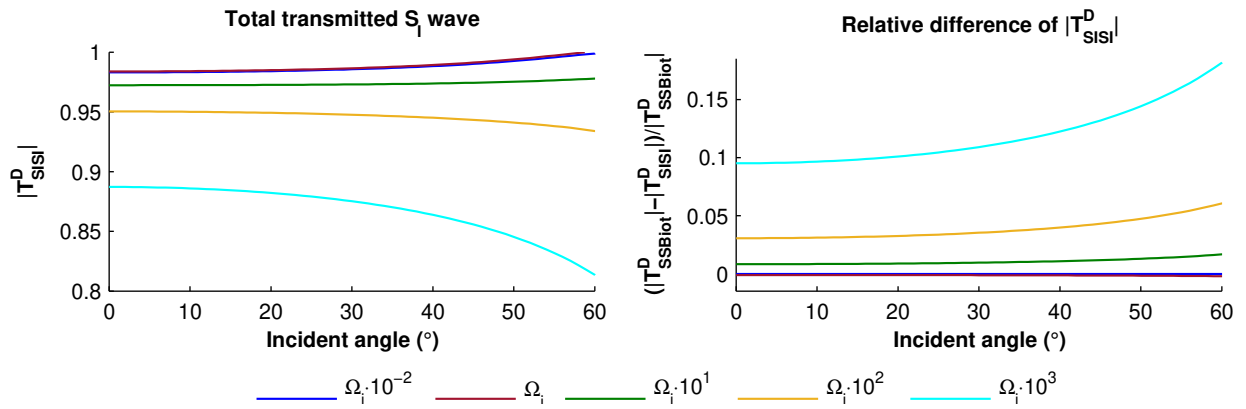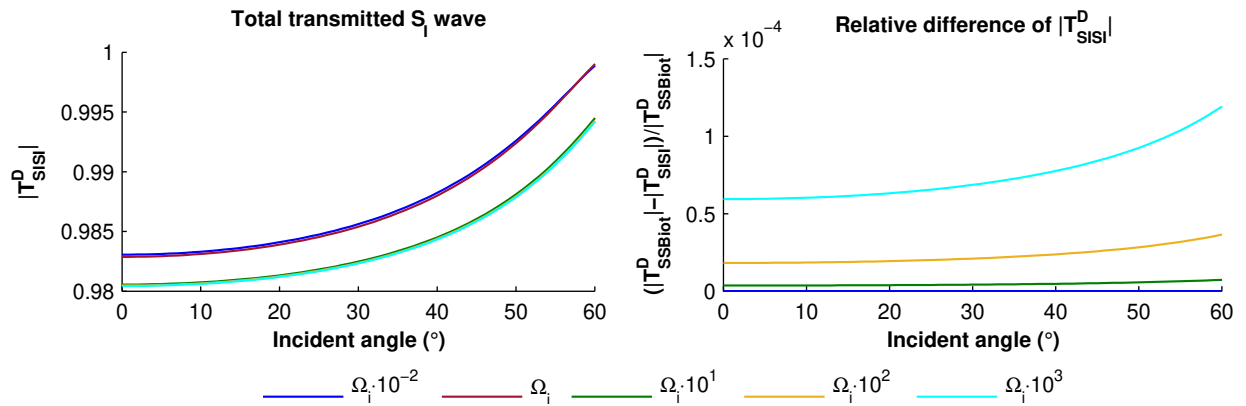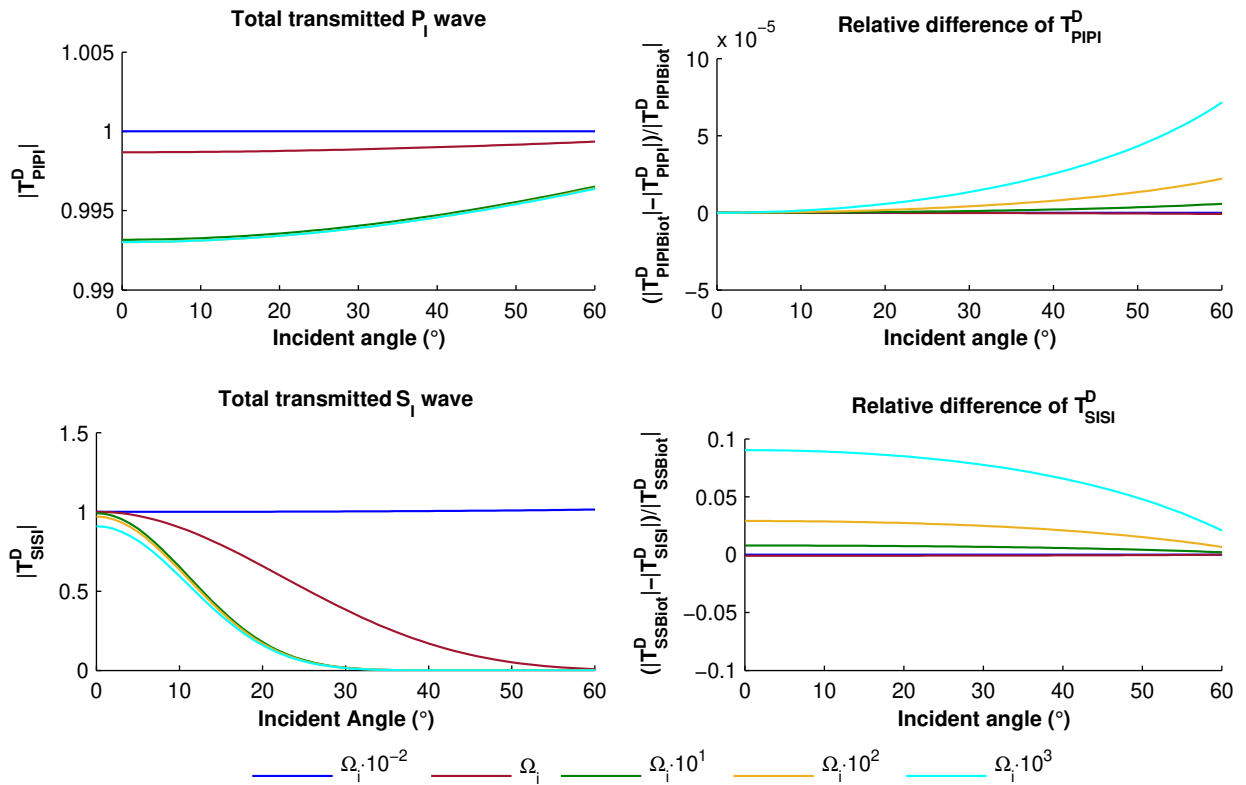
Figure 37. Total transmitted amplitude of P- and SV-waves that travel across a stack of Berea sandstone layers with same properties and impermeable surfaces. The amplitudes are plotted as a function of the incident angle, and they are presented for the angular frequencies $\Omega_i \cdot 10^{-2}$ (blue), Ω_i (red), $\Omega_i \cdot 10^1$ (green), $\Omega_i \cdot 10^2$ (yellow), and $\Omega_i \cdot 10^3$ (cyan)

Figure 39 shows the amplitudes $|T_{P_I P_I}^D|$ and $|T_{S_I S_I}^D|$ in the case of permeable surfaces. The amplitude $|T_{P_I P_I}^D|$ has a larger reduction than in the impermeable case; however, the effect of the fluid viscous stress tensor is three orders of magnitude smaller. The amplitude $|T_{S_I S_I}^D|$ shows a large value that indicates a low scattering into the other process. It is completely different than in the case of impermeable surfaces. The effect of the fluid viscous stress tensor increases with the frequency and reduces with the incident angle, and it is in the order of 10^{-5}. It is four orders of magnitude smaller than in the case of impermeable surfaces.
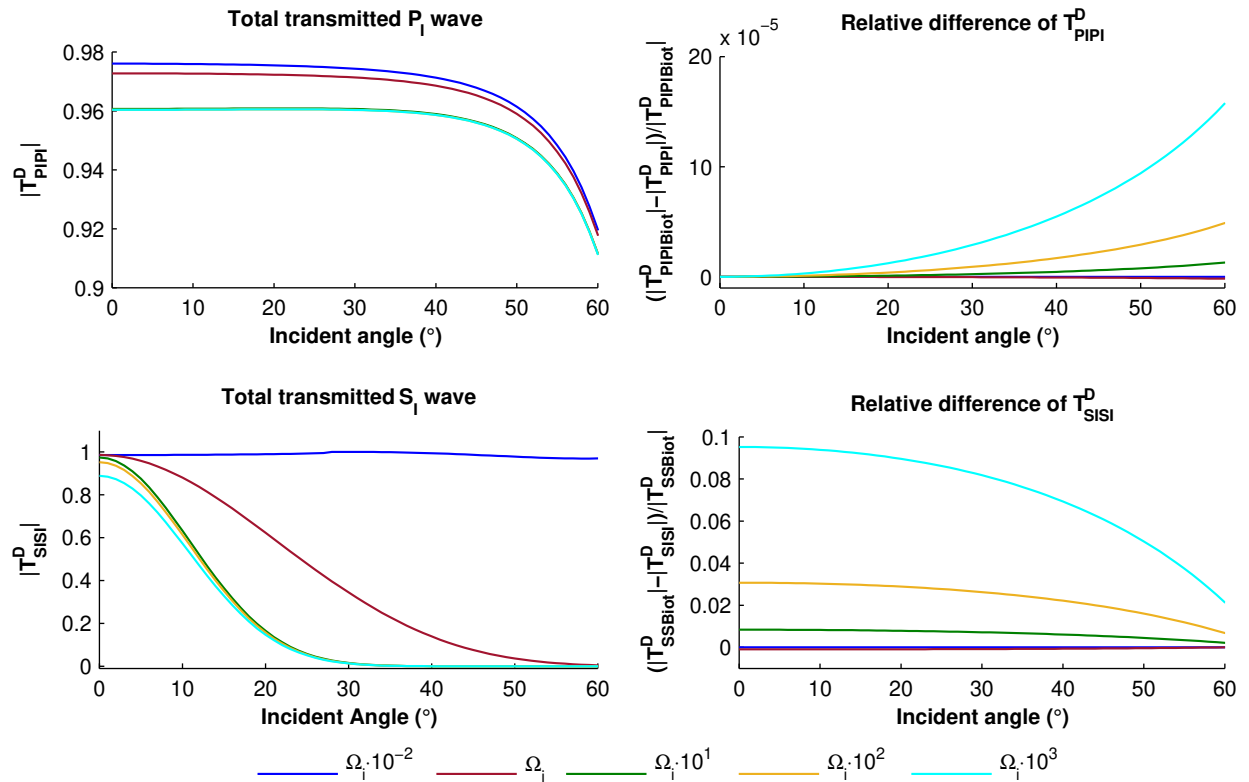
Figure 38. Total transmitted amplitude of P- and SV-waves that travel across a stack of layers with impermeable surfaces. The stack is composed of one thousand Berea sandstone layers with same properties, except for the porosity that alternates values of 0.2 and 0.21. The amplitudes are plotted as a function of the incident angle, and they are presented for the angular frequencies $\Omega_i \cdot 10^{-2}$ (blue), Ω_i (red), $\Omega_i \cdot 10^1$ (green), $\Omega_i \cdot 10^2$ (yellow), and $\Omega_i \cdot 10^3$ (cyan)
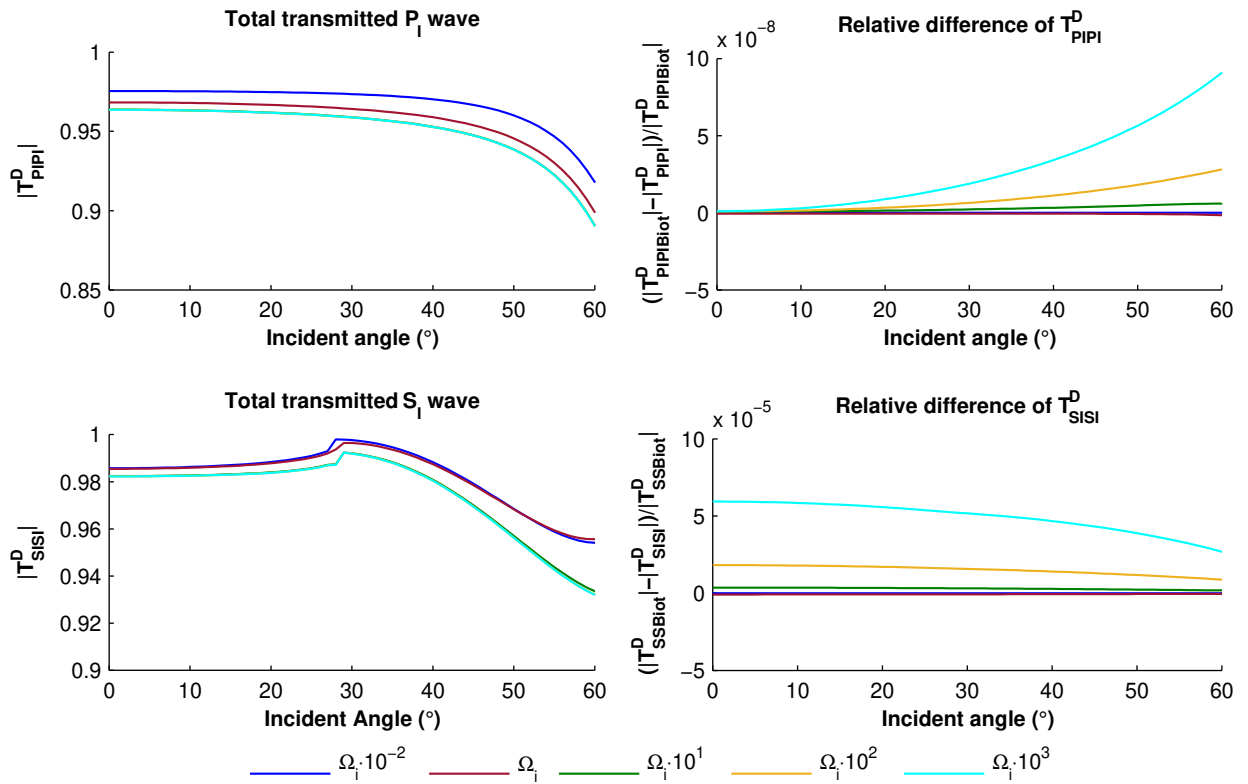
Figure 39. Total transmitted amplitude of P- and SV-waves that travel across a stack of layers with permeable surfaces. The stack is composed of one thousand Berea sandstone layers with same properties, except for the porosity that alternates values of 0.2 and 0.21. The amplitudes are plotted as a function of the incident angle, and they are presented for the angular frequencies $\Omega_i \cdot 10^{-2}$ (blue), Ω_i (red), $\Omega_i \cdot 10^1$ (green), $\Omega_i \cdot 10^2$ (yellow), and $\Omega_i \cdot 10^3$ (cyan)

Chapter 7.   Amplitude decrease due to conversion scattering as a quality factor

In previous chapters, the fluid viscous stress tensor effects are analyzed from the amplitude of scattered waves. This chapter examines those effects in terms of the quality factor Q. This is done by analyzing the reduction in amplitude due to the conversion scattering into the slow S-wave for a wavefield traveling across a stack of plane layers, as per amplitude computed in chapter 6. In order to eliminate the conversion scattering due to contrast in physical properties, a stack composed of plane layers with the same properties and impermeable contacts is considered. In addition, to avoid mode conversion to P waves, the analysis is performed for SH waves. In this case, the generation of fluid vorticity at each contact, directly related to the fluid viscous stress tensor, is the only process affecting the wave propagation.

Section 7.1 gives the framework to relate the reduction in amplitude of the total transmitted wave, which has traveled across a stack of plane poroelastic layers, and the quality factor. Then, based upon that, section 7.2 computes the values of Q for an SH-wave that has traveled across the stack. Finally, in section 7.3, the values of Q computed from the direct transmissions are contrasted with the quality factor computed in the Biot theory with the JKD model.

7.1 Quality factor from the transmission amplitude

The reduction in amplitude of a direct wave that travels across a stack of porous layers can be interpreted as a spatial attenuation factor α. They are related by

$$T = e^{(-\alpha L)}, \tag{151}$$

where T is the amplitude of a wave, of unitary amplitude at the origin, that has traveled across the stack of layers of the length L.

The spatial attenuation factor α and the quality factor Q are related by

$$\frac{1}{Q} = 2\frac{\alpha V}{\omega}, \tag{152}$$

where V is the phase velocity of the wave (Mavko et al., 2009).

Substituting equations 146, 149, and 150 for the amplitude of direct transmitted waves in equation 151, and using the relation 152, Q is defined as

$$\frac{1}{Q_w} \; = \; \underbrace{2\frac{\text{Imag}(q_w)}{\text{Re}(q_w)}}_{\frac{1}{Q1_w}} \underbrace{-\frac{2}{L}\frac{1}{\omega\text{Re}(q_w)}ln\left(|T_w|\right)}_{\frac{1}{Q2_w}}, \tag{153}$$

where the sub-index w labels the primary wave field being analyzed, which could be P_I, SV_I or SH_I. Imag and Re are the imaginary and real parts of its argument, the slowness q_w. ln and $|\cdot|$ stand for the natural logarithm and the magnitude of its argument, respectively. In the right hand side of equation 153, the term $Q1_w$ represents the quality factor that describes the amplitude decay due to intrinsic losses implicit in the theoretical framework. This factor affects the wave even in a homogeneous medium. $Q2_w$ represents the contribution to the quality factor of the reduction in amplitude due to conversion scattering.

In next sections, Q_w is computed in the Biot theory without and with the JKD model, and in the dCS theory. They are, respectively, identified by the super-indices (Biot), (JKD), and (dCS).

7.2 Quality factor of an SH-wave traveling across a stack of layers

This section analyzes the quality factor 153 in the dCS theory, $Q_{SH_I}^{(\text{dCS})}$, for the case of a normal incident SH_I-wave that travels across a stack of plane poroelastic layers with the same properties, the same thickness (h), and impermeable contacts. This case is helpful because $Q2_{SH_I}^{(\text{dCS})}$ is vanishing if the fluid viscous stress tensor is not taken into account. Therefore, in this case, $Q2_{SH_I}^{(\text{dCS})}$ manifests the attenuation due to vorticity diffusion described with the viscous stress tensor. Additionally, since all the layers has the same properties, $Q1_{SH_I}^{(\text{dCS})}$ is the quality factor of a homogeneous poroelastic medium, which is already described in section 2.4.1 of Chapter 2.

Because the propagation is in the normal direction, $q_{\beta_I} = 1/\beta_I$, and the travel distance is $L = hN$, where N is the number of layers in the stack. Then, by substituting the expression 147 for T_{SH_I} in equation 153, the inverse of $Q2_{SH_I}^{(\text{dCS})}$ becomes

$$\frac{1}{Q2_{SH_I}^{(dCS)}} = \frac{2}{h}\frac{Re\left(\beta_I\right)}{\omega}ln\left(\left|1-\gamma_I\frac{Z_{\tau S_{II}}}{Z_{\tau S_I}}\right|\right). \tag{154}$$

In contrast with the analysis of amplitude presented in Chapter 6, which shows independence on the layer thickness, equation 154 shows that the $Q2_{SH_I}^{(dCS)}$ is a function of the ratio between the wavelength ($Re\left(\beta_I\right)/\omega$) and the layer thickness h, and the transmitted wave amplitude in a single contact. Neither the stack length nor the number of layers affects $Q2_{SH_I}^{(dCS)}$ in this case.

The independence of $Q2_{SH_I}^{(dCS)}$ on the number of layers and the stack length is observed in Figure 40. It shows the inverse of quality factors $Q_{SH_I}^{(dCS)}$ (left panel) and $Q2_{SH_I}^{(dCS)}$ (right panel) for the case of the stacks of ten, one hundred, and one thousand water-saturated sintered glass beads porous layers with the same properties, 1 millimeter layer thickness, and impermeable contacts. The properties of porous media and saturating-fluid are, respectively, in Tables 1 and 3 of Appendix A. Although the amplitude T_{SH_I} decreases with the number of layers (see Figure 32), in Figure 40 is observed that the factor $Q2_{SH_I}^{(dCS)}$ is the same in the three stacks, as per equation 154. Herein, the values of $1/Q2_{SH_I}^{(dCS)}$ are two orders of magnitude smaller than $1/Q_{SH_I}^{(dCS)}$, showing that $Q1_{SH_I}^{(dCS)}$ controls the quality factor in this case.
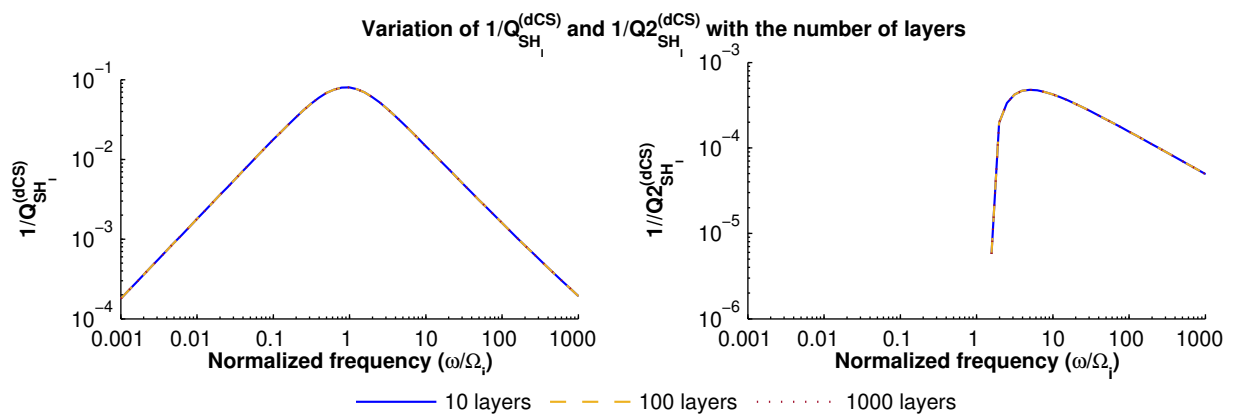
Figure 40. Variation of the inverse of quality factors $Q_{SH_I}^{(dCS)}$ and $Q2_{SH_I}^{(dCS)}$ with the number of layers. The quality factors are computed for a stack composed of ten, one hundred, and one thousand porous layers with the same properties and impermeable surfaces.

Furthermore, Figure 41 shows the increment on values of inverse quality factors with reducing the layer thickness h. It presents the inverse quality factors $Q_{\mathrm{SH_I}}^{\mathrm{(dCS)}}$ and $Q2_{\mathrm{SH_I}}^{\mathrm{(dCS)}}$ for the stacks of one hundred layers with layer thickness of h= 1mm, 0.1 mm and 23 μm. These thicknesses are 43.5, 4.3 and 1 times the average pore-throat size Λ. Herein, as the layer thickness reduces, the effect of $Q2_{\mathrm{SH_I}}^{\mathrm{(dCS)}}$ on $Q_{\mathrm{SH_I}}^{\mathrm{(dCS)}}$ increases and becomes more significant than that of $Q1_{\mathrm{SH_I}}^{\mathrm{(dCS)}}$.
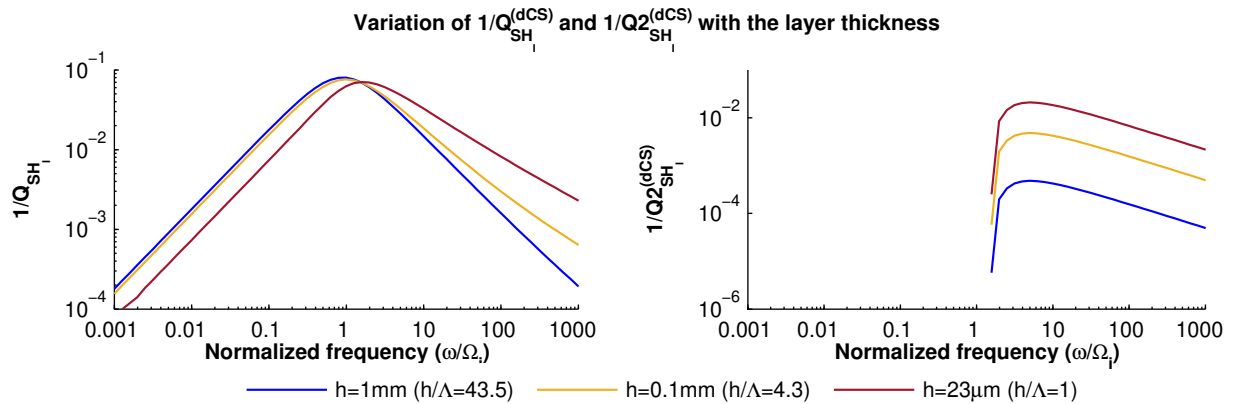
Figure 41. Variation of the inverse of quality factors $Q_{\mathrm{SH_I}}^{\mathrm{(dCS)}}$ and $Q2_{\mathrm{SH_I}}^{\mathrm{(dCS)}}$ with the layer thickness. The quality factors are computed for a stack composed of one hundred porous layers with the same properties and impermeable surfaces. The layer thickness in each stack are $h = 43\Lambda$, $h = 4.3\Lambda$, and $h = \Lambda$.

To understand the controlling factors affecting $Q2_{\mathrm{SH_I}}^{\mathrm{(dCS)}}$, the expression 154 is expanded in terms of frequency by substituting the approximations for the fast S-wave velocity (equation 44) and the amplitude $\mathrm{T_{SH_I}}$ (equation 148). Then, $Q2_{\mathrm{SH_I}}^{\mathrm{(dCS)}}$ is approximated as

$$\frac{1}{Q2_{\mathrm{SH_I}}^{\mathrm{(dCS)}}} \approx \frac{1}{h}\frac{\beta_c}{\omega} \times \begin{cases} ln\left(1 - 2\frac{\omega}{\Omega_b}\left(\eta_0 m_f \frac{\omega}{\Omega_\beta}\frac{\omega}{\Omega_b}\right)^{1/2}\right), & \omega \ll \Omega_i. \\[2em] \frac{1}{\sqrt{1-\frac{m_f}{S}}}\ln\left(1 + \frac{2}{S}\left(\frac{\eta_0}{2}\frac{m_f}{S-m_f}\frac{\omega}{\Omega_\beta}\right)^{1/2}\right), & \Omega_i \ll \omega \ll \Omega_\beta. \end{cases} \tag{155}$$

The equation 155 shows that, in the high-frequency regime, the value of $Q2_{\mathrm{SH_I}}^{\mathrm{(dCS)}}$ depends on the porosity, tortuosity, fluid mass fraction and is weighted by the factor $(\omega/\Omega_\beta)^{1/2}$. In the low-frequency regime, the factor $Q2_{\mathrm{SH_I}}^{\mathrm{(dCS)}}$ approach to zero with negative values. Because of that, the plot of $Q2_{\mathrm{SH_I}}^{\mathrm{(dCS)}}$ in log scale only shows values in

the high-frequency regime. The negative values are not an unphysical behavior. They are a consequence of a negligible increment on amplitude T_{SH_I} in the low-frequency regime.

As equation 155 shows, the quality factor $Q_{SH_I}^{(dCS)}$ and $Q2_{SH_I}^{(dCS)}$ are affected by the ratio $\mu_0/\mu_f = \Omega_\beta$. This effect is observed in Figures 42 and 43. Figure 42 shows the quality factors for three stacks of one hundred porous layers saturated with fluids of different viscosity. All layers have the same properties and correspond to the sintered glass beads porous medium. The saturating fluid is an idealized fluid with the properties of water, except for the shear viscosity which takes values of $\mu_f = 1.5 \times 10^{-3}$, 1.5×10^{-2}, and 1.5×10^{-1} Pa·s. Because Ω_i change with viscosity, in this case, the angular frequency ω is taken instead of the normalized frequency. $Q_{SH_I}^{(dCS)}$ and $Q2_{SH_I}^{(dCS)}$ show the same values for $\mu_f = 1.5 \times 10^{-3}$ and $\mu_f = 1.5 \times 10^{-2}$ except for a shift on the peak frequency. For the case of $\mu_f = 1.5 \times 10^{-1}$, the crossover frequency $\Omega_\beta^\dagger$ is achieved. It causes a higher value in $Q_{SH_I}^{(dCS)}$ due to the $Q1_{SH_I}^{(dCS)}$. However, the change on $Q2_{SH_I}^{(dCS)}$ is not apparent.

Variation of $1/Q_{SH_I}^{(dCS)}$ and $1/Q2_{SH_I}^{(dCS)}$ with the fluid shear viscoaity (μ_f)

μ_f=1.5x10^{-3} Pa·s μ_f=1.5x10^{-2} Pa·s μ_f=1.5x10^{-1} Pa·s
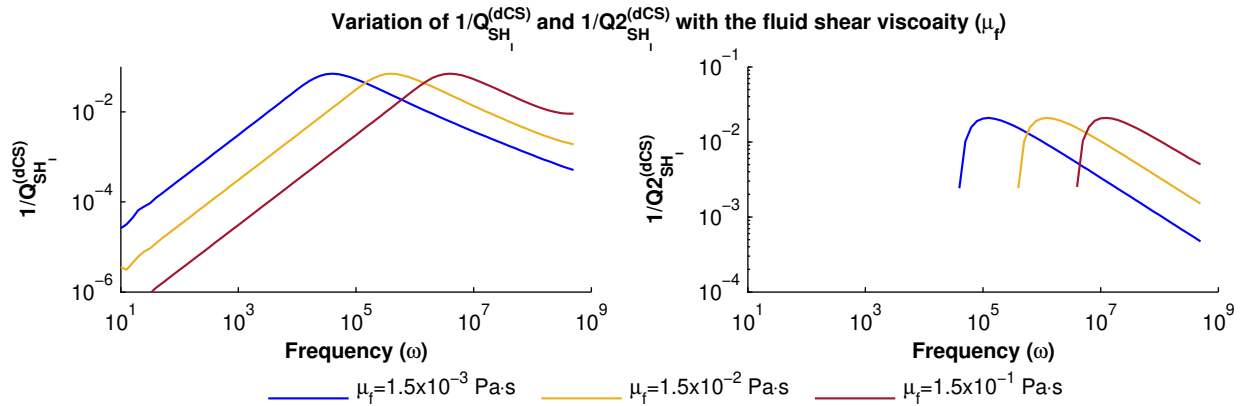
Figure 42. Variation of quality factors $Q_{SH_I}^{(dCS)}$ and $Q2_{SH_I}^{(dCS)}$ with the shear viscosity of the fluid. The quality factors are computed for a stack composed of one hundred porous layers with the same properties, impermeable surfaces, and layer thickness of $h = \Lambda$. The saturating fluids have the properties of water, except the shear viscosity that takes the values 1.5×10^{-3}, 1.5×10^{-2}, and 1.5×10^{-1} Pa·s.

To observe the effect of μ_0, Figure 43 plots the quality factors for three water-saturated stacks of sintered glass beads porous layers with the same properties, impermeable surface, and different μ_0 in each stack. The values of the shear modulus of the frame are $\mu_0 = 3.6$ GPa, 360 MPa, and 36 MPa. Such a variation is an ideal-

ized case where all properties are fixed except for μ_0. Figure 155 shows that $Q_{SH_I}^{(dCS)}$ increase with the reduction in μ_0. It is because of $Q1_{SH_I}^{(dCS)}$ that, for the lower values of μ_0, is being affected by the saturated-frame relaxation peak at Ω_β. In contrast, the value of $Q2_{SH_I}^{(dCS)}$ is slightly affected by the change on μ_0.
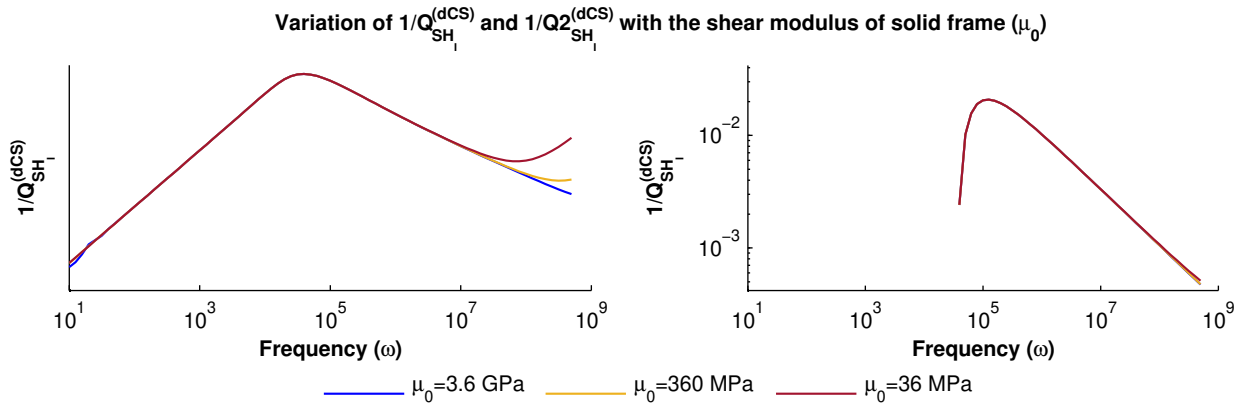
Figure 43. Variation of quality factors $Q_{SH_I}^{(dCS)}$ and $Q2_{SH_I}^{(dCS)}$ with the shear modulus of the frame. The quality factors are computed for three different stacks composed of one hundred porous layers, with impermeable surface and the same properties, except the shear modulus of the solid frame that takes the values 3.6 GPa, 360 MPa, and 36 MPa. The layer thickness is $h = \Lambda$.

7.3 Comparison of quality factor due to conversion scattering with that in the Biot theory with JKD model

Since JKD model aims to account for the effect of the development of VBLs in the Biot theory, this section contrasts its quality factor with $Q2_{SH_I}^{(dCS)}$, which accounts for the generation of fluid vorticity in the dCS theory. For the case of a stack of plane porous layers with the same properties and impermeable contacts, in the Biot theory, with or without JKD model, the SH-waves do not suffer conversion scattering across the interfaces of the stack. So, in this theory, the quality factor is given only by $Q1_{SH_I}^{(Biot)}$ or $Q1_{SH_I}^{(JKD)}$ if the dynamic permeability is included.

Even though the quality factor in the Biot theory with the JKD model, $Q_{SH_I}^{(JKD)}$, has only the term $Q1_{SH_I}^{(JKD)}$ in this case, the dynamic permeability effect lumped within it can be extracted out as

$$\frac{1}{Q1_{SH_I}^{\prime(JKD)}} = \frac{1}{Q1_{SH_I}^{(JKD)}} - \frac{1}{Q1_{SH_I}^{(Biot)}} \ , \tag{156}$$

where $Q1_{SH_I}^{(Biot)}$ is the quality factor in the Biot theory without the JKD model. $Q1_{SH_I}^{\prime(JKD)}$ can be viewed as the contribution of the development of VBLs to the quality factor. So it can be contrasted with $Q2_{SH_I}^{(dCS)}$.

The values of $Q1_{SH_I}^{\prime(JKD)}$ and $Q2_{SH_I}^{(dCS)}$ are compared in Figure 44. $Q2_{SH_I}^{(dCS)}$ is plotted for three different layer thicknesses, whereas $Q1_{SH_I}^{\prime(JKD)}$ is plotted only once because it is the same in the three cases. Figure 44 shows that both quality factors appear only in the high-frequency regime. It is because the vorticity, so the VBLs, are only developed in that regime. It is observed that $Q1_{SH_I}^{\prime(JKD)}$ is close to $Q2_{SH_I}^{(dCS)}$ in the case that the layer thickness is the same that the average pore-throat size ($h = \Lambda = 23 \ \mu m$). It means that the JKD model accounts for the specific case where the fluid vorticity is developed at each pore as if they were completely closed.
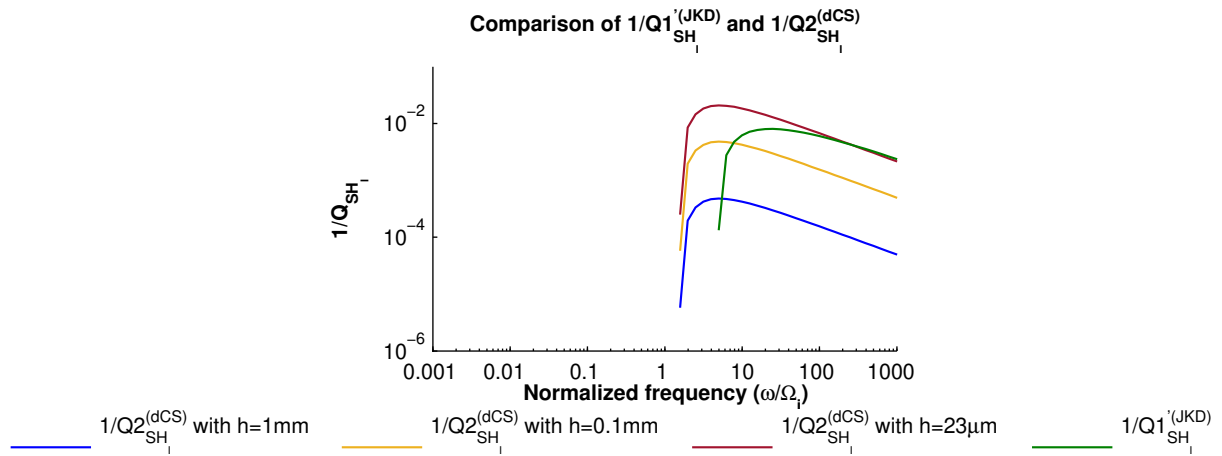
Figure 44. Comparison of the quality factors $Q1_{SH_I}^{\prime(JKD)}$ and $Q2_{SH_I}^{(dCS)}$. The quality factors are computed for a stack of hundred porous layers with the same properties and impermeable surfaces. The layer thickness in each stack are $h = 1$ mm, $h = 0.1$ mm, and $h = 23 \ \mu m$.

Chapter 8.   Discussion and conclusions

8.1 Proper representation of viscous boundary layers in a porous medium

Viscous boundary layers (VBLs) are the manifestation of the vorticity of Newtonian fluids (Landau and Lifshitz, 1987). In porous media, any relative motion of the fluid develops VBLs at pore interfaces. Although the fluid vorticity is an independent process in Newtonian fluids, equation 38 shows that the fluid shear motion in the Biot theory is not an independent process. Instead, it is proportional to the solid-frame motion. This behavior does not change even after Biot's viscodynamic correction factor (Biot, 1956b) or the dynamic permeability of Johnson et al. (1987) is introduced to account for the emergence of viscous boundary layers (VBL). It is because Biot (1956b) and Johnson et al. (1987) attempt to capture the dissipation within the VBLs by altering the drag force resulting from the Darcy term in the equations of motion. However, a complete description of it would require including the frictional force within the fluid that counteracts the deformation restoration through viscous friction. This force is precisely generated through the fluid viscous stress tensor, which is neglected.

Other authors have worked on incorporating the fluid viscous stress tensor into the poroelastic theory. Applying the mixture theory, Katsube (1985) and Katsube and Carroll (1987a, 1987b) include the viscous stress tensor to the constitutive relations of a porous medium. Katsube shows the equivalences with the Biot theory in the limit of vanishing the viscous stress tensor and concludes that the effects of that tensor are captured by the Darcy mobility term of the Biot theory. Pride et al. (1992) describe porous media by applying the volume averaging method, as in the dCS theory. However, they neglect the viscous stress tensor from their formulation under the assumption that its effect is negligible. Therefore, Pride et al. conclude that the viscous forces are fully characterized by the Darcy mobility term of the Biot theory, as Katsube did. This is plausible at a single heterogeneity where the effect is small, as Chapter 5 shows. However, this assumption is not valid in heterogeneous media where the generation of fluid vorticity at each contact causes a considerable reduction in amplitude of the waves, as it is shown in Chapter 6.

Sahay (2008) analyzes the behavior of S-waves in the dCS theory, which retains the viscous stress tensor in the constitutive relation. Here it is shown that account-

ing for that tensor allows describing the fluid vorticity as an independent process, the slow S-wave, as it was pointed out since the beginning of the dCS theory. The description of the fluid vorticity as a separate process shows a negligible effect on the wave propagation in infinite homogeneous porous media. However, this is not the case for heterogeneous media. From the problem of a porous half-space in contact with a solid half-space presented in Chapter 4, it is shown that the lack of freedom of the fluid vorticity impedes the proper description of the fluid motion at the interface. While the Biot theory predicts an unphysical relative fluid motion at the contact, the analysis in Chapter 4 shows that the mode conversion into the slow S-wave generates an opposite movement of the fluid, which counteracts that caused by the fast S-wave to ensure that the no-slip boundary condition holds.

Moreover, from the analysis of SH waves across a stack, it is shown that the fast S-wave attenuation predicted with the Johnson et al. (1987) dynamic permeability corresponds with the scattering into the slow S-wave at each pore, as it was shown in randomly inhomogeneous porous media (Müller and Sahay, 2011b). However, it is not the general case; it only happens in the case of layers with impermeable surfaces. If the interfaces are permeable, the effect of slow-S wave scattering is smaller, causing less attenuation. It means that the JKD model implies that the pores are not connected in the direction of propagation. Additionally, for the case of non-normal angles, the drop in amplitude is larger; thus, its attenuation must increase. Also, the scattering into the slow S-wave causes a minor decrease in amplitude of the P- and SV-waves, and that drop is angle-dependent. Therefore, the attempt to capture the development of VBLs by a single term in the equation of motion is incomplete in a general case of heterogeneous media because it cannot capture all these effects.

It demonstrates the importance of considering the fluid vorticity as an independent process, the slow S-wave, that properly represents the development of VBLs at the contact of discontinuities.

8.2 Implications of fluid viscous stress tensor on wave propagation across discontinuities

The slow S-wave does not exist when the fluid viscous stress tensor is not part of the constitutive equations. Hence propagating waves cannot be converted into this

diffusion wave. By contrasting the solution of reflection and transmission problem in the dCS and Biot theories, I find that the mode conversion into the slow S-wave not only guarantees the no-slip condition at discontinuities, as it is shown in Chapter 4, but it also affects the amplitude of scattered waves.

The reflection and transmission solution for fast SH-waves incident at an imperme-able contact of two porous media with the same properties shows a change in the amplitude of the scattered fast SH-waves, and such a change is related to the fluid viscous stress tensor. It is because the relative fluid motion in the tangential direction vanishes at the contact, as the no-slip conditions define. Thus, there is no strain rate in the fluid, and, consequently, the viscous forces are null at the contact. It generates a change in the total stress, which the fast SH-wave causes in a porous medium, that induces scattering in the incident wave, reducing its amplitude and generating a re-flected fast S-wave. To balance this perturbation in amplitude, which also affects the energy carried by the fast S-waves, a reflected and a transmitted slow S-wave are gen-erated at the contact. Although it is an idealized case, it shows that the fluid viscous forces affect fast waves that travel across heterogeneities.

The effect of the fluid viscous stress tensor is not constrained to the SH-waves, but this effect is present in the P- and SV-waves, too. The impact in SV-waves is compara-ble to that in the SH-waves. In contrast, it is orders of magnitude smaller in the incident P-waves. Even though it cannot be just ignored without analyzing the implications. As it is shown in Chapter 6, the generation of the slow S-wave at multiple contacts, i.e., a stack of layers, enhances the effect of the fluid viscous stress tensor. Although it is smaller than the effect of change in elastic properties, it must be considered in the case of highly heterogeneous porous media.

Because the fluid viscous forces are linked to the fluid motion, a perturbation on the fluid mobility must generate a scattering of the waves, not only the change in elastic properties. It is observed in the case of waves that travel across a stack of porous media with permeable contacts and a slight variation in porosity. Herein, the amplitude of the transmitted waves shows a reduction because of the scattering at each interface. Although the change in porosity also affects the density, the fluid viscous stress tensor influences the amplitude of the scattered waves.

Additionally, the case of impermeable surfaces, where the relative fluid motion vanishes, has substantially affected the scattering even if all media have the same properties. It is the fast SV-waves the more affected by the scattering (see Figure 21). The SV-waves incident at the impermeable contact is strongly scattered as the incident angle increase. It causes that in a stack of layers with impermeable surfaces, the fast SV-waves can not be transmitted at middle and high incident angles, even if the material properties are very similar. It is illustrated in Figure 37, where, above 30 degrees, the fast SV-wave cannot be transmitted across a stack of one thousand Berea sandstone layers. This behavior is not accounted to the fluid viscous stress tensor because it is predicted even in the Biot theory. However, to my best knowledge, it has not been reported before.

8.3 Relevance on seismic exploration

The results presented in this thesis have shown that the fluid viscous stress tensor affects the wave propagation mainly at or above the Biot critical frequency. Therefore, whenever the center frequency of a pulse is comparable or exceeds the Biot critical one, this effect must be taken into account. Because the critical frequency is determined essentially by the kinematic viscosity (ν_f) divided by the permeability (κ), the effects of viscous stress tensor matter in different scenarios depending on fluid and porous frame properties. It is the laboratory setting where this poroelastic effect has its primary importance since most wave propagation experiments are carried out with ultrasonic transducers. Then, more often than not, the pulse frequency exceeds the critical frequency for porous rocks saturated with water/oil. Moreover, it is not uncommon in borehole acoustics that broadband sonic pulses probe a sequence of highly permeable layers. In such a scenario, the pulse frequency may become comparable to the critical frequency, and then, these effects come into play.

Furthermore, the highly heterogeneous media needed to observe a significant effect of the fluid viscous stress tensor are not hard to find in the subsurface. As it is shown in Chapter 6, even a tiny change in porosity can induce a difference in the scattering waves. These variations are common in sedimentary basins where the compaction causes porosity gradients, as well as the change in erosion/deposition rates can affect the porosity. Also, the case of an impermeable surface is not uncom-

mon. It appears at macro-scale in the sandstone formations with interlayered shale sequences. Also, the cementation/compaction can dispose of the clay content such that there are impermeable zones at the scale of a few pores (North, 1985).

8.4 Conclusion

This thesis analyzes the role of the fluid viscous stress tensor in the poroelastic wave propagation across discontinuities. Such discontinuities include changes in elasticity, porosity, or fluid mobility (permeable or impermeable contacts). It is achieved by (i) solving the reflection and transmission problem of incident fast waves at a planar contact and (ii) computing the response of a stack of plane poroelastic layers with the reflectivity method. To separate the effects of the fluid viscous stress tensor from that generated without including this tensor, I contrast the results in the dCS theory with those in Biot theory, which does not contain the fluid viscous stress tensor.

This analysis shows that the missing viscous stress tensor, in the Biot theory, causes a relative fluid motion at the contact that violates the no-slip boundary condition of a viscous fluid. This motion persists even after the dynamic permeability (JKD theory) is incorporated. In contrast, by including the fluid viscous stress tensor into the poroelastic constitutive relations, as it is in the dCS theory, the relative fluid motion vanishes at the contact. This is because at the boundary, a slow S-wave, which manifests the fluid vorticity at macro-scale, is generated through mode conversion. This diffusion wave induces a relative motion of the fluid at the contact, which counteracts the movement caused by the solid-frame field.

Along with the proper representation of the no-slip condition, the fluid viscous stress tensor induces a change in the amplitude of the scattered waves. Such effect is more evident in the S-waves, but it also exists in the P-waves. This effect shows that the development of fluid vorticity is not adequately captured by a single term, as the dynamic permeability. Still, it requires considering all the consequences involved in the scattering. It highlights the need to describe fluid vorticity as an independent process. It also implies that previous implementations of the viscous boundary layer are not fully complete. Because the slow S-wave, which manifests the fluid vorticity as an independent process, can only be described with the fluid viscous stress tensor, the poroelastic description must include that tensor.

References

Ben-Menahem, A. and Singh, S. J. 1981. Seismic waves and sources. Springer-Verlag, New York.

Biot, M. A. 1956a. Theory of propagation of elastic waves in a fluid-saturated porous solid. I. low-frequency range. Journal of the Acoustical Society of America, **28**(2): 168–178.

Biot, M. A. 1956b. Theory of propagation of elastic waves in a fluid-saturated porous solid. II. higher frequency range. Journal of the Acoustical Society of America, **28**(2): 179–191.

Biot, M. A. 1962. Mechanics of deformation and acoustic propagation in porous media. Journal of Applied Physics, **33**(4): 1482–1498.

Bouzidi, Y. and Schmitt, D. R. 2012. Incidence-angle-dependent acoustic reflections from liquid-saturated porous solids. Geophysical Journal International, **191**(3): 1427–1440.

de la Cruz, V. and Spanos, T. 1985. Seismic wave propagation in a porous medium. Geophysics, **50**(10): 1556–1565.

De La Cruz, V., Hube, J., and Spanos, T. 1992. Reflection and transmission of seismic waves at the boundaries of porous media. Wave motion, **16**(4): 323–338.

Deresiewicz, H. and Rice, J. 1964. The effect of boundaries on wave propagation in a liquid-filled porous solid: V. transmission across a plane interface. Bulletin of the Seismological Society of America, **54**(1): 409–416.

Deresiewicz, H. and Skalak, R. 1963. On uniqueness in dynamic poroelasticity. Bulletin of the Seismological Society of America, **53**(4): 783–788.

Geertsma, J. and Smit, D. C. 1961. Some aspects of elastic wave propagation in fluid-saturated porous solids. Geophysics, **26**(2): 169–181.

González Flores, J. G. 2017. Extensional waves in a fluid-saturated porous cylinder with an impermeable radial surface. Master of Science Thesis, Centro de Investigación Científica y de Educación Superior de Ensenada, Baja California. xii, 61 pp.

Johnson, D. L. 1982. Elastodynamics of gels. Journal of Chemical Physics, **77**(3): 1531–1539.

Johnson, D. L., Koplik, J., and Dashen, R. 1987. Theory of dynamic permeability and tortuosity in fluid-saturated porous media. Journal of Fluid Mechanics, **176**: 379–402.

Johnson, D. L., Plona, T. J., and Kojima, H. 1994. Probing porous media with first and second sound. II. acoustic properties of water-saturated porous media. Journal of Applied Physics, **76**(1): 115–125.

Katsube, N. 1985. The constitutive theory for fluid-filled porous materials. Journal of Applied Mechanics, **52**: 185–189.

Katsube, N. and Carroll, M. M. 1987a. The modified mixture theory for fluid-filled porous materials: theory. Journal of Applied Mechanics, **54**: 35–40.

Katsube, N. and Carroll, M. M. 1987b. The modified mixture theory for fluid-filled porous materials: applications. Journal of Applied Mechanics, **54**: 41–46.

Kennett, B. 1983. Seismic wave propagation in stratified media. Cambridge University Press, Cambridge.

Kuteynikova, M., Tisato, N., Jänicke, R., and Quintal, B. 2014. Numerical modeling and laboratory measurements of seismic attenuation in partially saturated rock. Geophysics, **79**(2): L13–L20.

Landau, L. and Lifshitz, E. 1987. Fluid Mechanics. (2nd ed.), Pergamon, New York.

Mavko, G., Mukerji, T., and Dvorkin, J. 2009. The Rock Physics Handbook: Tools for Seismic Analysis of Porous Media. (2nd ed.), Cambridge University Press, Cambridge.

Müller, T. M. and Sahay, P. N. 2011a. Fast compressional wave attenuation and dispersion due to conversion scattering into slow shear waves in randomly heterogeneous porous media. Journal of the Acoustical Society of America, **129**(5): 2785–2796.

Müller, T. M. and Sahay, P. N. 2011b. Stochastic theory of dynamic permeability in poroelastic media. Physical Review E, **84**: 026329.

Müller, T. M. and Sahay, P. N. 2011c. Porous medium acoustics of wave-induced vorticity diffusion. Applied Physics Letters, **98**(8): 084101.

Müller, T. M., Gurevich, B., and Lebedev, M. 2010. Seismic wave attenuation and dispersion resulting from wave-induced flow in porous rocks — a review. Geophysics, **75**(5): 75A147–75A164.

North, F. K. 1985. Petroleum geology. Allen & Unwin, Boston.

Plona, T. J. 1980. Observation of a second bulk compressional wave in a porous medium at ultrasonic frequencies. Applied Physics Letters, **36**(4): 259–261.

Pride, S. R., Gangi, A. F., and Morgan, F. D. 1992. Deriving the equations of motion for porous isotropic media. The Journal of the Acoustical Society of America, **92**(6): 3278–3290.

Rasolofosaon, P. N. 1988. Importance of interface hydraulic condition on the generation of second bulk compressional wave in porous media. Applied Physics Letters, **52**(10): 780–782.

Sahay, P. N. 2008. On the Biot slow S-wave. Geophysics, **73**(4): N19–N33.

Sahay, P. N. 2013. Biot constitutive relation and porosity perturbation equation. Geophysics, **78**(5): L57–L67.

Sahay, P. N., Spanos, T. J. T., and de la Cruz, V. 2001. Seismic wave propagation in inhomogeneous and anisotropic porous media. Geophysical Journal International, **145**(1): 209–222.

Sánchez Pérez, L. A. 2010. Reflection and transmission in poroelasticity. Master of Science Thesis, Centro de Investigación Científica y de Educación Superior de Ensenada, Baja California. xii, 104 pp.

Slattery, J. C. 1969. Single-phase flow through porous media. AIChE Journal, **15**(6): 866–872.

Solorza, S. and Sahay, P. N. 2009. On extensional waves in a poroelastic cylinder within the framework of viscosity-extended biot theory: The case of traction-free open-pore cylindrical surface. Geophysical Journal International, **179**(3): 1679–1702.

Whitaker, S. 1969. Advances in theory of fluid motion in porous media. Industrial & engineering chemistry, **61**(12): 14–28.

Appendix A.   Poroelastic properties

The poroelastic properties used to compute reflection-transmission coefficients and the response of a stack of porous layers correspond with those of a sintered glass beads porous medium and a Berea sandstone. The physical properties of the former are reported by Bouzidi and Schmitt (2012). They are in Table 1.

Table 1. Physical properties of the sintered glass beads porous medium (Bouzidi and Schmitt, 2012). The Biot critical frequency Ω_i is calculated considering water as the saturating fluid.

Property	Value	Unit
Mineral Bulk modulus (K_s)	32.9	GPa
Mineral Shear modulus (μ_s)	23.1	GPa
Frame Bulk modulus (K_0)	4.1	GPa
Frame Shear modulus (μ_0)	6.9	GPa
Solid density (ρ_s)	2440	Kg/m^3
Unperturbed porosity (η_0)	0.39	-
Permeability (κ)	1.99×10^{-11}	m^2
Tortuosity (S)	1.44	-
Biot critical frequency for water saturation (Ω_i)	15 898	rad/s

The Berea sandstone is a well-characterized rock used in numerical and experimental studies. Its physical properties are presented in Table 2, and they are as reported by Kuteynikova et al. (2014).

Table 2. Physical properties of the Berea sandstone (Kuteynikova et al., 2014). The Biot critical frequency Ω_i is calculated considering water as the saturating fluid.

Property	Value	Unit
Mineral Bulk modulus (K_s)	43.5	GPa
Mineral Shear modulus (μ_s)	31.7	GPa
Frame Bulk modulus (K_0)	7	GPa
Frame Shear modulus (μ_0)	4.2	GPa
Solid density (ρ_s)	2650	Kg/m^3
Unperturbed porosity (η_0)	0.2	-
Permeability (κ)	6×10^{-13}	m^2
Tortuosity (S)	3	-
Biot critical frequency for water saturation (Ω_i)	114 400	rad/s

The properties for the saturating fluid are in Table 3.

Table 3. Physical properties of the saturating fluid.

Property	Value for water	Unit
Fluid Bulk modulus (K_f)	2.25	GPa
Fluid Shear viscosity (μ_f)	10^{-3}	Pa·s
Fluid Bulk viscosity (ξ_f)	3×10^{-3}	Pa·s
Fluid density (ρ_s)	1000	Kg/m^3

Appendix B. Pseudocodes

This chapter presents the pseudocodes of functions used to compute the results discussed in the thesis. Section B.1 describes the function used to compute the dispersion relation of the poroelastic waves. Section B.2 shows the pseudocode for the reflection and transmission coefficients. After that, the pseudocode for the poroelastic reflectivity method is in section B.3.

B.1 Dispersion relations

The dispersion relations for the poroelastic media are computed with the function DispRel (algorithm 1). It calculates the compressional and shear velocity matrix. Then, the velocities are computed with the eigenvalues formulas. As a side result, this function returns the eigenvector matrix for compressional and shear velocity matrices. The pseudocode 1 is valid for velocities in the dCS and Biot theories.

Algorithm 1: Pseudocode of DispRel function for computing the dispersion relation and associated eigenvector matrix of a porous medium.

---

1 **Function** <u>DispRel(*Properties, frequency*)</u>**:**
  Input: Medium properties and frequency.
  Output: Poroelastic velocities and associated eigenvectors.
  /* *Computation of K, mu, nu, xi, rho, and omega matrices.* */
2   **SET** K = CalculateK(*Properties*) ;
3   **SET** mu = CalculateMu(*Properties*) ;
4   **SET** nu = CalculateNu(*Properties*) ;
5   **SET** xi = CalculateXi(*Properties*) ;
6   **SET** rho = CalculateRho(*Properties*) ;
7   **SET** Omega = CalculateOmega(*Properties, frequency*) ;
  /* *Computation of the alpha and beta velocity matrices.* */
8   **SET** alpha = [rho * Omega]$^{-1}$ [K - $i * frequency$ * xi] ;
9   **SET** beta_Matrix = [rho * Omega]$^{-1}$ [mu - $i * frequency$ * nu] ;
  /* *Computation of velocities and associated eigenvectors.* */
10 **SET** vP=Eigenvalues(alpha) ;
11 **SET** vS=Eigenvalues(beta) ;
12 **SET** RP=Eigenvectors(alpha) ;
13 **SET** RS=Eigenvectors(beta) ;
14 **SET** V=[vP, vS] ;
15 **return** V, RP, RS

The function DispRel is coded in MATLAB, composed of 117 lines of code.

B.2 Reflection and transmission coefficients

For the case of the reflection and transmission coefficients, the pseudocode that describes their solution is in algorithm 2. It is valid for permeable and impermeable contacts, and it works for both dCS and Biot theories. This function receives the poroelastic properties of each porous half-space, and it returns a 8 × 8 matrix that contains the reflection and transmission coefficients for all incident waves.

Although the analytical solution for incident fast SH waves is developed, the pseudocode 2 is used to compute the solution for all kinds of incident SH-waves. In this case, the function returns a 4 × 4 matrix.

Algorithm 2: Computation of the reflection and transmission coefficients, at the contact of two porous half-spaces, with respect to the angle and frequency of the incident wave.

---

1 Function RTCoeff(*Media*1, *Media*2, *angle*, *frequency*)**:**
　　/* *Media1 and Media2 contain the properties of each porous media.* */
　　Input: Properties of porous media, incident angle, and frequency.
　　Output: Reflection and transmission coefficients.
　　/* *Computation of velocities (V) and the associated eigenvectors (RP and RS).* */
2 　**CALL** DispRel(*Media*1, *frequency*) **RETURNING** V_1, RP_1, RS_1 ;
3 　**CALL** DispRel(*Media*2, *frequency*) **RETURNING** V_2, RP_2, RS_2 ;
　　/* *Computation of displacements and stresses* */
4 　**SET** displacements= CalculateDisplacements(Media1, V_1, RP_1, RS_1, Media2, V_2, RP_2, RS_2, *angle*) ;
5 　**SET** stresses= CalculateStresses(Media1, V_1, RP_1, RS_1, Media1, V_2, RP_2, RS_2, *angle*) ;
　　/* *Set up the coefficient matrices for the scattered (A) and incident (B) waves.* */
6 　**SET** A=CalculateA(displacements, stresses) ;
7 　**SET** B=CalculateB(displacements, stresses) ;
　　/* *Solution of reflection and transmission coefficients.* */
8 　**SET** rt = Gauss_Jordan_Solution(A,B) ;
9 　**return** rt

The function RTCoeff is coded in MATLAB. It is composed of 119 lines of code for the SH-wave case and 178 lines for the P- and SV-waves case. Both cases are available to

compute the solution for permeable and impermeable contacts.

B.3   Poroelastic reflectivity method

The pseudocode for the poroelastic reflectivity method is presented in algorithm 3. This function is used to compute the case of poroelastic layers with permeable and impermeable contacts in both Biot and dCS theories.

The algorithm 3 is defined for P and SV-waves. Even so, it is valid for the SH-waves, for which the reflection and transmission coefficients (rt) are a 4×4 matrix. Thus, the sub-matrices rD = rt(1:2, 1:2), tD = rt(1:2, 2:3), rU = rt(3:4, 2:4), and tU = rt(1:2, 3:4) are 2×2 matrices for the SH-waves.

The function Reflectivity is coded in MATLAB and C language. MATLAB code comprises 175 lines for the SH-waves and 236 lines for P- and SV-waves. The function in C language contains 155 lines of code for the SH-waves and 223 lines for P- and SV-waves. Moreover, the DispRel and RT functions are implemented in C language as a part of the Reflectivity code.

Algorithm 3: Computation of the reflectivity method for a stack of N plane porous layers.

---

1 **Function** <u>Reflectivity(*Stack, angle, frequency*)</u>**:**

    /* *Stack is an array that contains the N properties,*
       velocities, eigenvectors, and thickness of each layer.   */

    Input: Properties of the stack, incident angle, and frequency.

    Output: Total reflection and transmission amplitudes.

2   **SET** nl= number of layers in the stack ;

3   **SET** h=layer thickness ;

    /* *R/T coefficients in the lowest contact.*   */

4   **CALL** RTCoeff(*Stack*(nl-1), *Stack*(nl), *angle, frequency*) **RETURNING** rt ;

    /* *Sub-matrices of the 8X8 rt matrix.*   */

5   **SET** rD = rt(1:4, 1:4) ;

6   **SET** tD = rt(4:8, 1:4) ;

7   **SET** rU = rt(4:8, 4:8) ;

8   **SET** tD = rt(1:4, 4:8) ;

    /* *Computation of the total reflection (RD) and transmission*
       (TD) amplitudes.   */

9   **for** *layer* ← nl−1 **TO** 1 **STEP** −1, *l* **do**

10   **SET** ED = CalculatePhase(*Stack.V*(*l*), h) ;

11   **SET** R'D = ED*rD*ED ;

12   **SET** T'D = tD*ED ;

13   **CALL** RTCoeff(*Stack*(l-1), *Stack*(l), *angle, frequency*) **RETURNING** rt;

14   **SET** rD = rt(1:4, 1:4) ;

15   **SET** tD = rt(4:8 , 1:4) ;

16   **SET** rU = rt(1:4 , 4:8) ;

17   **SET** tD = rt(4:8 , 4:8) ;

18   **SET** RD = rD + tU*R'D*[I - rU*R'D]*tD ;

19   **SET** TD = T'D*[I - rD*R'D]* tD ;

20   **end for** ;

21   **return** RD,TD ;